

DUAL BAND MICROSTRIP IMPLANTABLE ANTENNA DESIGN FOR
BIOMEDICAL APPLICATIONS

A THESIS SUBMITTED TO
THE GRADUATE SCHOOL OF NATURAL AND APPLIED SCIENCES
OF
MIDDLE EAST TECHNICAL UNIVERSITY

BY

DAMLA ALPTEKIN

IN PARTIAL FULFILLMENT OF THE REQUIREMENTS
FOR
THE DEGREE OF MASTER OF SCIENCE
IN
ELECTRICAL AND ELECTRONICS ENG.

AUGUST 2015

Approval of the thesis:

**DUAL BAND MICROSTRIP IMPLANTABLE ANTENNA DESIGN
FOR BIOMEDICAL APPLICATIONS**

submitted by **DAMLA ALPTEKIN** in partial fulfillment of the requirements
for the degree of **Master of Science in Electrical and Electronics Eng. Department, Middle East Technical University** by,

Prof. Dr. Gülbin Dural Ünver _____
Dean, Graduate School of **Natural and Applied Sciences**

Prof. Dr. Gönül Turhan Sayan _____
Head of Department, **Electrical and Electronics Eng.**

Prof. Dr. Nevzat Güneri Gençer _____
Supervisor, **Elec. and Electronics Eng. Dept., METU**

Assoc. Prof. Dr. Lale Alatan _____
Co-supervisor, **Elec. and Electronics Eng Dept., METU**

Examining Committee Members:

Prof. Dr. Sencer Koç _____
Electrical and Electronics Engineering Dept., METU

Prof. Dr. Nevzat Güneri Gençer _____
Electrical and Electronics Engineering Dept., METU

Prof. Dr. Gülbin Dural Ünver _____
Electrical and Electronics Engineering Dept., METU

Prof. Dr. Gönül Turhan Sayan _____
Electrical and Electronics Engineering Dept., METU

Prof. Dr. Ergin Atalar _____
Elec. and Electronics Engineering Dept., Bilkent University

Date: 28.08.2015

I hereby declare that all information in this document has been obtained and presented in accordance with academic rules and ethical conduct. I also declare that, as required by these rules and conduct, I have fully cited and referenced all material and results that are not original to this work.

Name, Last Name: DAMLA ALPTEKIN

Signature :

ABSTRACT

DUAL BAND MICROSTRIP IMPLANTABLE ANTENNA DESIGN FOR BIOMEDICAL APPLICATIONS

Alptekin, Damla

M.S., Department of Electrical and Electronics Eng.

Supervisor : Prof. Dr. Nevzat Güneri Gençer

Co-Supervisor : Assoc. Prof. Dr. Lale Alatan

August 2015, 116 pages

In this study, numerical and experimental analysis of a dual band (Medical Implant Communications Service-MICS; 402 – 405 MHz, Industrial, Scientific and Medical-ISM; 2.4 – 2.48 GHz) implantable antenna design for biomedical applications are presented. The proposed antenna is in the type of Planar Inverted-F Antenna (PIFA) covered with a superstrate. For miniaturization, the metallic patch of the antenna is meandered and shorting-pin is used between the patch and ground plane. In addition, stacking patch structure is used to lengthen the current flow path. Numerical analysis of the implant antenna is carried out using commercially available Finite Element Method (FEM)-based High Frequency Structure Simulator (HFSS) software. As a tissue model a generic dispersive skin model is used. Two antenna designs are presented: an initial antenna operating in MICS band and a miniaturized optimized antenna operating in dual band (MICS and ISM). For both antennas, a parametric antenna model is presented and each antenna design step is explained. For experimental studies, skin mimicking phantoms are developed in MICS and ISM bands. The

proposed antenna is fabricated and *in vitro* tested. It is shown that the antenna resonates at 403.5 MHz with a reflection coefficient of -23 dB, and a 10-dB bandwidth of 56 MHz, which covers the MICS band, moreover, it resonates at 2.45 GHz with a reflection coefficient of -22 dB, and a 10-dB bandwidth of 200 MHz, which covers the ISM band. The maximum simulated gain is found as -33 dBi. Communication link measurements are performed using commercially available Microsemi-Zarlink Application Development Kit for Medical Telemetry (ZLE70102) in order to check the functioning of the proposed antenna. Designed antenna is inserted into MICS band phantom and it is achieved to wake-up base station module at ISM band and to send data at MICS band in 4 meter range. Moreover, patient safety issues, comparative analysis of radiation performance for different phantom models, effect of coaxial cable, far field properties of implantable antennas, and gain measurement of the electrically small antennas are discussed.

Keywords: Implantable Medical Devices, Implantable Antenna, Electrically Small Antenna, Planar Inverted-F Antenna, Dual Band Medical Telemetry

ÖZ

BİYOMEDİKAL UYGULAMALAR İÇİN VÜCUT İÇERİSİNE YERLEŞTİRİLEBİLİR ÇİFT BANTLI MİKROŞERİT ANTEN TASARIMI

Alptekin, Damla

Yüksek Lisans, Elektrik ve Elektronik Mühendisliği Bölümü

Tez Yöneticisi : Prof. Dr. Nevzat Güneri Gençer

Ortak Tez Yöneticisi : Assoc. Prof. Dr. Lale Alatan

Ağustos 2015, 116 sayfa

Bu çalışmada; biyomedikal uygulamalar için tasarlanan, çift bantta (Medikal Implant Haberleşme Servisi-MICS; 402-405 MHz, Endüstriyel, Bilimsel ve Medikal-ISM; 2.4-2.48 GHz) çalışma özelliğine sahip, vücut içerisine yerleştirilebilir antenin sayısal ve deneysel analizi sunulmuştur. Önerilen anten yüzeysel devrilmis F-anten (PIFA) tipinde olup, üzeri üstsubstrat ile kaplanmıştır. Anten boyutunun küçültülmesi amacıyla, metalik şerit bükülmüş ve metalik şerit ile toprak düzlemi arasında kısaltıcı pin kullanılmıştır. Ayrıca, akım akış yolunu uzatmak amacıyla katmanlı yama yapısı kullanılmıştır. Implant antenin sayısal analizleri piyasada mevcut olan ve Sonlu Eleman Yöntemine (FEM) dayalı çözüm yapan Yüksek Frekanslı Yapı Simulatoru (HFSS) programı ile yürütülmüştür. Doku modeli olarak frekansa bağlı elektriksel özellikleri değişen genel deri modeli kullanılmıştır. İki adet anten tasarımı sunulmuştur: MICS bantta çalışan ön anten tasarımı ve çift bantta (MICS ve ISM) çalışan küçültülmüş anten tasarımı. İki anten için de, parametrize edilmiş anten modeli sunulmuş ve her bir tasarım

adımı açıklanmıştır. Deneysel çalışmalar için, MICS ve ISM bantta, dokunun elektriksel özelliklerini taklit eden fantomlar geliştirilmiştir. Önerilen anten üretilmiş ve bu fantomlar içerisinde test edilmiştir. Giriş geri dönüş kaybının 403.5 MHz'de -23 dB olduğu ve 10-dB'deki 56 MHz'lik bant genişliği ile MICS bantını kapsadığı gösterilmiştir. Ayrıca, antenin 2.45 GHz de -22 dB'lik giriş geri dönüş kaybına sahip olduğu ve 10-dB'deki 200 MHz'lik bant genişliği ile ISM bantını kapsadığı gösterilmiştir. Antenin en yüksek kazanç değeri benzetimlerde -33 dBi olarak bulunmuştur. Antenin işleyişini kontrol etmek amacıyla ticari olarak bulunan Microsemi- Medikal Telemetry için Zarlink Uygulama Geliştirme kiti (ZLE70102) kullanılarak, haberleşme hattı ölçümleri gerçekleştirilmiştir. Tasarlanan anten MICS bantta çalışan fantom içerisine yerleştirilmiş, 4 metrelik bir mesafede baz istasyonu ünitesi ISM bantta uyandırılmış ve MICS bantta veri gönderimi sağlanmıştır. Ayrıca; hasta güvenliği, farklı fantom modellerine göre radyasyon performanslarının karşılaştırılması, eş eksenli kablunun etkisi, implant antenin uzak alan özellikleri ve elektriksel olarak küçük antenlerin kazanç ölçümleri tartışılmıştır.

Anahtar Kelimeler: Implant edilebilir Medikal Cihazlar, Implant Anten, Elektriksel Küçük Anten, Yüzeysel Devrilmiş F-Anten, Çift Bant Medikal Haberleşme

To my beloved mother...

ACKNOWLEDGMENTS

First of all, I would like to thank my supervisor Prof. Dr. Nevzat G. Gençer. I want to express my gratitude to him due to the entire support and assistance he gave me throughout my thesis study. In addition, I would like to thank my co-supervisor Assoc. Prof. Dr. Lale Alatan. I want to present my appreciation to her for spending her valuable time to my thesis study. I cannot achieve the desired results without her guidance and encouragement. Therefore, I present my endless appreciation to her.

Especially, I would like to thank Prof. Dr. Gülbin Dural Ünver for initiating me antenna design when I was an undergraduate student. Due to her positive motivation and encouragement, I found the courage to start the graduate study. I would also like to acknowledge the members of my thesis jury for having accepted to examine this work and for their valuable comments and insights.

I would moreover thank Fikret Küçükdeveci and my friends from Kardiosis for their precious support during my graduate study.

I would like to express my gratitude to the members of Brain Research Laboratory; Dr. Reyhan Zengin, Balkar Erdoğan, Ekrem Bayraktar, and Ümit İrgin for motivating me in my hard times. I would also like to thank to my friends from the Antenna Laboratory; Savaş Karadağ, Yusuf Sevinç and Feza Mutlu for creating a lovely laboratory environment. I am grateful to Adem Ateş and Erdinç Yurdakul for their help in fabrication processes and measurement setups. Without the talent of Erdinç, it would not be possible to overcome any technological problem while prototyping.

I would like to thank my friends for all the great time we spent together: Mursel Karadaş, for his support and friendship. I could never be able to become a research assistant without his help. It is a privilege to work with such a clever

and encouraging colleague. Dilek Baysal, for being such a charming person and giving me inspiration. Begüm Kayalar, for being a perfect dorm-mate and *Bebiş*. Öykü Çobanoğlu, for her support and ability to always find a way to help people. My most sincere appreciation is addressed to a group of friends: *Semiconductor*. You all have been extraordinary examples and sources of motivation for me in my hard times. I will always remember the times we spent together as the best years of my life.

Special thanks to my best friend Tuğba Can for her positive attitude and being the definition of a good person. Despite the distance, I always feel happy and hopeful when I think about our invaluable friendship.

I would like to express my deepest thank to Yusuf Soydan for his support, care, encouragement and unbelievable patience. Throughout my thesis study, he is literally always there for me under all types of difficulties in both academic and personal life. Despite all my disappointments, he always found a way to cheer me up. I know that I could not achieve to finish this study without him. I feel incredibly lucky to have him in my life.

Finally, I would like to thank my family; my father Kamil Alptekin and my sister Duygu Alptekin Avcı. You have always been present to love and support me under any circumstances. It would be impossible to imagine myself in my current position without your everlasting love and encouragement.

TABLE OF CONTENTS

ABSTRACT	v
ÖZ	vii
ACKNOWLEDGMENTS	x
TABLE OF CONTENTS	xii
LIST OF TABLES	xv
LIST OF FIGURES	xvii
LIST OF ABBREVIATIONS	xxvii
CHAPTERS	
1 INTRODUCTION	1
1.1 Overview	1
1.2 Implantable Antenna Design Challenges	2
1.2.1 Miniaturization	2
1.2.2 Dual Band Operation	3
1.2.3 Good Radiation Efficiency	4
1.2.4 Patient Safety	5
1.3 Literature Survey on Implantable Antennas for Biomedical Telemetry	6
1.4 Scope of the Thesis	10

1.5	Thesis Organization	13
2	DESIGN OF PATCH BASED IMPLANTABLE ANTENNA IN MICS BAND	15
2.1	Introduction	15
2.1.1	Method of Analysis	16
2.2	Design of a Patch Antenna in the MICS Band (402-405 MHz) Radiating into Air	18
2.3	Design of a Patch Antenna in the MICS Band (402-405 MHz) Radiating into Tissue	24
2.3.1	Electrically Small Antenna Design	28
2.3.2	Antenna Miniaturization Techniques	28
2.3.3	First Prototype: MICS Band Implantable Antenna Design	39
2.3.3.1	Antenna Design	39
2.3.3.2	Fabrication and Measurement in Air	48
2.3.3.3	Phantom Preparation in the MICS band and <i>in vitro</i> Measurement	49
3	DESIGN OF MINIATURIZED IMPLANTABLE PIFA IN DUAL BAND	53
3.1	Introduction	53
3.2	Antenna Design Steps	54
3.3	Realization and Measurement of the Final Design	76
3.3.1	Realization of the Antenna	76
3.3.2	Return Loss Measurement	76
3.3.3	Communication Link Measurement	82
4	RESULTS AND DISCUSSION	85

4.1	Introduction	85
4.1.1	Patient Safety	85
4.1.2	Effect of Different Phantoms	89
4.1.3	Effect of Coaxial Cable	89
4.1.4	Far Field Properties of the Antenna	91
	4.1.4.1 Effects of Conducting Medium on the Antenna Pattern	91
	4.1.4.2 Measurement of the Maximum Gain of Electrically Small Antennas	94
5	CONCLUSION	101
APPENDICES		
A	MEASUREMENT OF ELECTRICAL PROPERTIES	105
A.1	Theory	105
A.2	Experimental Studies and Results	107
	REFERENCES	111

LIST OF TABLES

TABLES

Table 1.1 Dielectric properties of different body tissues in MICS and ISM bands	3
Table 1.2 Maximum Equivalent Isotropic Radiated Power (EIRP) level	4
Table 1.3 Examples of Uplink (From implant to base station)	5
Table 1.4 Comparison of the implantable patch antennas reported in the literature with respect to operating bands, implantation cite, antenna types, occupied volume, 10 dB impedance BW and simulated maximum gain values.	12
Table 2.1 Design parameters of the initial patch antenna which operates in the MICS Band	20
Table 2.2 Design parameters of the initial patch antenna which operates in the MICS Band	20
Table 2.3 Design Parameters of Optimized Patch Antenna which Operates in the MICS Band	21
Table 2.4 Optimized Dimensions of the Prototype-1	46
Table 2.5 Recipe for skin mimicking gel taken from [1]	50
Table 3.1 Optimized Dimensions of the Design-3 given in Figure 3.14	63

Table 3.2 Selected dimensions according to conducted parametric study results (See Figure 3.22 and Figure 3.23)	68
Table 3.3 Antenna design parameters of the final design	74
Table 3.4 Recipe for skin mimicking gel in the ISM band	78

LIST OF FIGURES

FIGURES

Figure 1.1 (a) Inductive link system (b) External coil example [2]	2
Figure 1.2 Dual band communication between implant medical device and external control unit (Base Station)	4
Figure 1.3 (a) Biocompatible material Silastic MDX-4210 (b) Encased antenna [3]	5
Figure 1.4 Examples of implantable antennas: (a) Spiral PIFA [4] (b) Meandered PIFA and skin mimicking phantom [1] (c) Cavity slot antenna [5] (d) Meandered stacked patch antenna [6] (e) CP Antenna [7] (f) Nonsuperstrate antenna [8] (f) Pyramidally stacked patch antenna [9]	11
Figure 2.1 Side view of the basic patch model where h is the thickness of the substrate	16
Figure 2.2 Return loss of the patch antenna designed according to the Table 2.3	21
Figure 2.3 Top view of the simulated patch antenna: Antenna parameters are optimized to operate in the MICS band	22
Figure 2.4 Return loss of the patch antenna operates in the MICS Band	22
Figure 2.5 Simulated 3D directivity pattern of the patch at 403 MHz .	23

Figure 2.6 Gain as a function of resonant frequency, substrate permittivity and substrate thickness for the TM_{10} mode of a rectangular patch [10]	23
Figure 2.7 Patch antenna and tissue model proposed in [2]. Note that the dimensions are not scaled.	24
Figure 2.8 HFSS Model of the patch antenna inserted in 2/3 muscle block (a) Side view (b) Top view	25
Figure 2.9 Return loss of the patch antenna which is inserted into 2/3 muscle block	26
Figure 2.10 Simulated three-dimensional far field pattern of patch antenna at 403 MHz which is inserted into 2/3 muscle block	27
Figure 2.11 Chu sphere of radius "a" centered about the origin. The <i>Chu sphere</i> is the minimum circumscribing sphere enclosing the antenna of maximum dimension 2a [11]	29
Figure 2.12 Side view of a planar inverted-F antenna (PIFA)	30
Figure 2.13 Development of PIFA from microstrip antenna (a) Microstrip antenna (b) Microstrip antenna with a shorting wall (c) PIFA with a narrow strip [12].	31
Figure 2.14 Derivation of the quarter wave patch from patch antenna with the electric field distribution	31
Figure 2.15 Effect of reducing the number of shorting pins in a quarter-wavelength patch to form a planar inverted-F antenna (a) PIFA_A: Shorting pins are at the corner of the radiating surface (b) PIFA_B: Shorting pins are at the middle of the radiating surface (c) Change in resonant frequency [13].	32
Figure 2.16 Meander line antennas with equivalent inductance models where s is the spacing and l is the length of the meander section. L_1 and L_2 represents the equivalent inductance of the each section [14]	34

Figure 2.17 Resonant frequency of meander line antennas with different geometries [15]	34
Figure 2.18 Surface current distributions for meandered rectangular microstrip patches with (a) meandering slits and (b) a pair of triangular notches cut at the patch's nonradiating edges [16]	35
Figure 2.19 Schematic of the compact microstrip patch antenna [17]	36
Figure 2.20 Variation of resonant frequency f_r of the antenna with slot length (l)	37
Figure 2.21 Surface current distribution for various slot lengths. (a) $l = 0$ mm, (b) $l = 7.5$ mm, (c) $l = 12.5$ mm [17].	37
Figure 2.22 The geometry of the 4-layered stacked patch antenna [18].	38
Figure 2.23 Current distribution on the antenna layers at 402 MHz [18].	38
Figure 2.24 Simulated electric field of patch antenna at 403 MHz which radiates into air	40
Figure 2.25 HFSS model of the quarter wave antenna (a) Quarter wave patch antenna model in air with shorting pins and simulated electric field at 402 MHz (b) Return loss of the quarter wave rectangular microstrip antenna	40
Figure 2.26 HFSS model of the $16\text{cm} \times 7\text{cm}$ quarter wave antenna (a) Top view of the quarter wave patch antenna model in air with shorting pins (b) Simulated far field gain pattern (c) Return loss	41
Figure 2.27 Simulated results for $16\text{ cm} \times 7\text{ cm}$ quarter wave antenna in 2/3 muscle block tissue (a) Return loss (b) Input impedance	42
Figure 2.28 Skin model with embedded antenna in HFSS	44
Figure 2.29 $3.1\text{ cm} \times 1.1\text{ cm}$ patch model in skin	44

Figure 2.30 Comparison of simulated S_{11} of the antenna for different feed positions- l_f	44
Figure 2.31 3.1 $cm \times 1.1 cm$ fully meandered patch model in skin	45
Figure 2.32 Comparison of simulated S_{11} of the fully meandered patch antenna for different feed positions- l_f	45
Figure 2.33 3.1 $cm \times 1.1 cm$ PIFA model in skin	45
Figure 2.34 Comparison of simulated S_{11} of the PIFA for different feed positions- l_f	46
Figure 2.35 HFSS model of the first prototype antenna (a) Top view of the antenna with conductor parameters (b) Side view of the antenna	47
Figure 2.36 Simulated return loss of the Prototype-1	47
Figure 2.37 Simulated far field gain for the Prototype-1 at 402 MHz	48
Figure 2.38 Photograph of fabricated implantable antenna	48
Figure 2.39 Comparison of the measured and simulated S_{11} in air	49
Figure 2.40 Process of preparing skin mimicking gel for MICS band	50
Figure 2.41 (a) Skin mimicking fluid (b) Antenna measurement in skin mimicking fluid	51
Figure 2.42 Comparison of permittivity of the MICS band skin-mimicking gels with the reference data from [19].	51
Figure 2.43 Comparison of conductivity of the MICS band skin-mimicking gels with the reference data from [19].	52
Figure 2.44 Comparison of the measured and simulated S_{11} in skin mimicking gel	52
Figure 3.1 Design 1 (a) Top view of the antenna in xy-plane (b) Side view of the antenna in yz-plane	55

Figure 3.2 Simulated S_{11} of the antenna - Design 1	55
Figure 3.3 Simulated three dimensional gain pattern of the antenna - Design 1	56
Figure 3.4 Design 2 (a) Top view of the antenna in xy-plane (b) Side view of the antenna in yz-plane (c)Trimetric view of the antenna	57
Figure 3.5 Simulated S_{11} of the antenna - Design 2	58
Figure 3.6 Simulated three dimensional gain pattern of the antenna - Design-2	58
Figure 3.7 Top view of the antenna with design parameters - Design 3	59
Figure 3.8 Effect of feed point location on the resonant frequency	59
Figure 3.9 Input impedance of the antenna for $l_f = 2.82 \text{ cm}$	60
Figure 3.10 Current density vector distribution on the patch surface (a) 403.5 MHz (b) 2.45 GHz	61
Figure 3.11 Simulated S_{11} of the antenna for $w_2 = w_5 = 0.1 \text{ cm}$	61
Figure 3.12 Input impedance of the antenna for $w_2 = w_5 = 0.1 \text{ cm}$	62
Figure 3.13 Current vector distribution on the patch surface for $w_2 = w_5 =$ 1 cm (a) 403.5 MHz (b) 2.45 GHz	62
Figure 3.14 Top view of the antenna dual band (MICS and ISM band) tuned antenna - Design 3	63
Figure 3.15 Simulated S_{11} of the dual band tuned antenna	63
Figure 3.16 Top view of the antenna in Step-1 which fits in an area of $2 \text{ cm} \times 1 \text{ cm}$	65
Figure 3.17 Simulated S_{11} of the antenna in Step-1	65
Figure 3.18 Simulated Z_{in} of the antenna in Step-1	66

Figure 3.19 Current density vector distribution on the patch surface of the antenna in Step-1 (a) 403.5 MHz (b) 2.45 GHz	66
Figure 3.20 Top view of the antenna in Step-2	67
Figure 3.21 Simulated S_{11} of the antenna in Step-2	68
Figure 3.22 Effect of lower patch arm parameters w_1, w_2 and w_3 on the resonant frequency	69
Figure 3.23 Effect of upper patch arm parameters w_4, w_5 and w_6 on the resonant frequency	70
Figure 3.24 Top view of the antenna designed according to parameters given in Table 3.2	71
Figure 3.25 Simulated S_{11} of the antenna designed according to parameters given in Table 3.2	71
Figure 3.26 Optimization setup in HFSS (a) Goal definition for both MICS and ISM bands (b) Optimization parameters	72
Figure 3.27 Geometry of the proposed antenna with all design parameters (a) Top view of the antenna (b) Side view of the antenna	73
Figure 3.28 Simulated S_{11} of the antenna proposed antenna designed according to parameters given in Table 3.3	74
Figure 3.29 Simulated current density distribution on the patch surface of the proposed antenna (a) 403.5 MHz (b) 2.45 GHz	75
Figure 3.30 Simulated 3D gain pattern of the proposed antenna (a) 403.5 MHz (b) 2.45 GHz	75
Figure 3.31 Fabricated antenna (a) Fabricated antenna parts (b) Assembled antenna with feeding cable	77
Figure 3.32 Effect of double-sided tape permittivity on the resonant frequency	77

Figure 3.33 Comparison of simulated and measured S_{11} of the proposed antenna in air	79
Figure 3.34 Comparison of simulated and measured S_{11} of the proposed antenna in MICS band phantom	79
Figure 3.35 Process of preparing skin mimicking gel for ISM band	80
Figure 3.36 Comparison of permittivity of the ISM band skin-mimicking gels with the reference data from [19].	80
Figure 3.37 Comparison of conductivity of the ISM band skin-mimicking gels with the reference data from [19].	80
Figure 3.38 (a) Skin mimicking phantom (b) Measurement of the phantom's electrical properties (c) Return loss measurement	81
Figure 3.39 Comparison of simulated and measured S_{11} of the proposed antenna in ISM band phantom	81
Figure 3.40 Medical telemetry application development kit: ZLE70102 (a) Base Station Application Unit (BAU) (b) Implant Application Unit (IAU)	83
Figure 3.41 GUI for the BAU: Green colored "In Session" indicates that communication is established between BAU and IAU	83
Figure 3.42 Telemetry setup: (a)Antenna test-bed in anechoic chamber (b) IAU with implant antenna inserted in phantom (c) Base Station Application Unit (BAU)	84
Figure 3.43 GUI for the IAU: "Hello Implant!" message is received.	84
Figure 4.1 Two approaches for biocompatible antenna design (a) Antenna fabricated on biocompatible material (b) Antenna encased with biocompatible material [7]	86

Figure 4.2 Comparison of simulated S_{11} of the antenna fabricated on RO3210 and Al_2O_3 ceramic substrate	86
Figure 4.3 Comparison of simulated S_{11} of the antenna for different thickness of encased biocompatible material	87
Figure 4.4 Side view of the simulation model used for the calculation of the SAR	87
Figure 4.5 Simulated average SAR of the antenna with 1 W input power (a) 403.5 MHz (b) 2.45 GHz	88
Figure 4.6 Simulation models to investigate the effect of different tissues on the resonant frequency: (a) One-layer skin phantom: case 1 (b) Three-layer tissue phantom where antenna is inserted into skin-fat interface: case 2 (c) Three-layer tissue phantom where antenna is inserted into fat-muscle interface: case 3 (d) Three-layer tissue phantom where antenna is inserted into muscle: case 4	90
Figure 4.7 Comparison of simulated S_{11} of the antenna for different phantom models given in Figure 4.6	91
Figure 4.8 Dielectric properties of skin fat and muscle in 20 MHz-3 GHz frequency band: (a) Relative Permittivity (ϵ_r) (b) Conductivity (S/m)	92
Figure 4.9 Simulation models to investigate the effect of coaxial feed on the resonant frequency: (a) Setup 1 (b) Setup 2 (c) Setup 3 [7]	93
Figure 4.10 Comparison of the simulated S_{11} of the antenna for different feeding models given in Figure 4.9	93

Figure 4.11 Results taken from [20] to show the effect of conducting medium on the radiation pattern of the antenna (a) A hypothetical wire antenna of full wave long carrying a uniform current. The position of the coordinate origins are indicated as: origin at center and origin at one end (b) Patterns in air and conducting medium when origin is at the center (c) Patterns in air and conducting medium when origin is at one end	95
Figure 4.12 Results taken from [21] to show the effect of phantom size on the radiation pattern of the antenna (a) A phantom model with the dimensions of length (l) x width (w) and height (h) (b) Simulated radiation pattern when lateral dimensions of the phantom is modified	96
Figure 4.13 Photographs of gain measurement setup for the MICS band (a) First measurement: S_{21} measurement of dummy antenna and monopole antenna (b) Second measurement: S_{21} measurement of dummy antenna and proposed implantable antenna	97
Figure 4.14 Schematic of the gain measurement technique for electrically small antennas proposed in [22]	99
Figure 4.15 Photographs of electrically small antenna gain measurement setup taken from [22] (a) Dielectric (Polypropylene) sphere that encloses the antenna is used to position the DUT in every possible position and polarization. Device under test is defined as combination of antenna, VCO and battery. DUT is centered within the sphere using the low-density foam (b) Details of the implemented random positioner (c) Reference gain antenna: Dipole mounted within dielectric sphere (d) Complete measurement setup in the anechoic chamber	100
Figure A.1 Open-ended probe model for virtual line method [23]	106
Figure A.2 Measurement setup of the calibration references (a) Air (b) De-ionized Water	108

Figure A.3 Comparison of measured S_{11} of the air when <i>gating</i> option is on and off	108
Figure A.4 Measured dielectric constant of olive oil: Real part (ϵ'_r) and the imaginary (ϵ''_r) of the permittivity are presented.	109

LIST OF ABBREVIATIONS

PIFA	Planar Inverted F-Antenna
HFSS	High Frequency Structure Simulator
MICS	Medical Implant Communications Service
ISM	Industrial, Scientific and Medical
IMD	Implantable Medical Devices
EIRP	Equivalent Isotropic Radiated Power
SAR	Specific Absorption Rate
DGF	Dyadic Green's Function
FDTD	Finite Difference Time Domain
λ_d	Wavelength in Dielectric
FEM	Finite Element Method
ESA	Electrically Small Antenna
DUT	Device Under Test

CHAPTER 1

INTRODUCTION

1.1 Overview

Medical devices that are implemented inside patient's body by means of a surgical operation are called implantable medical devices (IMDs) [24]. IMDs can be used for various applications such as diagnostic, monitoring and therapeutic applications. Pacemakers, defibrillators, neurostimulators, glucose monitors, and cochlear implants are typical examples of the implantable medical devices. One of the first IMD utilizing an implantable antenna is used for cancer treatment by Kasevich in 1988 [25]. In that study, the near field radiation of the antenna was used to harm tumour tissues by heating. Note that, the antenna was used only for treatment purposes not for communication with an exterior device. However, IMDs need to have wireless communication capability with an external device for the convenience of monitoring patients without physical contact and rigorous schedules [26]. Traditionally, inductive links as shown in Figure 1.1, between the implant and an external coil have been used at low frequencies [27, 28]. However, inductively coupled channels have some drawbacks such as low data rates (1-30 kbps), restricted range of communication (<10 cm) and dependence of internal coil-external coil position alignment [2, 24]. On the other hand, far field radio-frequency (RF) telemetry has advantages such as longer distance communication and high data rates [7]. Due to the advantages over the inductive links, medical devices with wireless telemetry has gained great interest in recent years. Recently, a globally accepted frequency band had been dedicated to biotelemetry for implantable devices. The European Telecommunications Standards Institute

(ETSI) reserved the medical implant communications service (MICS, 402 – 405 MHz) frequency band for medical and meteorological applications [29]. In addition, Industrial, Scientific, and Medical (ISM) bands; 433.1 – 434.8 MHz, 868 – 868.6 MHz, 902.8 – 928 MHz and 2400 – 2500 MHz, are suggested for implantable medical device biotelemetry [30]. Implantable antennas are the key components of telemetry systems since they provide communication between implanted device and external control equipment.

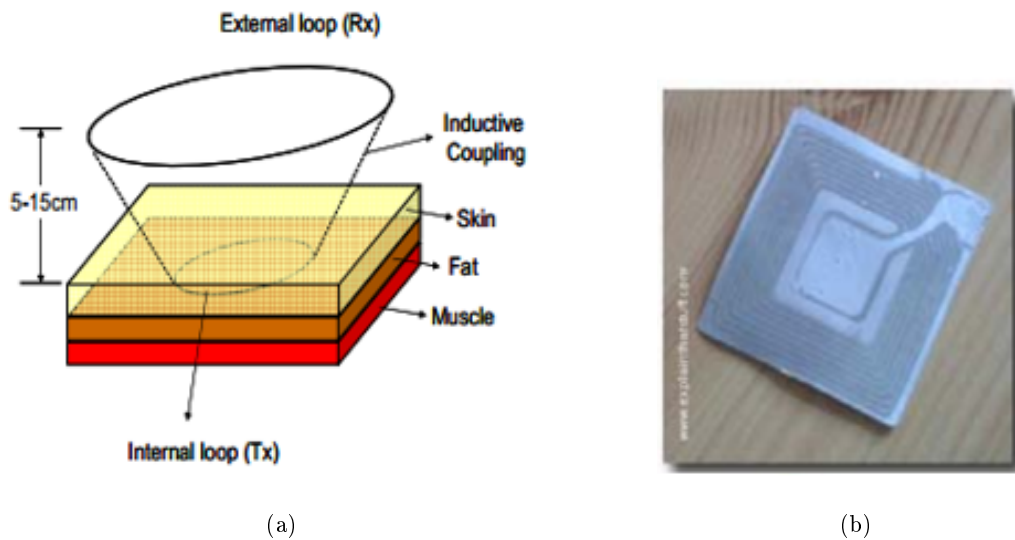


Figure 1.1: (a) Inductive link system (b) External coil example [2]

1.2 Implantable Antenna Design Challenges

Designing implantable antennas is a challenging task since there are many factors need to be considered. The requirement and constraints related to implantable antenna design are summarized in the following subsections::

1.2.1 Miniaturization

With the recent advances in the technology of microelectronics and medical technologies, implantable devices become smaller. For example, a typical car-

diac pacemaker size is $44.92 \text{ mm} \times 30.72 \text{ mm} \times 10 \text{ mm}$ [31]. An implantable antenna needs to be small enough to fit in a medical device. However, traditional half-wavelength ($\lambda/2$) or quarter wavelength ($\lambda/4$) antennas becomes useless for MICS band since free space wavelength in this band is approximately 74 cm. Therefore, miniaturization of the antenna is one of the greatest challenge in design. Fortunately, human tissue exhibits high permittivity which helps reduce size. Table 1.1 shows the dielectric properties (ϵ_r : *Dielectric constant*, σ : *Conductivity*, $\tan\delta$: *loss tangent*) of different body tissues at 403.5 MHz and 2.45 GHz.

Table1.1: Dielectric properties of different body tissues in MICS and ISM bands

Tissue	403.5 MHz			2.45 GHz		
	ϵ_r	σ	$\tan \delta$	ϵ_r	σ	$\tan \delta$
2/3 Muscle [5,32]	38.10	0.53	0.62	35.15	1.16	0.242
Muscle [19]	57.10	0.797	0.622	52.73	1.73	0.242
Fat [19]	5.58	0.042	0.328	5.28	0.105	0.145
Skin [19]	43.50	0.87	0.799	39.20	1.80	0.336

1.2.2 Dual Band Operation

For efficient use of the implanted device battery, device need to be used when an operation is necessary. Otherwise, the transceiver may consume a significant energy. To avoid unnecessary power consumption, a transceiver with dual band operation can be used. Commercially available Zarlink ZL70102 transceiver allows the implant to switch between sleep and wake-up modes as shown in Figure 1.2 [33]. The transceiver stays in “sleep mode” with low power consumption until a “wake-up” signal is sensed in the 2450 MHz ISM band. Then, data exchange happens in the MICS band.

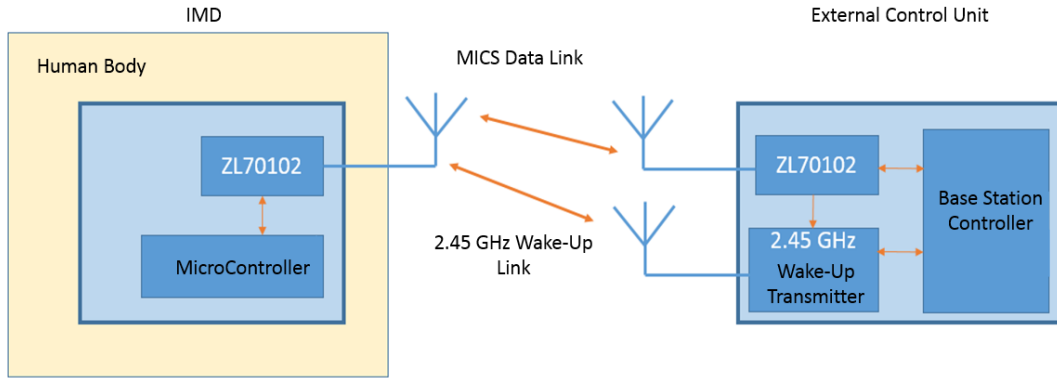


Figure 1.2: Dual band communication between implant medical device and external control unit (Base Station)

1.2.3 Good Radiation Efficiency

The radiated power from the implantable antenna should be strong enough to communicate with an external device. Since the antenna radiates into lossy human body, the near field strongly couples with the surrounding medium close to the antenna and thus the efficiency of the antenna decreases dramatically. Therefore, it is desired to maximize the power radiated out of the body [34]. However, there is a limitation on the Equivalent Isotropic Radiated Power (EIRP) of implantable medical devices operating in the MICS and ISM bands. The maximum power levels are reported in Table 1.2. Examples of the link budget which accounts all gains and losses from the transmitter; through the medium to the receiver are presented in Table 1.3 [5, 35]. Note that implantable antenna gain in the MICS band is quite low for the uplink communication (-31.5 dBi).

Table 1.2: Maximum Equivalent Isotropic Radiated Power (EIRP) level

Band	Maximum EIRP
MICS (402-405 MHz)	-16 dBm
ISM (2.4-2.5 GHz)	20 dBm

Table 1.3: Examples of Uplink (From implant to base station)

Parameter	MICS [35]	ISM [5]
Frequency	401 MHz	2.45 GHz
Bandwidth	200 kHz	200 kHz
Tx Power	-2 dBm	-36 dBm
Implant Antenna Gain	-31.5 dBi	-26.5 dBi
EIRP	-33.5 dBm	-62.5 dBm
Free space path loss (2 m)	30.5 dB	46.2 dB
Excess Loss & Fade Margin	25 dB	2 dB
Base Station antenna gain	2 dBi	2.1 dBi
Rx power	-87 dBm	-108.6 dBm
Rx noise	-101 dBm	-120 dBm

1.2.4 Patient Safety

Implantable antennas need to be biocompatible with the surrounding tissue in order to preserve patient safety. There are two common approaches for the biocompatibility of the antenna. One is to use biocompatible materials for the design of antennas. Most commonly used materials can be listed as teflon, macor, and ceramic alumina [31]. The other approach is to encapsulate antenna with a low-loss biocompatible coating. Figure 1.3 represents an implantable antenna covered by biocompatible material Silastic MDX-4210 ($\epsilon_r = 3.3$, $\sigma = 0.01$ S/m) [3].

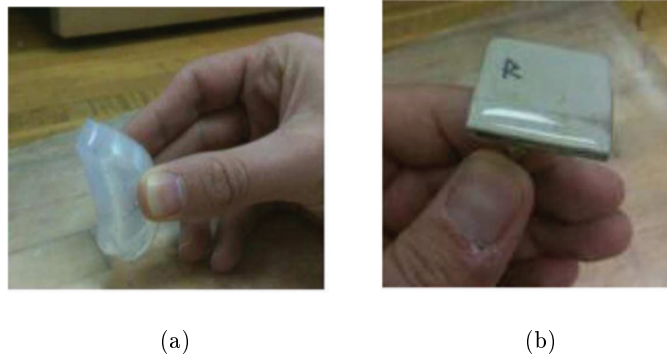


Figure 1.3: (a) Biocompatible material Silastic MDX-4210 (b) Encased antenna [3]

Another issue related with the patient safety is the Specific Absorption Rate (SAR). SAR is the electromagnetic energy (dW) absorbed in the body per unit time (dt) and per unit mass (dm) when exposed to radio frequency electromagnetic field and expressed as [36]:

$$SAR = \frac{d}{dt} \left(\frac{dW}{dm} \right) = \frac{d}{dt} \left(\frac{dW}{\rho dV} \right) \quad (1.1)$$

SAR is expressed in units of watts per kilogram (W/kg). The power absorbed by the human body in the presence of an incident electromagnetic field is given by [4]

$$P_{abs} = \frac{1}{2} \int \sigma |E|^2 dV \quad (1.2)$$

where σ is the conductivity of the human tissues and $|E|$ is the intensity of the electric field inside the body.

In order to prevent the harmful effects due to the tissue heating, the standards for SAR are regulated by Institute of Electrical and Electronics Engineers (IEEE). According to IEEE C95.1-1995 standard, maximum 1-g averaged SAR should not be larger than 1.6 W/kg [36].

1.3 Literature Survey on Implantable Antennas for Biomedical Telemetry

In 2004, one of the first implantable antenna design which is used for biotelemetry applications was presented [4]. The spherical Dyadic Green's Function (DGF) expansions and Finite Difference Time Domain (FDTD) code were applied to analyze dipole antennas. A dipole antenna ($\lambda_d/2$) which operates at 402 MHz was inserted into a lossy dielectric sphere ($\epsilon_r = 49$, $\sigma = 0.6$ S/m) and an anatomical head model. The normalized far field patterns, radiated power and radiation efficiency of the antennas were observed. It was concluded that a large portion of human body should be included in the FDTD simulations to obtain correct field distributions. Kim and Rahmat-Samii also analyzed the

resonant characteristics of the low-profile implanted antennas. Two types of antennas, namely spiral type microstrip and PIFA, were designed for the MICS band operation. It was observed that PIFA has higher radiation efficiency than the microstrip antenna. After this study, other researchers have studied various types of dipole antennas for biomedical applications in [37], [38], [39]. On the other hand, many research groups focused on microstrip based PIFA configurations since they have compact small size, easy fabrication processes and flexibility in design.

Soontornpipit analyzed spiral and serpentine microstrip antennas for communication with medical devices in 402-405 MHz ranges [31]. As an initial antenna model, the design in [4] was utilized. The antenna was embedded in 2/3 human muscle block ($\epsilon_r = 42.807$, $\sigma = 0.6463$ S/m) and simulated using FDTD method. Several parametric studies were conducted to understand the performance of a microstrip antenna when implanted in lossy material. As a design strategy, first choosing the substrate and superstrate materials, then optimizing the length of the antenna was suggested.

In 2008, Karacolak et. al. designed a serpentine PIFA that operates in both MICS and ISM bands [1]. After the initial design of the antenna, it was optimized by combining an in-house finite element boundary integral electromagnetic simulation code and particle swarm optimization algorithm. RO3210 ($\epsilon_r = 10.2$, $\tan\delta = 0.003$ S/m) was preferred for substrate and superstrate material due to its high permittivity. Antenna was embedded in skin tissue and measured skin properties are used from [19] during simulations. Moreover, a three layer tissue model (skin, fat, muscle) was developed and the return loss of one-layer (skin) and three layer models are compared. A significant change was not observed in resonant characteristics. In order to test the designed antenna, skin mimicking phantoms are developed for both MICS and ISM bands. For the ISM band, the conductivity of the phantom ($\sigma = 2.27$ S/m) was found slightly higher than the conductivity of the skin ($\sigma = 1.4407$ S/m). The maximum simulated gain of the antenna is found as -26 dBi at 402 MHz.

A dumbbell-shaped and H-shaped cavity slot antennas which operate in the

ISM band (2.45 GHz) were also proposed in [40] and [5], respectively. Antennas are designed to operate in human arm and 2/3 muscle block is used in the simulations. A cavity slot antenna is preferred since it has a merit of high miniaturization and it is mechanically robust.

To reduce the effect of frequency shift in human tissue and to improve the tolerance of human tissue environments, antennas having wide impedance bandwidth were studied. In [41], a compact π -shape with a double L-strips PIFA was proposed for the MICS band. The wide-bandwidth performance is achieved by combining two close resonant frequencies which correspond to the double L-strips. In [42], dual band (MICS and ISM) implantable planar inverted-F antenna design was presented. Utilizing the two spiral antennas coupled with each other, a wide impedance bandwidth was achieved. In [43], a dual band implantable PIFA was studied. Three closely spaced resonant frequencies were created by adding open-end slots in the ground plane. For aforementioned designs, antennas were fabricated on the RO3210 substrate. The return loss values were simulated in High Frequency Structure Simulator (HFSS) and measured with skin simulating fluid. The maximum simulated gain values were found as -31.5 dBi, -27 dBi, and -28 dBi, respectively. The gain values were observed lower than the one presented in [1] due to size reduction of the antennas.

To reduce the size of the antennas and enhance the impedance bandwidth stacked structures are widely used. In [44], a three layer hook-slotted shape stacked PIFA was designed for MICS band. Proposed antenna were implanted into different tissues such as muscle ($\epsilon_r = 58.8$, $\sigma = 0.84$ S/m), heart ($\epsilon_r = 66$, $\sigma = 0.97$ S/m), eye tissue ($\epsilon_r = 57.7$, $\sigma = 1$ S/m) and simulated return loss values are observed to be less than -10 dB. In [45] and [46], stacked antennas operating in the MICS band were studied for wide bandwidth operation. Meandered stacked PIFA and hook slotted PIFA configuration were used, respectively. It was observed that higher bandwidth is achieved using the latter configuration (122 MHz). In [6], a miniature antenna was designed for integration in head-implanted medical devices operating in the MICS and ISM (433.1–434.8, 868.0–868.6 and 902.8–928.0 MHz) bands. Meandered stacked PIFA structure with a parametric model was preferred due to its compact size. Antenna sim-

ulations were conducted in skin tissue simulating cube phantom in the HFSS. For aforementioned stacked antennas, large scale miniaturization was achieved by lengthening the current flow path through the utilization of different layers of the stacked structure.

In [7], a miniaturized circularly polarized microstrip patch antenna was designed for the ISM band biomedical applications. Circularly polarized radiation was desired to eliminate the effect of multipath distortion and achieve improvement in the bit error rate. A square patch antenna with a center-square slot was loaded capacitively to reduce the patch size. Simulated impedance and axial ratio were studied using cubic skin phantom in HFSS.

Stacked multilayers and PIFA structures were usually covered with superstrates for the purpose of improving the bandwidth of the antennas and reducing the human tissue erosion [47]. A nonsuperstrate implantable CPW-fed monopole antenna operating in the MICS band was proposed in [8]. By the use of screen-printing technique and Ag/Pd paste, implantable antennas were printed on bio-compatible high dielectric constant ceramic substrate. In [48], another non-superstrate patch based implantable antenna operating in dual band (MICS and ISM) were proposed. Both antennas were simulated using HFSS in a skin model. Both designs achieved wide measured bandwidths in the MICS band, 130 MHz and 278 MHz, respectively.

Implantable antennas designed for the realization of complete implantable device were also studied. A conformal implantable antenna working in both the MICS and ISM (2.4-2.5 GHz) bands were proposed in [21]. The antenna was designed with required active components and bio-sensors to form a complete implantable wireless telemetry system. Multilayer spiral model antenna was fabricated using four dielectric substrates (RogerTMM10, alumina) and inserted in the bio-compatible insulation. A homogeneous cylindrical body phantom with muscle equivalent dielectric properties was used in HFSS analysis. Simulated maximum gain values were found as -28.8 and -18.5 dBi in the MICS and ISM band, respectively. In [49], a differentially fed dual band implantable antenna was proposed for neuro-microsystem. Structurally symmetrical spiral shaped

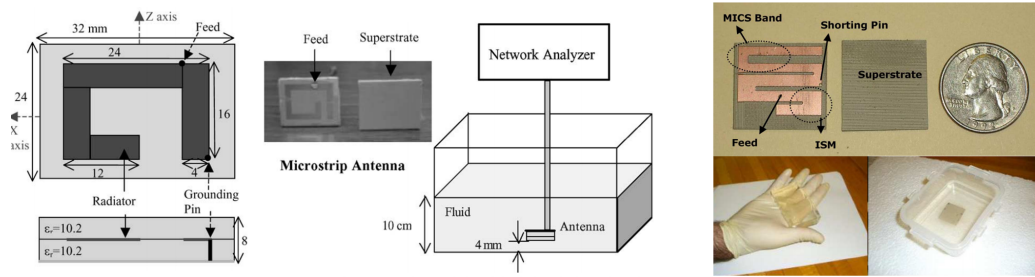
antenna was fabricated on Rogers6010 ($\epsilon_r = 10.2$, $\tan\delta = 0.0023$ S/m), covered by a superstrate with the same material. Simulated impedance and characterization of the communication link were studied using one layer skin tissue model in HFSS.

Examples of the referenced antennas are presented in Figure 1.4. The comparison of the implantable patch antennas reported in the literature with respect to operating bands, implantation cite, antenna types, occupied volume, 10 dB impedance BW and simulated maximum gain values are given in Table 1.4.

1.4 Scope of the Thesis

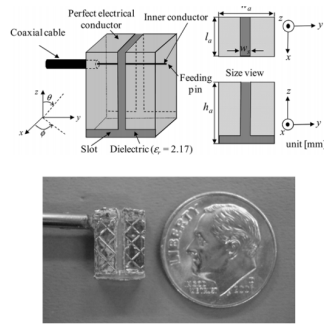
In this thesis, numerical and experimental analysis of a dual band (Medical Implant Communications Service-MICS; 402 – 405 MHz, Industrial, Scientific and Medical-ISM; 2.4 – 2.48) implantable antenna are presented. In aforementioned studies, implantable antennas were designed however a design methodology and intuition behind the miniaturized antennas were not provided clearly. In this study, each design step of the antenna operation mechanism is explained step by step. Therefore, the scope of this thesis can be listed as:

- Develop clearly explained step-by-step design methods for miniaturized antennas
- Conducting the numerical study of antenna design in tissue models
- Develop miniaturized antennas operating in tissue
- Performing simulation studies on different phantom models
- Preparing tissue mimicking phantoms
- Conducting experimental setup to validate the proposed design

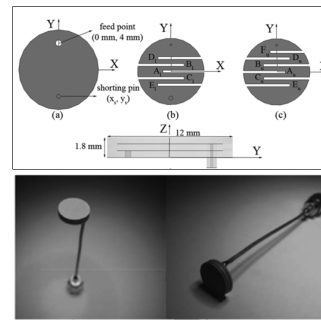


(a)

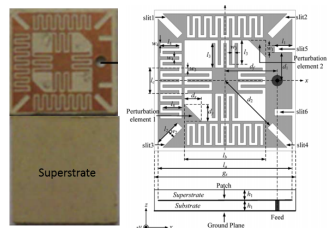
(b)



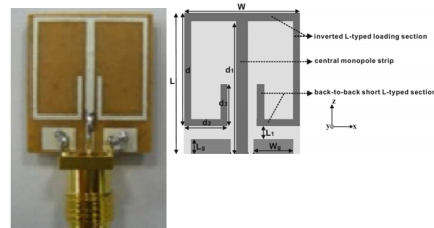
(c)



(d)



(e)



(f)



(g)

Figure 1.4: Examples of implantable antennas: (a) Spiral PIFA [4] (b) Meandered PIFA and skin mimicking phantom [1] (c) Cavity slot antenna [5] (d) Meandered stacked patch antenna [6] (e) CP Antenna [7] (f) Nonsuperstrate antenna [8] (f) Pyramidally stacked patch antenna [9]

Table1.4: Comparison of the implantable patch antennas reported in the literature with respect to operating bands, implantation cite, antenna types, occupied volume, 10 dB impedance BW and simulated maximum gain values.

Ref	Band	Tissue	Antenna Type	Antenna Size (mm)	BW (MHz)	Gmax (dB)
[4]	MICS	Skin	Spiral Patch	32x40x8	20	-
[31]	MICS	2/3 Muscle	Spiral PIFA	26.6x16.8x6	28	-
[1]	MICS, ISM	Skin	Meandered PIFA	22.5x22.5x2.5	142, 173	-25, -9
[5]	ISM	2/3 Muscle	H-shaped Cavity Slot	2.8x4x1.6	670	-22.3
[41]	MICS	Skin	Pi-shaped PIFA with double L strips	22.5x22.5x1.27	80	-25
[42]	MICS, ISM	Skin	Spiral PIFA	16.5x16.5x2.54	52, 110	-31.5, -10
[43]	MICS, ISM	Skin	Open end slot PIFA	19x19.4x1.27	254, 110	-28, -22
[44]	MICS	Skin	Hook-Slotted Circular Stacked PIFA	$\pi \times (7.5)^2 \times 1.9$	50	-26
[45]	MICS	Skin	Slotted Stacked Patch	10x10x1.9	50	-26
[46]	MICS	Skin	Hook Slotted	8 x 8 x 1.9	122	-38
[6]	MICS	Skin	Meandered Circular PIFA	$\pi \times 6^2 \times 1.8$	27	-37
[7]	ISM	Skin	Capacitively loaded Patch	10x10x1.27	190	-21
[8]	MICS	Skin	CPW-fed monopole with L loading	18x16x1.4	130	-26
[48]	MICS, ISM	Skin	Spiral Shaped Patch	18x16x1.27	278, 870	-26, -19
[9]	MICS, ISM	Muscle	Pyramidal Spiral Patch	2477 mm ³	10, 147	-28.8, -18
[49]	MICS	Skin	Differantially fed dipole	27x14x1.27	30	-

1.5 Thesis Organization

In Chapter 2, patch based implantable antenna design which operates in MICS band is presented. Antenna miniaturization techniques are discussed. A prototype antenna is designed using the commercial Finite Element Method (FEM) based HFSS solver and experimental studies are conducted to validate the simulation results.

In Chapter 3, a small size ($2\text{ cm} \times 1\text{ cm} \times 3.81\text{ mm}$) implantable antenna which operates in both MICS and ISM bands is designed. Design procedure is explained clearly. Experimental studies are conducted for return loss measurement and far field telemetry in MICS and ISM bands.

In Chapter 4, patient safety, effects of different phantoms on the resonant frequency, effects of coaxial cable and far field properties of the electrically small antennas are analyzed. For each issue, the feasibility and limitations of the proposed antenna are explored.

CHAPTER 2

DESIGN OF PATCH BASED IMPLANTABLE ANTENNA IN MICS BAND

2.1 Introduction

Since the invention of the microstrip antennas, they have been widely used in military applications such as aircraft, missiles, rockets, space crafts and also in commercial applications such as mobile satellite communications, wireless communications and remote sensing. As shown in Figure 2.1, a conventional microstrip antenna consists of a patch and a ground plane which are separated by an insulating dielectric sheet called as substrate. Microstrip antennas have a number of advantages over other antennas; they are low profile, light weight, compact and conformable to the mounting structure, easily fabricated and integrable with solid-state devices [15]. Although the microstrip antennas meet some critical requirements, they have some operational disadvantages such as narrow frequency bandwidth, low power and low efficiency. Several techniques can be used to eliminate disadvantages of microstrip antennas such as, increasing the electrical length of the antenna, using a thick substrate, and using a superstrate that helps to increase the bandwidth [16, 50].

The substrate selection of the patch antenna depends on the application area. Thick substrates whose dielectric constant are low provides better efficiency and larger bandwidth. On the other hand, substrates whose dielectric constant are high can be used for miniaturization of the patch antenna. The relative dielectric constant of the substrate is usually $2.2 \leq \epsilon_r \leq 12$. Microstrip antennas can be

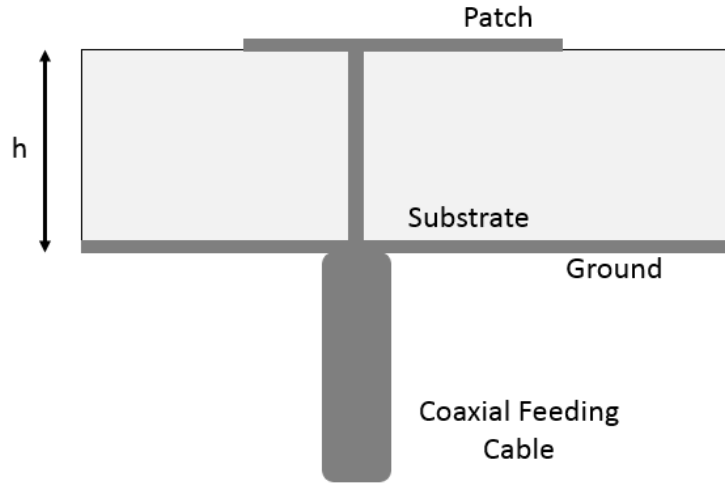


Figure 2.1: Side view of the basic patch model where h is the thickness of the substrate

fed in various configurations. The most common feeding methods are microstrip line, coaxial probe, aperture coupling and proximity coupling [51]. In this thesis study, coaxial-line feed, where the inner conductor of the cable is attached to the radiating patch while the outer conductor is connected to the ground plane, is preferred due to its compact structure.

2.1.1 Method of Analysis

It is important to develop analytical models to understand the limitations and improve the performance of patch antennas [51]. There are various analysis methods for microstrip antennas. The most popular methods can be listed as:

- i) Transmission Line Model [52], [10]
- ii) Cavity Model [52], [10], [53], [54]
- iii) Full Wave Model [55]

Among the aforementioned models, the transmission line model is the easiest one and it gives good physical insight. However, it is less accurate and more difficult to model coupling between the radiating slots [56]. Cavity model is more accurate than the transmission line model, but at the same time it is more complex. The full-wave models are very accurate, very versatile, and can treat

single elements, finite and infinite arrays, stacked elements, arbitrary shaped elements, and coupling. However they are the most complex models and usually give less physical insight [51].

The transmission line model is briefly explained in the next section since it provides a good understanding of radiation mechanisms of microstrip antennas and initial parameters for the antenna design. As full wave model, FEM based commercially available HFSS software is used to analyse the implantable antenna structures.

Transmission Line Model

Since the dimensions of the patch are finite along the length and width, the fields at the edges of the patch undergo fringing. Most of the electric field lines reside in the substrate and parts of some lines exist in air. Since some of the waves travel in the substrate and some in air, an effective dielectric constant ϵ_{reff} is introduced to account for fringing and the wave propagation in the line. The effective dielectric constant is defined as the dielectric constant of the uniform dielectric material so that it has identical electrical characteristics as the microstrip line at the interface between the dielectric substrate and air [51]. The effective dielectric constant is usually closer in value to that of the substrate than to that of air; this becomes even more effective as the dielectric constant of the substrate increases [57]. The effective dielectric constant for $w/h > 1$ can be calculated as [57]:

$$\epsilon_{reff} = \frac{\epsilon_r + 1}{2} + \frac{\epsilon_r - 1}{2} \left[1 + 12 \frac{h}{w} \right]^{-1/2} \quad (2.1)$$

where w is the width of the patch and h is the thickness of the substrate (See Figure 2.1 and Figure 2.3)

Due to the occurrence of the fringing at the edges of the patch, electrical length of the patch antenna looks greater than its physical dimensions. The extension of the patch length ΔL is given by [58]:

$$\frac{\Delta L}{h} = 0.412 \frac{(\epsilon_{reff} + 0.3) \left(\frac{w}{h} + 0.264\right)}{(\epsilon_{reff} - 0.258) \left(\frac{w}{h} + 0.8\right)} \quad (2.2)$$

Now, the effective length of the patch antenna can be written as

$$L_{eff} = L + 2\Delta L \quad (2.3)$$

For the dominant TM_{010} mode, the resonant frequency of the microstrip antenna is a function of its length. By taking into account the fringing effect, it is computed as

$$f_r = \frac{1}{2(L + 2\Delta L)\sqrt{\epsilon_{reff}}\sqrt{\mu_0\epsilon_0}} \quad (2.4)$$

In this chapter, the basic characteristics of the microstrip antennas are investigated to understand the operation mechanism. First, a patch antenna is designed that radiates into air, then an implantable patch antenna is designed that radiates into skin. For both antennas, MICS band is preferred as the operating frequency band.

2.2 Design of a Patch Antenna in the MICS Band (402-405 MHz) Radiating into Air

To design a patch antenna which operates in the MICS Band (402-405 MHz) in air, initial parameters are determined according to transmission line model. Design procedure is outlined as follows [51]:

1. Specify:

Dielectric constant of the substrate (ϵ_r),

The resonant frequency (f_r , in Hz),

Height of the substrate (h)

2. Determine:

Width of the patch (W),

Length of the patch (L)

The substrate is chosen as Rogers3210 ($\epsilon_r = 10.2, \tan\delta = 0.003$) which has been widely used for implantable antenna design due to its high dielectric constant [47]. The thickness of the substrate is 1.27 mm and the resonant frequency of the antenna is determined as 402 MHz.

The width of the patch is calculated by [51]:

$$W = \frac{1}{2f_r\sqrt{\mu_0\epsilon_0}}\sqrt{\frac{2}{\epsilon_r + 1}} = \frac{c}{2f_r}\sqrt{\frac{2}{\epsilon_r + 1}} \quad (2.5)$$

where c is the speed of light.

Then, the effective dielectric constant of the microstrip antenna is determined using equation 2.1. The extension of the length ΔL is found using equation 2.2 once the width of the patch, thickness of the substrate and the effective dielectric constant are known. Finally, the length of the patch antenna is determined as follows [51]:

$$L = \frac{1}{2f_r\sqrt{\epsilon_{ref}}\sqrt{\mu_0\epsilon_0}} - 2\Delta L \quad (2.6)$$

As a feeding mechanism, coaxial feeding is preferred since coaxial transmission lines are not influenced by immersion in dielectric materials. Also, it is easier to interface to the test equipment. The approximate feed position that provides a good impedance matching for an input impedance of 50Ω is determined by using the following formulas [59]:

$$y_f = \frac{W}{2} \quad \text{and} \quad x_f = \frac{L}{2\sqrt{\epsilon_{ref,L}}} \quad (2.7)$$

where x_f and y_f are feed positions in x and y directions, respectively measured from the corner of the patch as shown in Figure 2.3. Using this design procedure,

the initial antenna parameters are calculated and listed in Table 2.3. Based on the calculated parameters, antenna model is created and simulations are carried out using HFSS software. A coaxial probe is used to feed the structure, where the inner conductor of the coaxial is attached to the radiating patch, while the outer conductor is attached to the ground plane. The simulated return loss is shown in the Figure 2.2.

Table2.1: Design parameters of the initial patch antenna which operates in the MICS Band

Initial Parameters	
Resonant Frequency	402 MHz
Substrate	Rogers3210
Substrate Thickness	1.27 mm
Width of the Patch (W)	15.7678 cm
Length of the Patch (L)	11.8039 cm
Feed Position (x_f, y_f)	(1.822 cm, 7.8839 cm)

Table2.2: Design parameters of the initial patch antenna which operates in the MICS Band

Resonant Frequency	402 MHz	402 MHz
Substrate	Rogers3210	RO4003
Substrate Permittivity (ϵ_r)	10.2	3.38
Substrate Thickness	1.27 mm	1.52 mm
Width of the Patch (W)	15 cm	25 cm
Length of the Patch (L)	11 cm	20 cm

The initial parameters are optimized to get the best return loss performance around the centre frequency of the MICS band (403 MHz). Feed position is parametrically changed and the return loss is observed to obtain a good impedance matching for an input impedance of 50 Ω . However, when the feed position changes, the resonant frequency also changes slightly. To compensate the resonance frequency shift, the length of the antenna is rearranged. The optimized antenna parameters are listed in Table 2.1. The HFSS model and the related

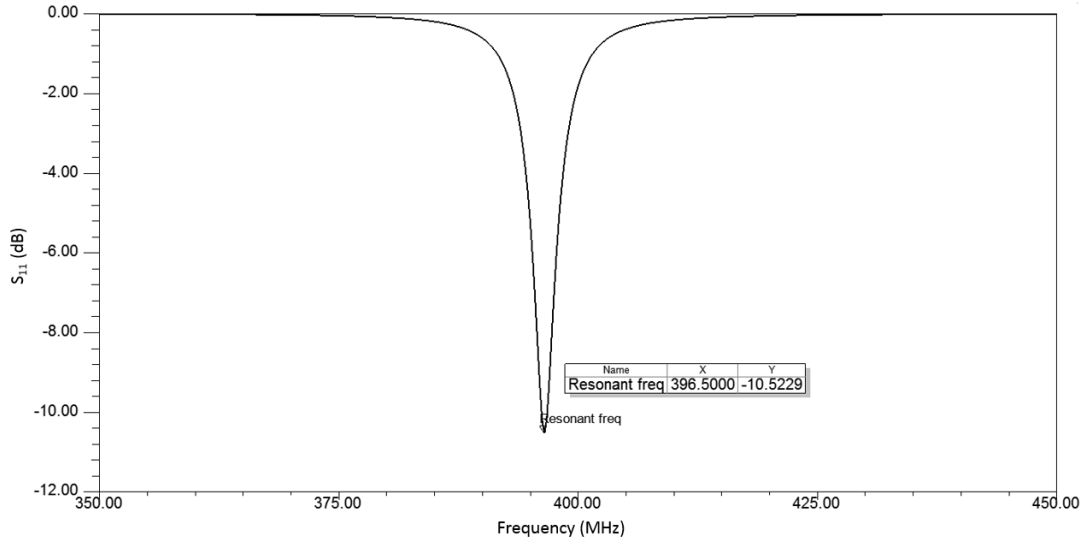


Figure 2.2: Return loss of the patch antenna designed according to the Table 2.3

antenna parameters are shown in Figure 2.3. Figure 2.4 shows the optimized simulated return loss. The simulated 3D directivity pattern at 403 MHz is given in Figure 2.5.

Table2.3: Design Parameters of Optimized Patch Antenna which Operates in the MICS Band

Optimized Parameters	
Resonant Frequency	402 MHz
Substrate	Rogers3210
Substrate Thickness	1.27 mm
Width of the Patch (W)	15.75 cm
Length of the Patch (L)	11.55 cm
Feed Position (x_f, y_f)	(3.125 cm, 7.875 cm)

When directivity and gain of the patch antenna are compared, it is observed that the maximum simulation values are 5.98 dBi and 1.96 dBi, respectively. Therefore, the radiation efficiency of the antenna is calculated approximately as 0.32 (Gain=Directivity \times Radiation Efficiency). It has been observed that radiation efficiency of the microstrip antenna depends primarily on the substrate

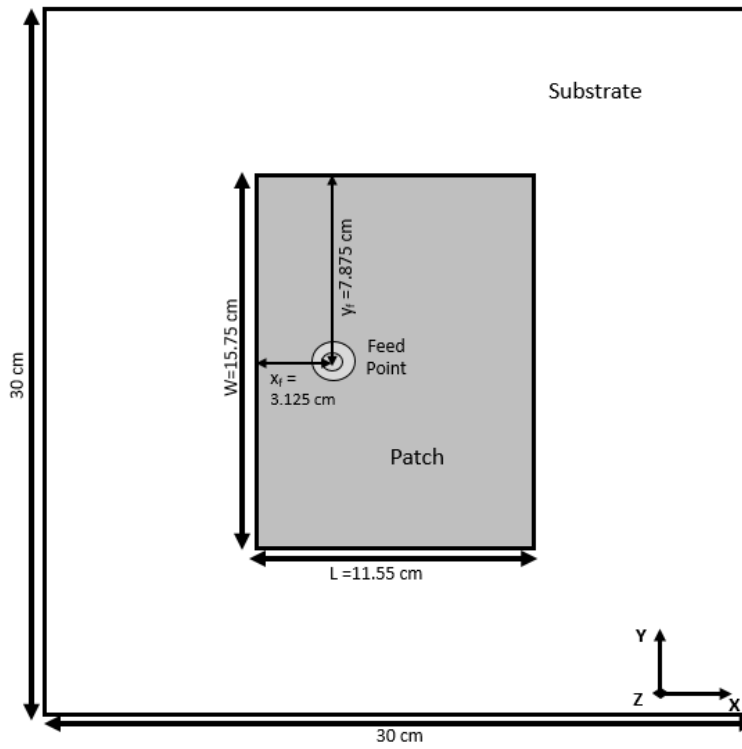


Figure 2.3: Top view of the simulated patch antenna: Antenna parameters are optimized to operate in the MICS band

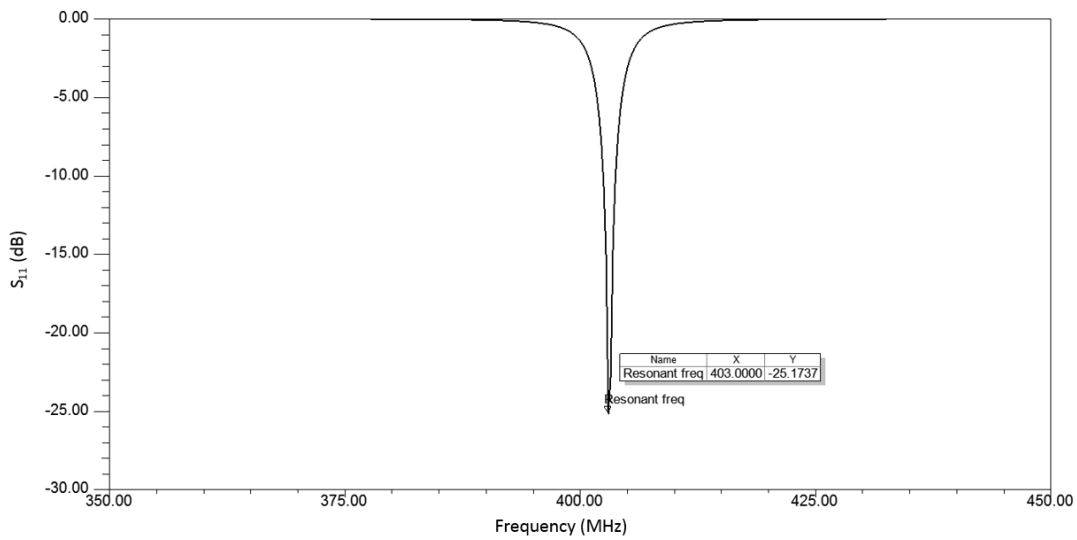


Figure 2.4: Return loss of the patch antenna operates in the MICS Band

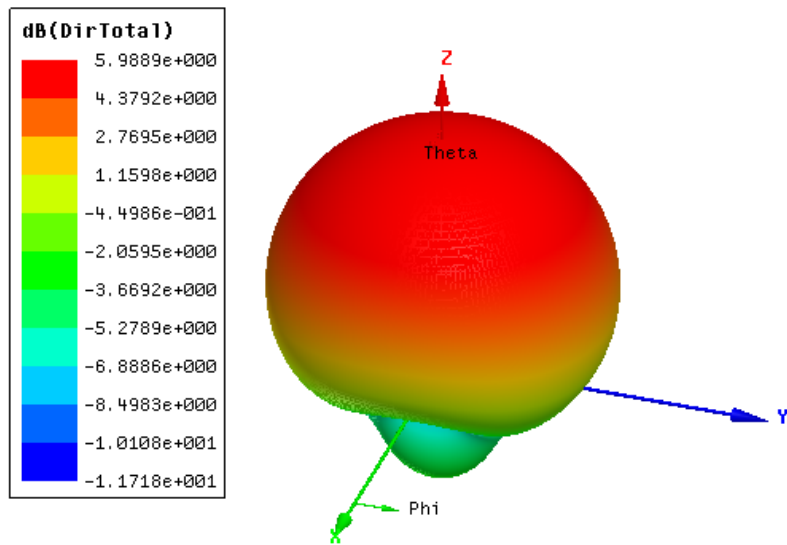


Figure 2.5: Simulated 3D directivity pattern of the patch at 403 MHz

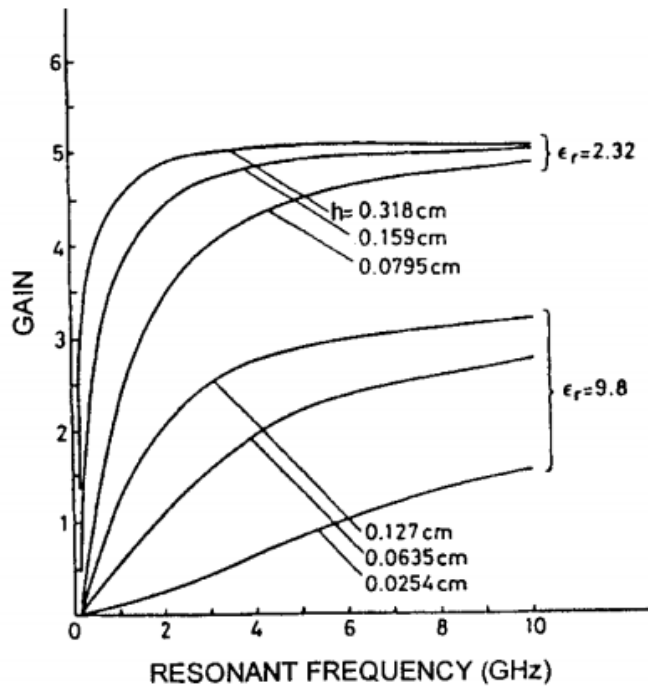


Figure 2.6: Gain as a function of resonant frequency, substrate permittivity and substrate thickness for the TM_{10} mode of a rectangular patch [10]

thickness and permittivity [60]. The gain variation with frequency and the thickness and height of the dielectric substrate is studied in [61]. A graph that summarizes the variation of gain with respect to frequency for two different dielectric constant and three different thickness values is reported in [61] and presented in Figure 2.6 for comparison. Note that gain decreases as substrate dielectric constant increases and frequency decreases. This happens since the surface wave power increases with ϵ_r . It is observed from Figure 2.6 that the simulated gain characteristics of the designed antenna (with $\epsilon_r = 10.2$, $h = 0.127$ cm and $f_r = 403$ MHz) is consistent with the literature.

2.3 Design of a Patch Antenna in the MICS Band (402-405 MHz) Radiating into Tissue

After designing the patch antenna that radiates into air and operates in the MICS band, it is decided to design a patch antenna in a tissue model. Generic 2/3 muscle block which is commonly preferred to represent average body properties is taken as tissue model to simplify the simulations [31]. The electrical properties are taken as 2/3 scale of the pure muscle tissue and found as $\epsilon_r = 42.807$, $\sigma = 0.6463$ S/m. First of all, the patch antenna model in air is inserted into tissue model. The dimensions of the tissue model are determined similar to tissue model in [2] and shown in Figure 2.7. The top and side view of the antenna and the tissue model in HFSS are illustrated in Figure 2.8.

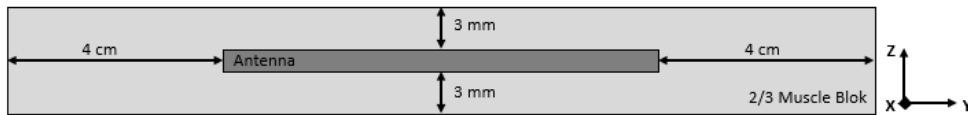
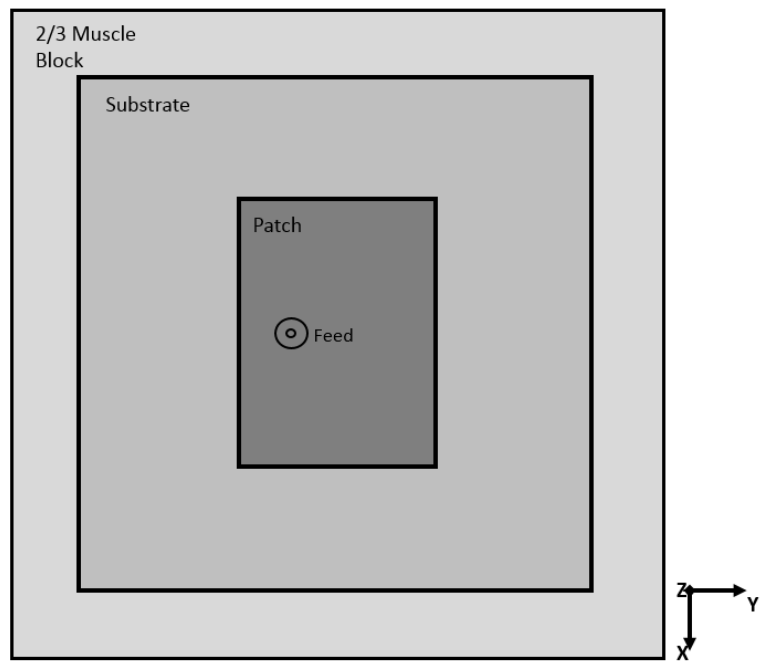


Figure 2.7: Patch antenna and tissue model proposed in [2]. Note that the dimensions are not scaled.

Because antenna is placed into a dielectric medium, the wavelength becomes shorter than the one in air and the effective electrical length of the antenna



(a)



(b)

Figure 2.8: HFSS Model of the patch antenna inserted in 2/3 muscle block (a) Side view (b) Top view

increases. As a result, the resonant frequency shifts below 403 MHz. The simulation result for the return loss of the patch is given in Figure 2.9. Frequency shift is observed as expected. In addition, due to the presence of surrounding dissipative biological tissue, the antenna suffers from poor impedance matching.

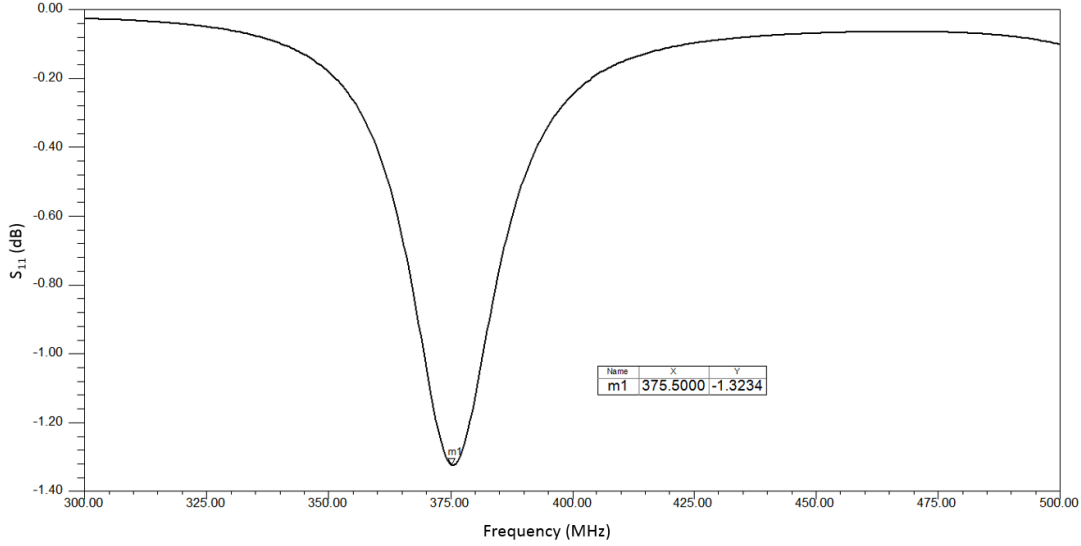


Figure 2.9: Return loss of the patch antenna which is inserted into 2/3 muscle block

Figure 2.10 represents the simulated three-dimensional far field pattern at 402 MHz. Note that the gain value do not account for impedance mismatch losses and due to the near field coupling with lossy tissues, radiation efficiency is extremely low ($\eta = 0.02$ with Gain = -11 dBi). To understand the physical phenomena for antennas in lossy matter, consider the following expression [21]:

$$P_{source} = P_{rad} + P_{abs} = \int_{S_r} Re\{\vec{S} \cdot \vec{r}\} dS + \frac{w}{2} \int_V \varepsilon_0 \varepsilon_e'' |E|^2 dV \quad (2.8)$$

where P_{rad} is the average power flow through a spherical surface S_r of a volume V in which the power absorption, P_{abs} occurs, \vec{S} is the Poynting vector ($\frac{1}{2} \vec{E} \times \vec{H}^*$), w is the angular frequency and ε_e'' is the imaginary part of the effective permittivity ($\varepsilon_e = \varepsilon_0(\varepsilon_e' - j\varepsilon_e'')$). Equation 2.8 can be expressed as sum of Far Field (FF) and

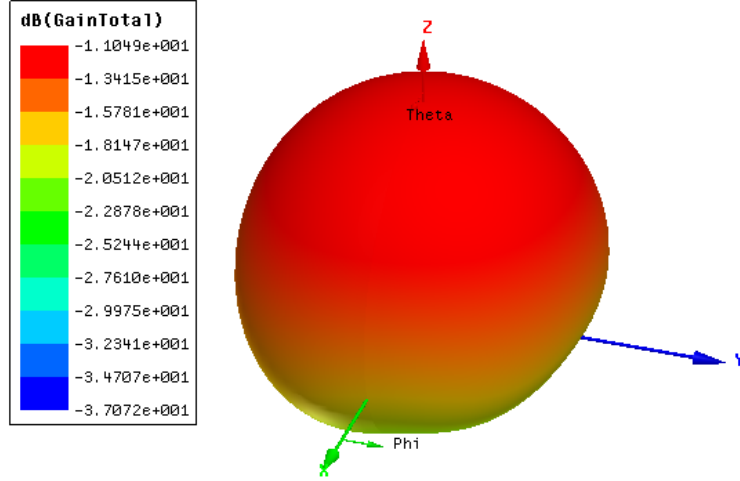


Figure 2.10: Simulated three-dimensional far field pattern of patch antenna at 403 MHz which is inserted into 2/3 muscle block

Near Field (NF) components as follows:

$$\begin{aligned}
 P_{source} &= \int_{S_r} \text{Re}\{\vec{S}(1/r^2) + \vec{S}(1/r^n)\} \cdot \vec{r} dS + \frac{w}{2} \int_V \epsilon_0 \epsilon_e'' [|\vec{E}|^2 (1/r^2)] \\
 &= P_{rad-FF} + P_{rad-NF} + P_{abs-FF} + P_{abs-NF}
 \end{aligned} \tag{2.9}$$

where S is the Poynting vector, the $1/r^2$ indicates far field and $1/r^n$, with $n > 2$, indicates near field components. P_{rad-FF} , P_{abs-FF} are the radiated power and the absorbed power in far field and P_{rad-NF} , P_{abs-NF} are the radiated power and the absorbed power in near field. The near field is mainly reactive in a free space, therefore, it affects neither the radiated power nor the absorbed power. However, when antenna is inserted into a lossy matter, near field strongly couples with the closest surrounding material resulting in power loss. Comparing the gain values of the patch antenna that radiates into air ($G_{air} = 1.96 \text{ dBi}$) and tissue ($G_{tissue} = -11 \text{ dBi}$), the power loss arising from the tissue loading is observed as approximately -13 dBi .

2.3.1 Electrically Small Antenna Design

In the previous considerations, antenna is inserted into lossy medium without any size limitation. However, implantable antennas require extreme miniaturization to fit in implanted device. Ideally implants are in the range of 1 to 10 mm in diameter for a length of 5 to 35 mm [34]. However, free space wavelength in the MICS band is approximately 74 cm and 12 cm in the ISM band. This leads to the electrically small antenna design with antenna size limitations of $\lambda_0/30$ and $\lambda_0/5$ for the MICS and ISM bands, respectively.

When considering the physical and electrical size of the antenna, antenna's electrical size is defined in terms of its occupied volume relatively to the operating wavelength [62]. Antenna whose overall occupied volume is such that $ka \leq 0.5$ is defined as electrically small antenna where k is the free space wave number ($2\pi/\lambda$), and a is the radius of the sphere enclosing the maximum dimension of the antenna [11]. This spherical enclosure is called as "*Chu sphere*" (Figure 2.11). However, these definitions cover lossless miniature antennas radiating into free space and are not applicable for implantable antennas [21]. When analysing implantable antennas, field coupling with lossy tissues and radiated EM wave are affected from the body model. Therefore, it is more complex to specify the antenna and identify the minimum circumscribing sphere.

2.3.2 Antenna Miniaturization Techniques

Despite the differences between the classical electrically small antenna description, implantable antennas still have electrically small antenna problem and the size reduction must be applied while maintaining adequate electromagnetic performance. In this section, basic antenna miniaturization techniques are briefly discussed. For each section, example antennas and their results are presented.

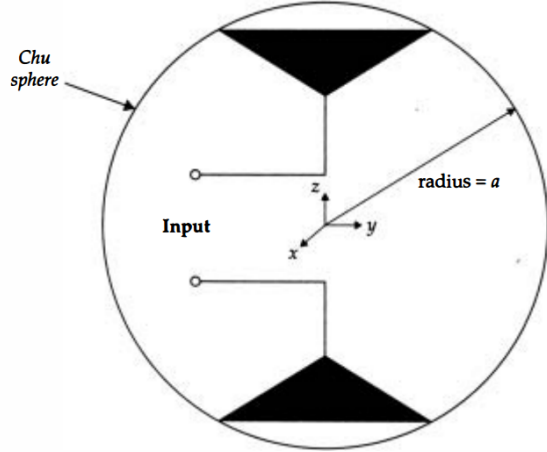


Figure 2.11: Chu sphere of radius "a" centered about the origin. The *Chu sphere* is the minimum circumscribing sphere enclosing the antenna of maximum dimension $2a$ [11]

i) Loading the Substrate with High Dielectric Constant Material

Recall that, the resonant frequency for the fundamental mode rectangular patch can be expressed as:

$$f_r = \frac{1}{2(L + 2\Delta L)\sqrt{\epsilon_{reff}}\sqrt{\mu_0\epsilon_0}} \quad (2.10)$$

Note that the resonant frequency decreases, when the effective permittivity increases. To see the affect of the substrate permittivity on the resonant frequency, two substrates (RO4003 and RO3210) are taken as sample and their resonant frequencies are observed. First, it is assumed that patch antenna is printed on a RO4003 substrate ($\epsilon_r = 3.38, h = 1.52$ mm). The dimensions of the patch antenna is calculated approximately as $L = 25$ cm, $w = 20$ cm for operation in the MICS band ($f_{res} = 402$ MHz). Then, antenna dimension are calculated according to RO3210 ($\epsilon_r = 10.2, h = 1.27$ mm) substrate and found as $L = 15$ cm, $w = 11$ cm. When the total area of the patch is considered, nearly 33% size reduction occurs. This shows why RO3210 substrate is commonly used in implantable patch antenna design. Note that when using substrate with permittivity higher than 10.2, designer must be careful since the radiator starts to lose its radiation efficiency [15].

ii) Usage of Shorting Pin

One of the techniques to reduce the size of a microstrip patch antenna is to short-circuit the edge of the patch with a shorting wall or plane. This procedure produces the same frequency response at half the size of a similar antenna without the shorting pin [63,64]. These type of antennas are called as Planar Inverted-F antennas (PIFAs) since the side view of the antenna looks like an upside down letter F as shown in Figure 2.12. Basically, a PIFA can be considered

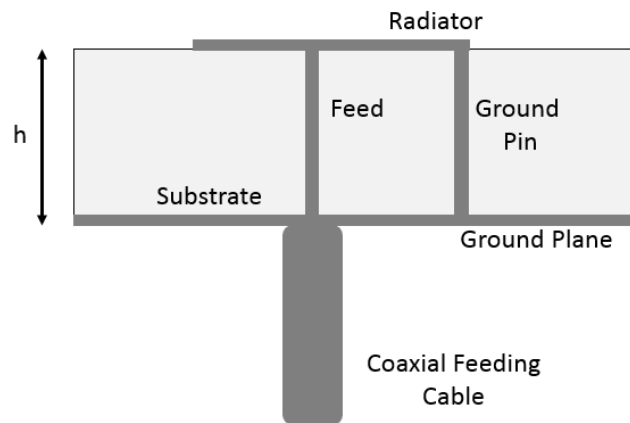


Figure 2.12: Side view of a planar inverted-F antenna (PIFA)

as a modification of a microstrip patch antenna where the radiating patch of the antenna is halved at its midline by a short-circuiting wall [12]. If the width of the shorting wall is further reduced to a narrow shorting strip, the PIFA is formed as shown in Figure 2.13.

The operation mechanism of the PIFA can be understood by examining the electric field distribution on the radiating surface. For the half wave rectangular patch antenna, maximum electric field occurs at one of the radiating edges and zero electric field occurs at the centre. Since the electric field is zero at the plane $x = L/2$, an electric wall can be inserted without perturbing the field distribution in the excited half of the patch. The patch is still expected to resonate at the design frequency with a quarter wavelength distance ($\lambda_g/4$) between the

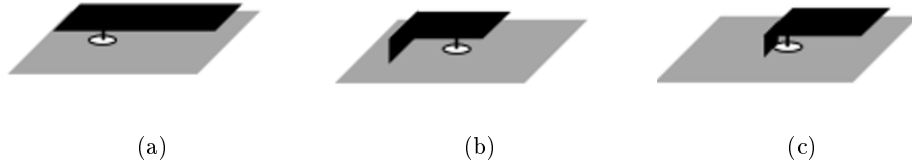


Figure 2.13: Development of PIFA from microstrip antenna (a) Microstrip antenna (b) Microstrip antenna with a shorting wall (c) PIFA with a narrow strip [12].

radiating edge and the electric wall. Such a shorting plane can be realized using shorting pins or vias (through hole plating) connected between the patch metallization and ground plane. However, this method introduces a rise to residual inductance at the shorting edge [65]. Therefore, the feed position and the feed length need to be re-adjusted to account for the inductance. Figure 2.14 represents half wavelength long patch antenna with E-field distribution and PIFA with shorting pins.

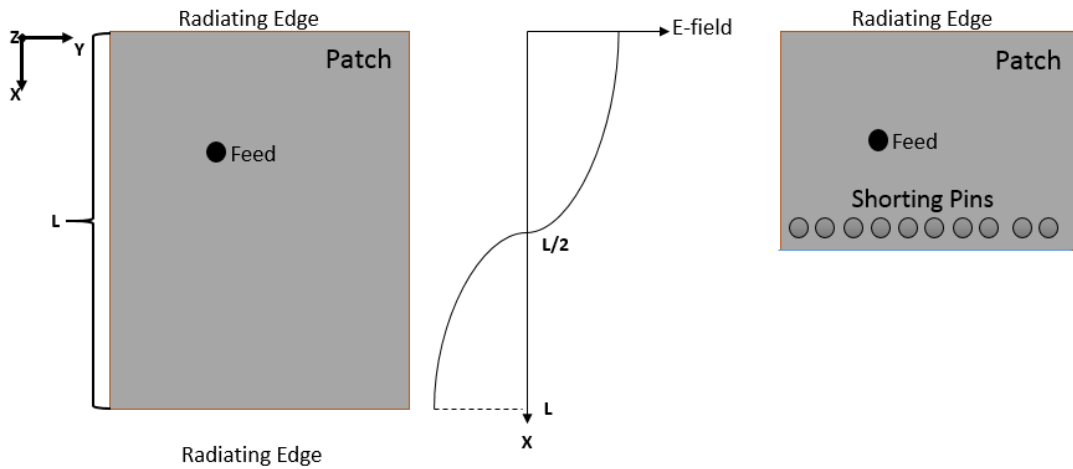


Figure 2.14: Derivation of the quarter wave patch from patch antenna with the electric field distribution

The number and position of the shorting pins affects the resonance frequency of the patch antenna. Since the current path becomes longer, the largest reduction in operating frequency is obtained when the shorting pin is inserted into the corner of the patch [13]. Figure 2.15 represents the results taken from [13]. The

frequency reduction for two planar inverted-F antennas (PIFA) with shorting pins inserted in the middle of the patch and the corner of the patch are illustrated. Note that the most compact antenna with a lowest frequency value is obtained when the shorting pin is in the corner.

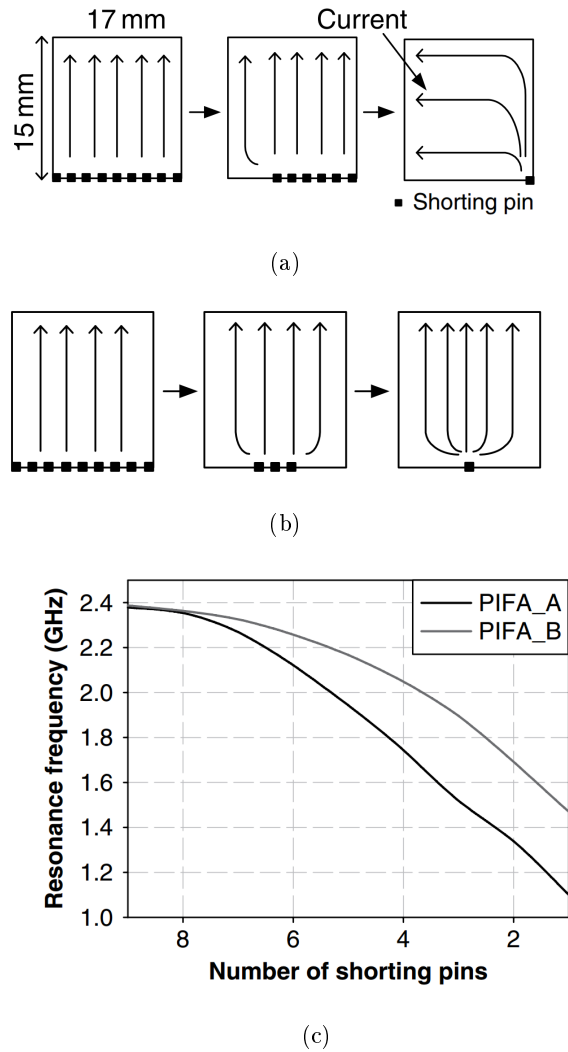


Figure 2.15: Effect of reducing the number of shorting pins in a quarter-wavelength patch to form a planar inverted-F antenna (a) PIFA_A: Shorting pins are at the corner of the radiating surface (b) PIFA_B: Shorting pins are at the middle of the radiating surface (c) Change in resonant frequency [13].

iii) Meandering the Patch

Another technique to reduce the size of the antenna is to increase the length of the current path by meandering the patch. To understand this technique, firstly monopole wire antennas are investigated. Then, compact patch antenna examples utilizing both shorting pin and meandering techniques are inspected.

As mentioned before, optimizing the impedance of the antenna to match the transmitter or receiver is one of the most important performance characteristics of small antennas [15]. For an electrically small monopole antenna with overall height $h \ll \lambda$, the feed point resistance is given as [51]:

$$R_r^m = 40\pi^2 \left(\frac{h}{\lambda}\right)^2 \quad (2.11)$$

The feed point reactance can be written as $X(w) = wL - 1/wC$, where L is the equivalent feed point inductance of the antenna, C is the equivalent feed point capacitance of the antenna and w is the angular frequency. Note that $1/wC$ term dominates at low frequencies. To prevent the use of external reactive components and achieving self-resonance at low frequencies, the equivalent feed point inductance can be increased until $wL = 1/wC$. To increase the self inductance, the total wire length must be increased. When increasing the wire length for a fixed height, the antenna geometry plays an important role on the resonant frequency. Best and Morrow studied the resonant frequency of linear wire antennas of fixed size and wire diameter [14]. The authors considered two simple meander antennas, namely M2 and M4, and their equivalent inductance models as shown in Figure 2.16. These antennas had an overall height of 10 cm, total wire length of 14 cm and wire diameter of 0.5 mm. The resonant frequency was determined as 600.7 MHz for M2 antenna and as 625 MHz for M4 antenna using EZNEC software [66]. Using the equivalent inductive circuit models, the resonant frequencies of the M2 and M4 antennas were calculated as 617.8 MHz and 630.1 MHz, respectively [67]. The critical aspect is that the equivalent inductor model does not account for the effective coupling between the meander line sections, however, the coupling has a significant role in determining the resonant frequency of meander antennas.

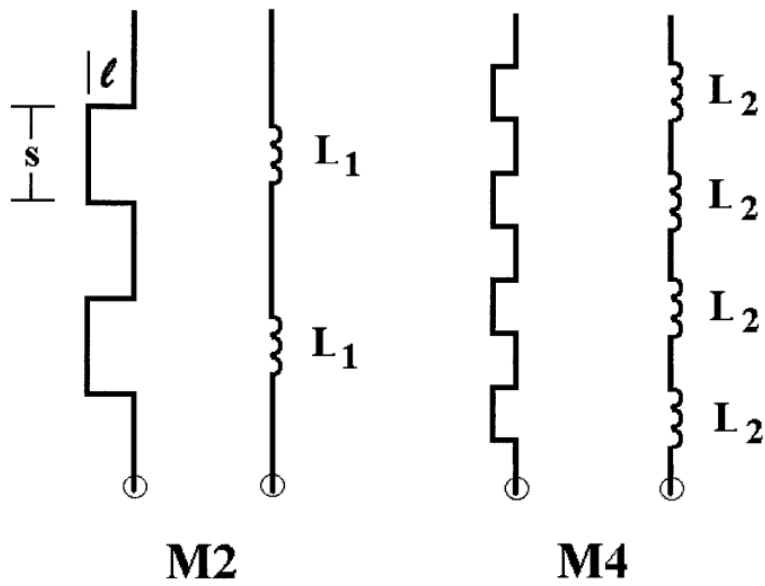


Figure 2.16: Meander line antennas with equivalent inductance models where s is the spacing and l is the length of the meander section. L_1 and L_2 represents the equivalent inductance of the each section [14]

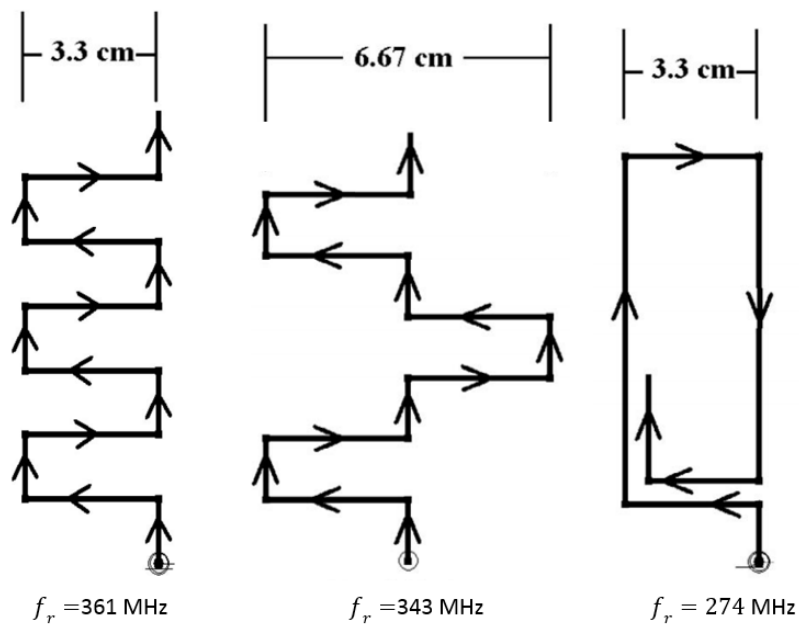


Figure 2.17: Resonant frequency of meander line antennas with different geometries [15]

The resonant frequency and current distribution of three meander antennas with overall height of 10 cm, total wire length of 30 cm, meander line section length of 3 cm and a conductor diameter of 1 mm are represented in Figure 2.17.

It is observed that, in regions where current vectors oppose in parallel sections of wire, the effective self inductance of the wire is decreased, whereas in regions where current vectors reinforce in parallel sections of wire the effective self inductance is increased. Therefore, altering the spacing between the parallel sections of wire aids in lowering the resonant frequency of the antenna.

Same approach in monopole wire antennas are also valid for printed antennas. To lower the fundamental resonant frequency of the microstrip antenna, the excited patch surface current paths in the antenna's radiating patch can be meandered [17]. For rectangular patch antenna, narrow slits are inserted at the non-radiating edges of the patch. In this way, the surface currents of the patch are effectively meandered resulting in lengthened current path and lowered resonant frequency for a fixed patch dimension. Figure 2.18 shows surface current distributions for meandered patch and bow-tie shaped patch antenna.

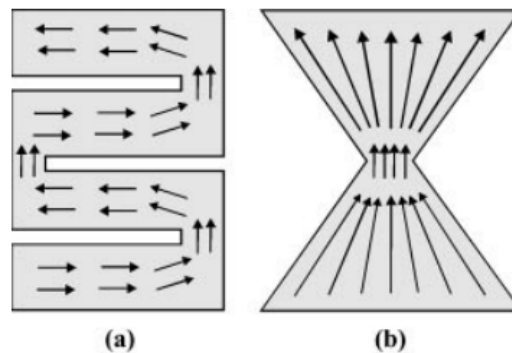


Figure 2.18: Surface current distributions for meandered rectangular microstrip patches with (a) meandering slits and (b) a pair of triangular notches cut at the patch's nonradiating edges [16]

First compact design in the literature which combines the patch meandering and shorting-pin loading techniques is presented in this part. Dey et al. achieved to design a compact microstrip patch antenna with a length of approximately

one-eighth of the effective wavelength [17]. Figure 2.19 shows the schematic of the antenna.

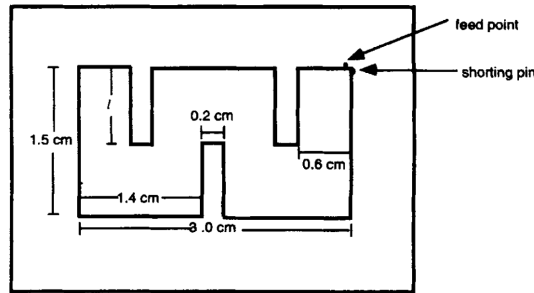


Figure 2.19: Schematic of the compact microstrip patch antenna [17]

The effect of the slot length (l) on the resonant frequency was observed and the results reported in [17] are displayed in Figure 2.20. Resonant frequency of the patch antenna was lowered as the current path increases as expected. In addition, Dey analysed the current distribution on the patch surface at resonance using method of Moments (MoM) to gain an understanding of the physical behaviour of the new kind of patch antenna and illustrated in Figure 2.21. It is noticed that resonant frequency decreases as the current path increases.

iv) Patch Stacking

Stacked structures are widely used to minimise and enhance the bandwidth of the antennas. Huang et. al. studied the example of a stacked short circuited PIFA for the MICS and ISM bands [18]. Designed antenna consisting of 4 substrate layers which were connected using vias are presented in Figure 2.22. The effective length of the current path was lengthened using the radiating surfaces at different layers. The current distribution on the radiating surface of the antenna at 402 MHz was reported in [18] and shown in Figure 2.23. It is observed that current flows through the stacked layers by efficiently using the available volume. Since the length of current flow path increases, the resonant frequency is reduced [44].

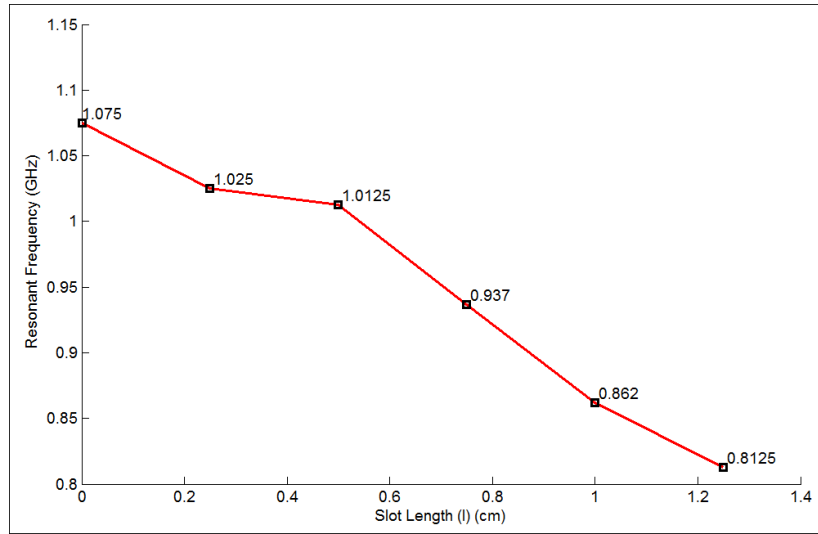


Figure 2.20: Variation of resonant frequency f_r of the antenna with slot length (l)

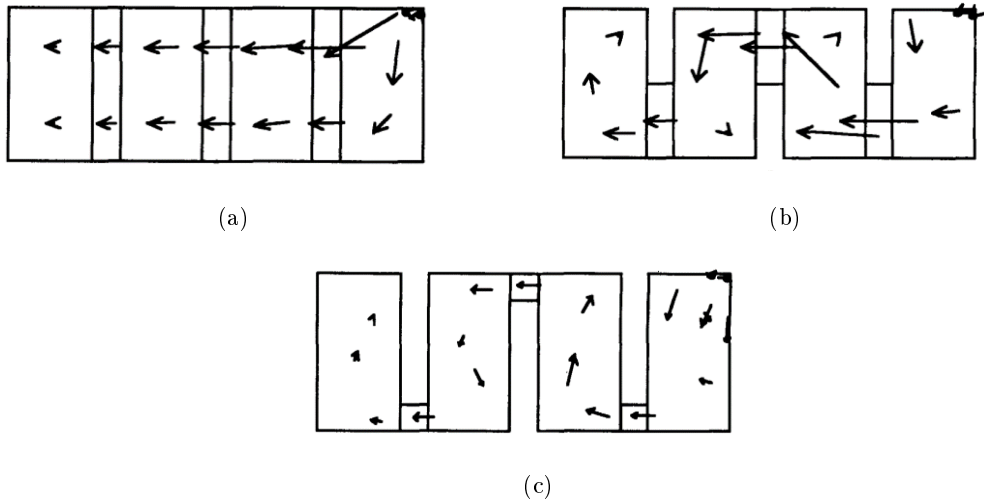


Figure 2.21: Surface current distribution for various slot lengths. (a) $l = 0 \text{ mm}$, (b) $l = 7.5 \text{ mm}$, (c) $l = 12.5 \text{ mm}$ [17].

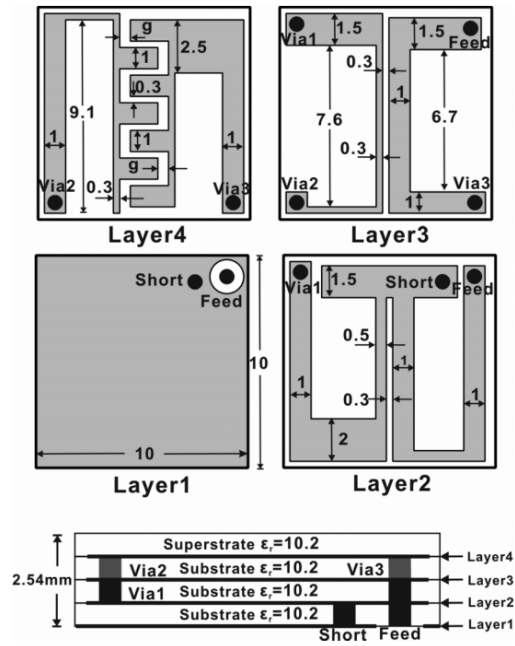


Figure 2.22: The geometry of the 4-layered stacked patch antenna [18].

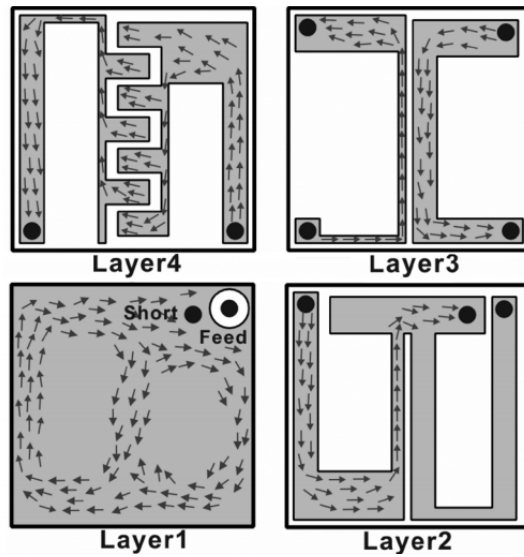


Figure 2.23: Current distribution on the antenna layers at 402 MHz [18].

2.3.3 First Prototype: MICS Band Implantable Antenna Design

After the investigation of the miniaturization techniques, it is decided to design an implantable antenna which operates in MICS band.

2.3.3.1 Antenna Design

At first, the antenna operation is examined in air. Antenna design shown in Figure 2.3 with dimensions of $W = 15.75$ cm, $L = 11.55$ cm, $x_f = 3.125$ cm and $y_f = 7.875$ cm is taken as the initial model. High permittivity substrate RO3210 ($\epsilon_r = 10.2$, $\tan\delta = 0.003$, $h = 1.27$ mm) is preferred for miniaturization. The simulated electric field distribution at 403 MHz for the patch antenna in air is illustrated in Figure 2.24. According to electric field distribution, shorting pins are inserted to the patch antenna. The quarter wave rectangular microstrip antenna ($W = 15.75$ cm, $L = 5.825$ cm, $x_f = 3.825$ cm and $y_f = 7.875$ cm) with simulated electric field at 403 MHz and $|S_{11}|$ for the patch antenna in air are illustrated in Figure 2.25. The maximum simulated gain of the antenna is found as -0.24 dBi. The gain is decreased when compared with the gain of half wavelength antenna (1.95 dBi). Note that, the patch antenna still has the 30 cm \times 30 cm substrate. To obtain a compact size, the substrate and the ground plane size are decreased to 16 cm \times 7 cm. Antenna model, the simulated far field pattern and return loss are shown in Figure 2.26. As expected, the resonant frequency is slightly changed since the ground plane became smaller and needs to be re-tuned. The maximum gain of the antenna is decreased to nearly -7 dBi due to the decrease in directivity when ground plane becomes smaller. Next, the antenna is inserted into 2/3 muscle block whose dimensions are given in Figure 2.7. The return loss and the input impedance of the antenna are presented in Figure 2.27. The real part of the input impedance is observed to be very low. Therefore, the patch length must be longer to achieve higher impedance values.

After the investigation of the classical patch and quarter-wave antenna models for MICS band operation, it is decided to design an antenna which fits in medical

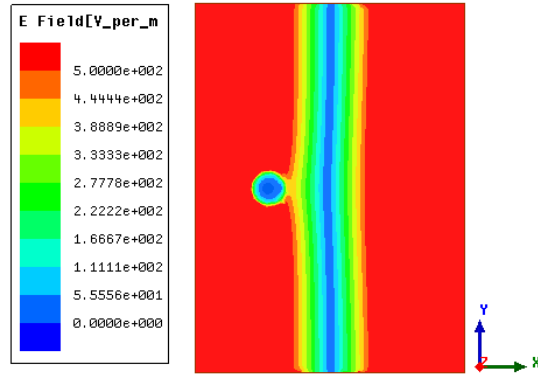
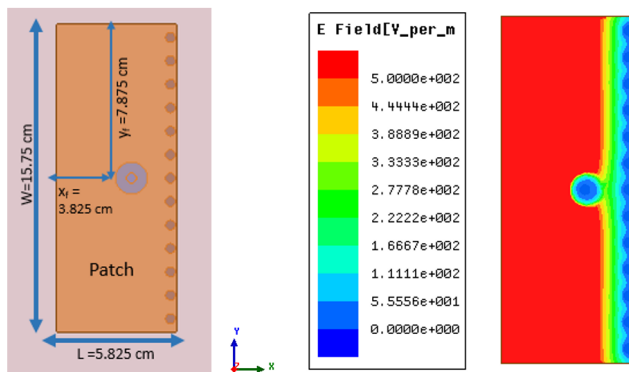
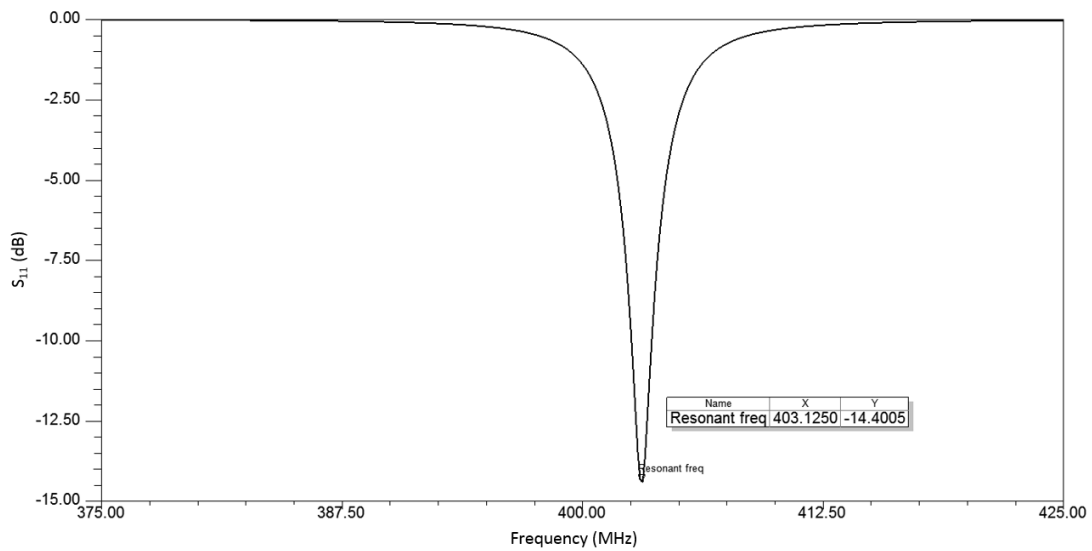


Figure 2.24: Simulated electric field of patch antenna at 403 MHz which radiates into air



(a)



(b)

Figure 2.25: HFSS model of the quarter wave antenna (a) Quarter wave patch antenna model in air with shorting pins and simulated electric field at 402 MHz (b) Return loss of the quarter wave rectangular microstrip antenna

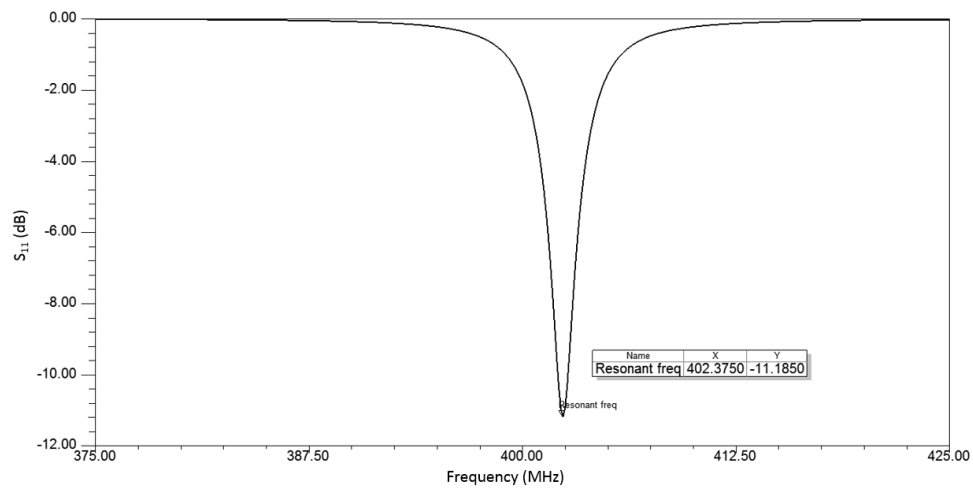
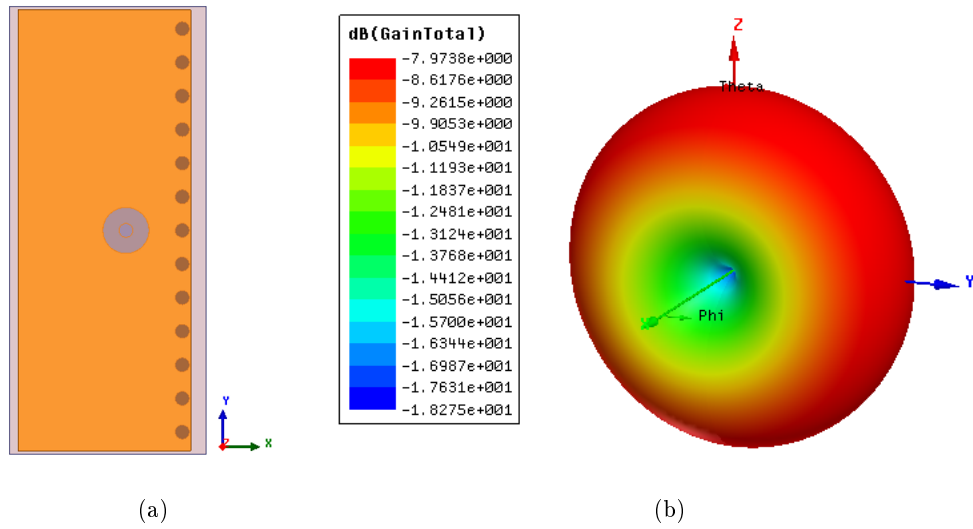
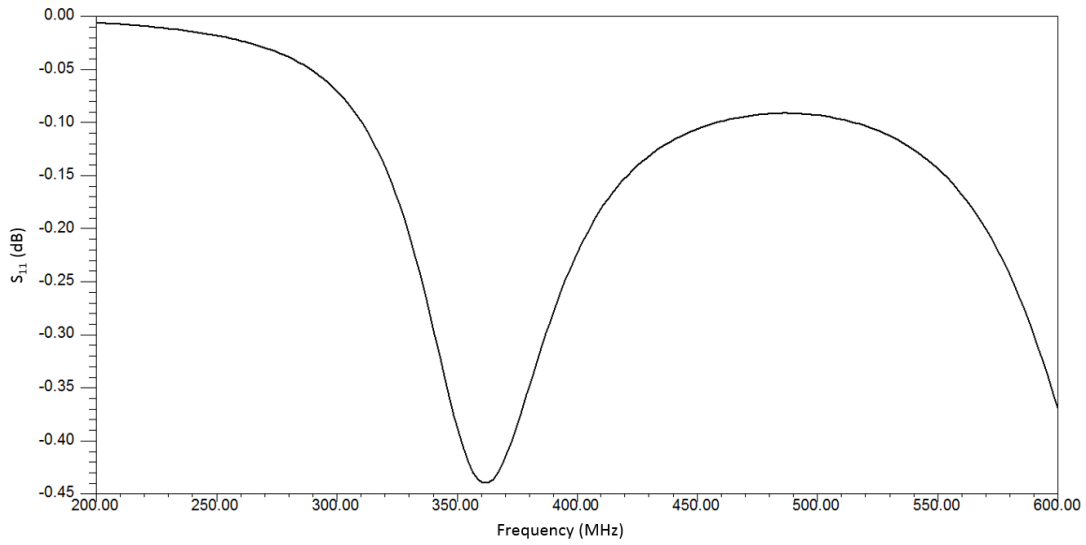
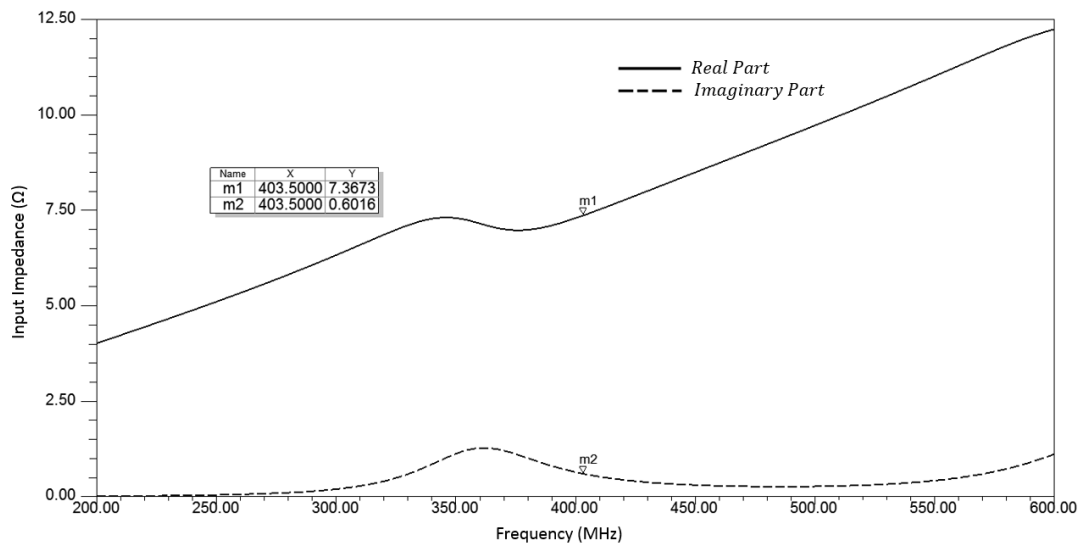


Figure 2.26: HFSS model of the $16\text{cm} \times 7\text{cm}$ quarter wave antenna (a) Top view of the quarter wave patch antenna model in air with shorting pins (b) Simulated far field gain pattern (c) Return loss



(a)



(b)

Figure 2.27: Simulated results for $16\text{ cm} \times 7\text{ cm}$ quarter wave antenna in $2/3$ muscle block tissue (a) Return loss (b) Input impedance

device. Therefore, the miniaturization techniques are applied. First of all, the size of the patch antenna is fixed. It is aimed to fit in a area of $3.1 \text{ cm} \times 1.1 \text{ cm}$. The thickness of the substrate is determined according to the availability in our laboratory. Therefore, R03210 model substrate with 1.27 mm thickness is preferred as substrate. Antenna is fed by a 50 ohm coaxial cable. As tissue model generic dispersive skin model is used [2] for more realistic results. The dielectric properties of the skin are fully frequency-dependent, and the values of permittivity and conductivity are set according to [19] in this study. The electrical properties of skin tissue at 402 MHz were found to be $\epsilon_r = 46.741$, $\sigma = 0.68892 \text{ S/m}$. The tissue model and the antenna used in simulation are illustrated in Figure 2.28. Note that, unless specified, the same tissue model is used through out this thesis study. The feed is inserted into the middle of the patch as shown in Figure 2.29. The centre position of the feed is chosen as half value of the patch's width ($x_f = W/2$). The effect of the feed position in the y direction (l_f) is observed parametrically and the results are shown in Figure 2.30. It is observed that antenna resonates at nearly 1.06 GHz for $l_f = 0.1 \text{ cm}$. To operate in the MICS band, the resonant frequency must be reduced, in other way, the current flow path must be lengthened. To achieve this, the effective length of the antenna is increased by meandering the radiating patch as shown in Figure 2.31. The width of the patch arm ($w = 2 \text{ mm}$) is kept constant for the meandered sections. Note that x_f remained unchanged and the l_f is parametrically changed to find the feed position for the best matching. The simulated fundamental resonant frequency with respect to different feed positions (l_f) for a fully meandered patch is shown in Figure 2.32. It is observed that antenna resonates at 595 MHz for $l_f = 1.5 \text{ cm}$. Further size reduction is needed to operate at 403 MHz. For this aim, shorting pin is inserted between the ground and the patch plane and the antenna become a PIFA type antenna as shown in Figure 2.33. The technique worked similar that a ground plane doubles the height of the monopole antenna [31]. Therefore, the effective length of the antenna increased and the resonant frequency is reduced up to 234 MHz for $l_f = 0.1 \text{ cm}$ as shown in Figure 2.34.

To compensate that effect, the size is shortened iteratively by fixing the shorting

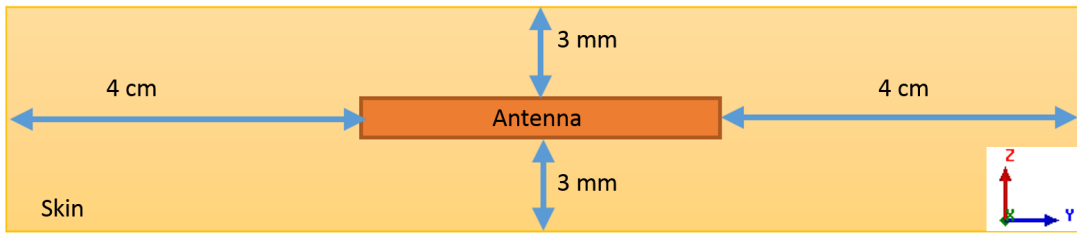


Figure 2.28: Skin model with embedded antenna in HFSS

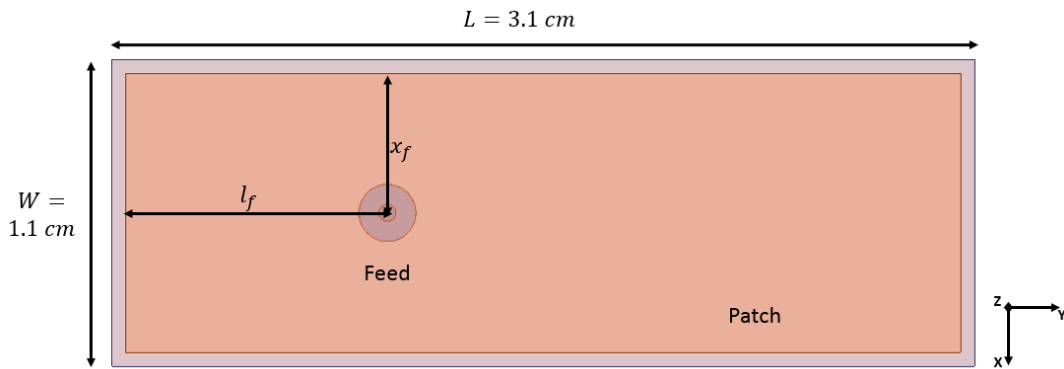


Figure 2.29: 3.1 cm \times 1.1 cm patch model in skin

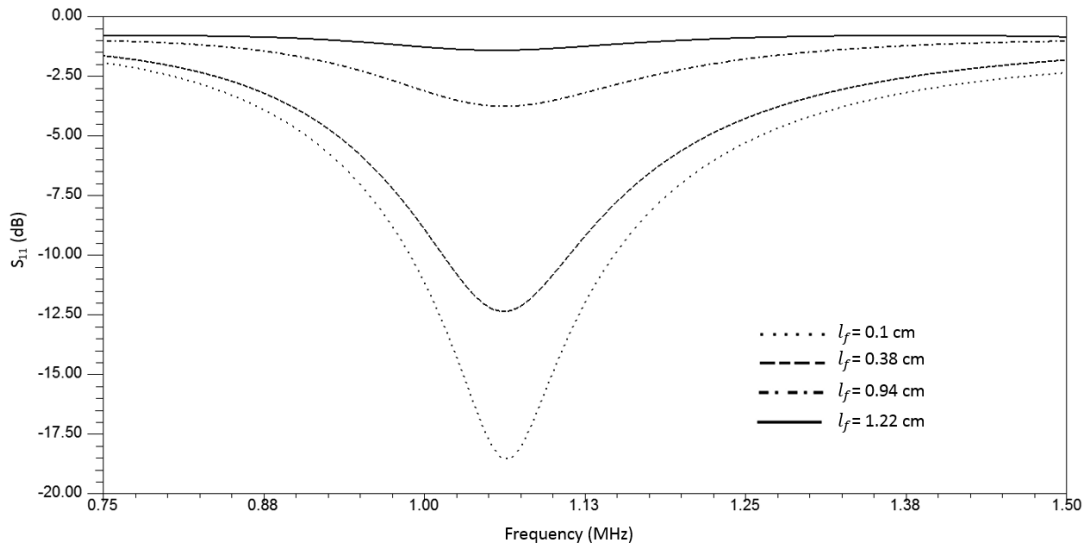


Figure 2.30: Comparison of simulated S_{11} of the antenna for different feed positions- l_f

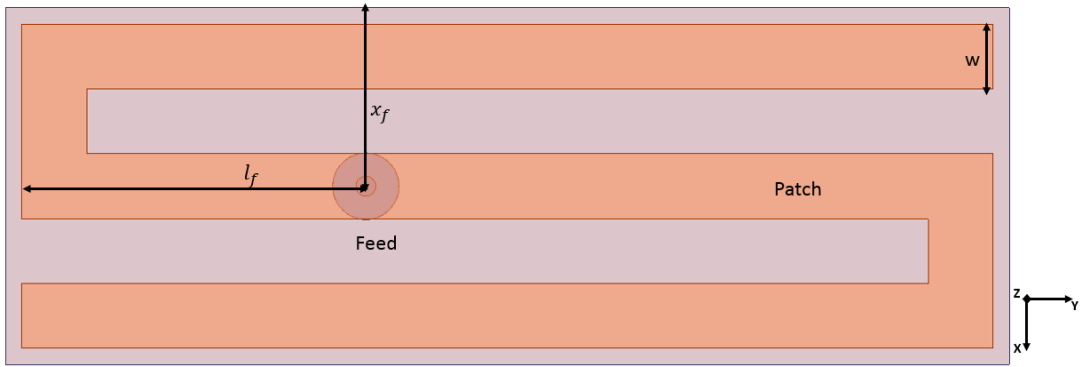


Figure 2.31: $3.1\text{ cm} \times 1.1\text{ cm}$ fully meandered patch model in skin

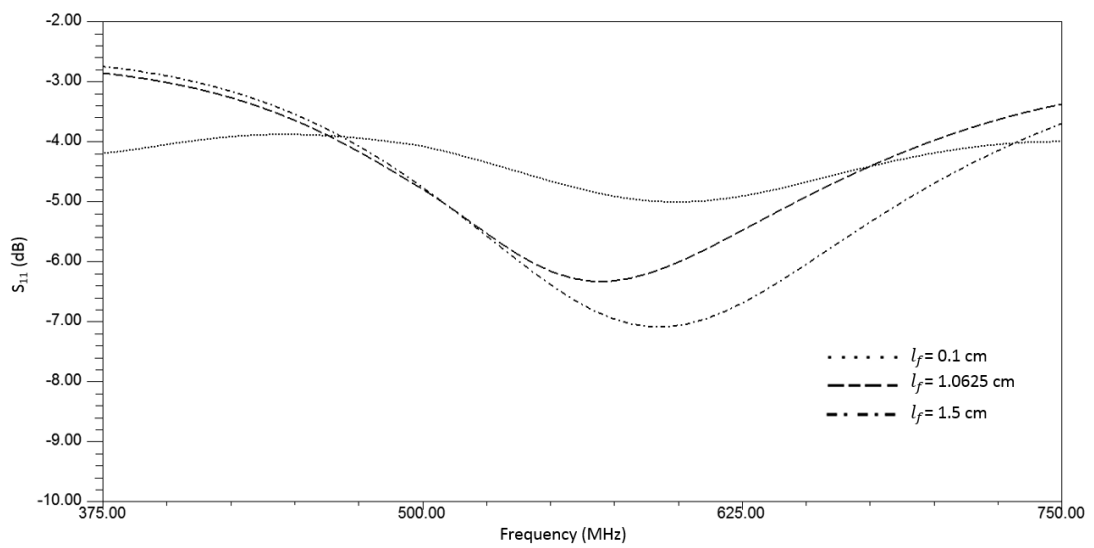


Figure 2.32: Comparison of simulated S_{11} of the fully meandered patch antenna for different feed positions- l_f

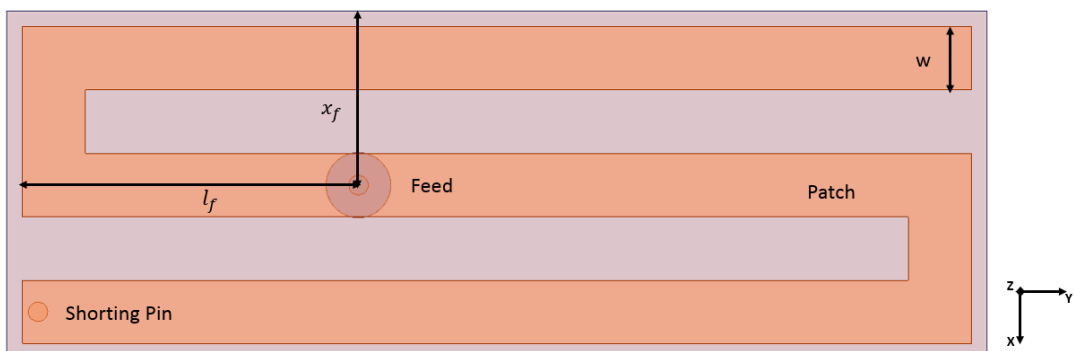


Figure 2.33: $3.1\text{ cm} \times 1.1\text{ cm}$ PIFA model in skin

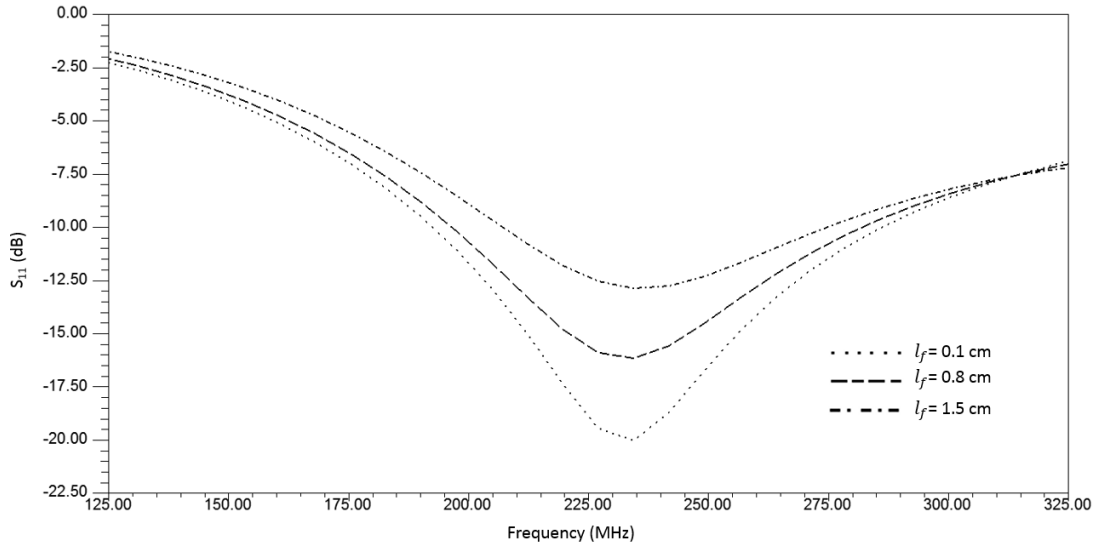
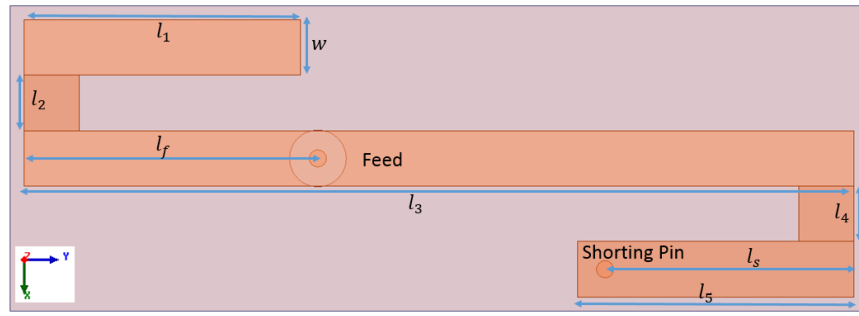


Figure 2.34: Comparison of simulated S_{11} of the PIFA for different feed positions- l_f

pin at the end of the lower arm. The resulting optimized dimensions of the antenna are given in Table 2.4. The geometry of the designed antenna with related parameters is depicted in Figure 2.35. Simulated return loss of the antenna is shown in Figure 2.36. Antenna resonates in the frequency range 343 to 474 MHz at MICS band for S_{11} less than 10 dB. The gain pattern and the maximum simulated gain value (-35.9 dBi) of the antenna are consistent with the gain characteristics of the implantable microstrip antennas and represented in Figure 2.37 [47].

Table2.4: Optimized Dimensions of the Prototype-1

Parameter	Dimesion (mm)
l_1	10
l_2	2
l_3	30
l_4	2
l_5	10
w	2
l_f	10.625
l_s	9



(a)



(b)

Figure 2.35: HFSS model of the first prototype antenna (a) Top view of the antenna with conductor parameters (b) Side view of the antenna

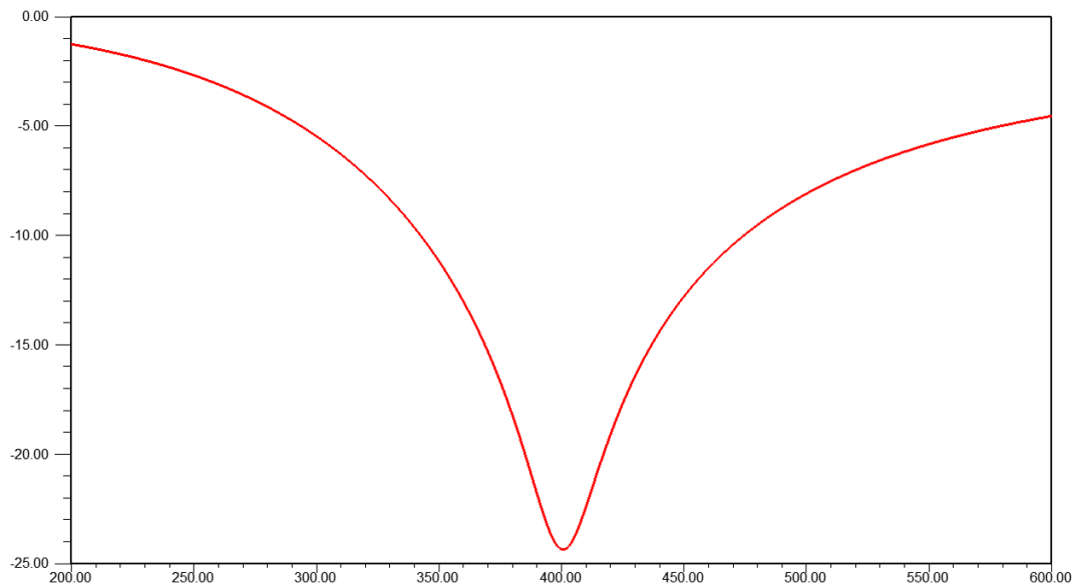


Figure 2.36: Simulated return loss of the Prototype-1

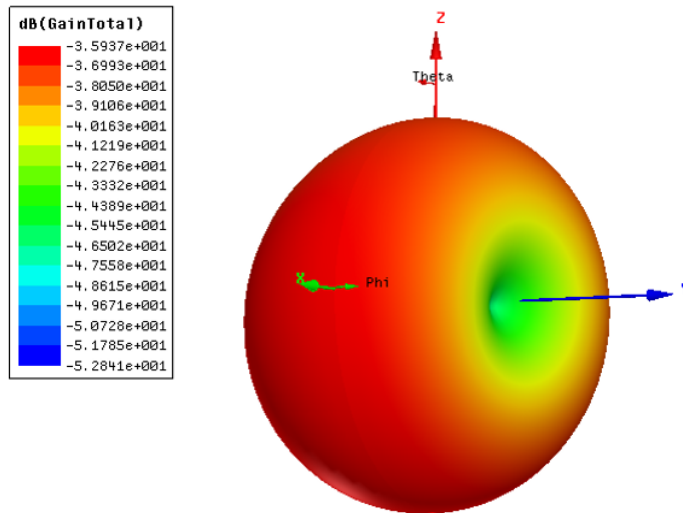


Figure 2.37: Simulated far field gain for the Prototype-1 at 402 MHz

2.3.3.2 Fabrication and Measurement in Air

To confirm the validity of the numerical simulations, experimental investigations are carried out. Fabrication of the antenna is completed using LPKF-ProMat-H100 circuit board plotter. A photograph of the fabricated antenna is shown in Figure 2.38. The fabricated antenna is measured using N9915A FieldFox Analyser. The results in air are illustrated in Figure 2.39. Since antenna radiates into air, frequency shift is occurred as expected.

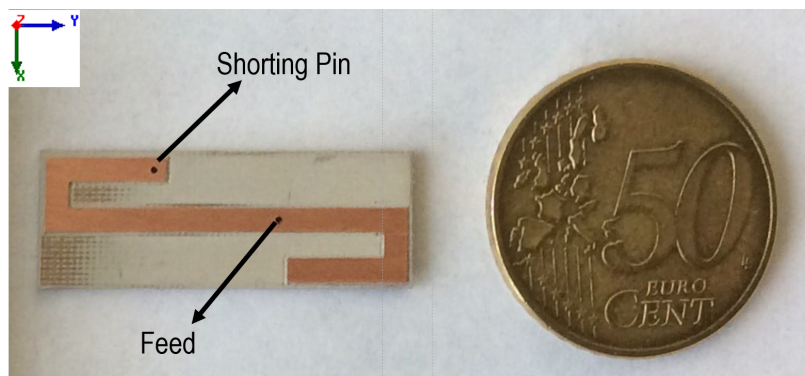


Figure 2.38: Photograph of fabricated implantable antenna

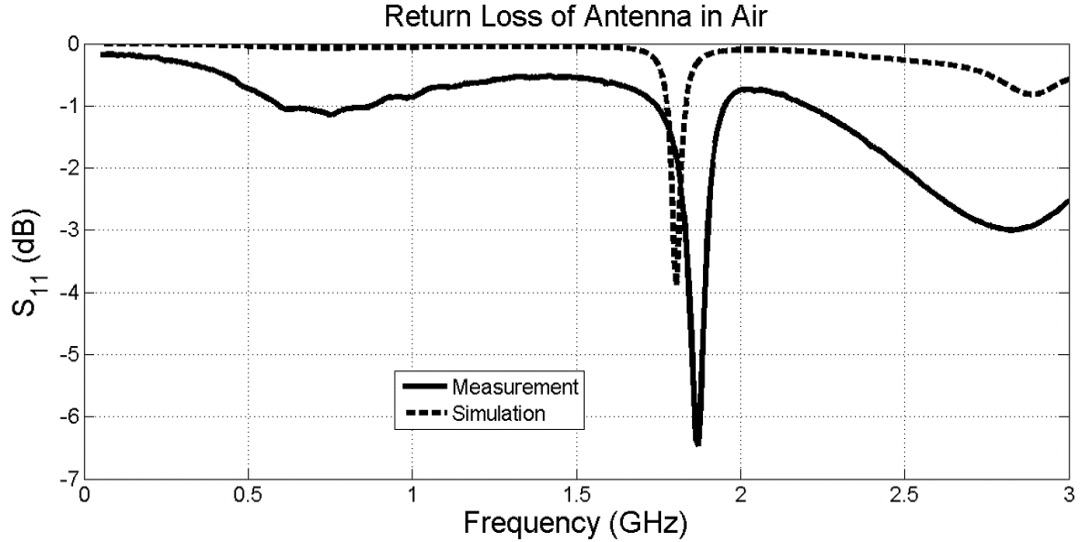


Figure 2.39: Comparison of the measured and simulated S_{11} in air

2.3.3.3 Phantom Preparation in the MICS band and *in vitro* Measurement

To test the antenna *in vitro*, a skin mimicking gel which has the electrical properties of skin at the MICS band is prepared with a recipe as shown in Table 2.5. The recipe is taken from [1]. The ingredients are mixed according to the Figure 2.40 which shows process to characterize proposed skin mimicking gel. Note that agarose is crucial to obtain a gel like material and does not have a significant effect to the electrical properties of the mixture [68]. Agarose is solvable in the water at high temperatures. Therefore, the mixture is heated until 50 Celsius degree where the mixture become transparent. The measurement of the phantom's electrical properties (ϵ_r and σ) are conducted via virtual line method [69]. In Appendix A, the technique is explained in detail. Skin mimicking fluid and antenna measurement setup are shown in Figure 2.41 (a) and (b), respectively. Figures 2.42 and 2.43 show the conductivity and the permittivity of the skin-mimicking gels prepared for the MICS band. The measurements are compared with the reference data taken from [19]. As seen in these figures, electrical properties perfectly match with the reference values for the MICS band. After the

preparation of the phantom, the antenna is placed in a plastic container which has same dimensions as the simulation model. Then the skin-mimicking liquid is poured in the container and it is left to cool down to solidify. Figure 2.44 displays the comparison of measured and simulated S_{11} of the proposed antenna. As seen from the graph, the results agree well at the MICS band. The measured frequencies range from 335 MHz to 474 MHz (34%) at the MICS band for S_{11} less than 10 dB and the maximum simulated gain of the antenna is -36 dBi.

Table2.5: Recipe for skin mimicking gel taken from [1]

MICS Band	
Sugar	% 56.18
NaCl	% 2.33
De-ionizaed Water	% 41.49
Agarose	Add 1 g in 100 ml solution

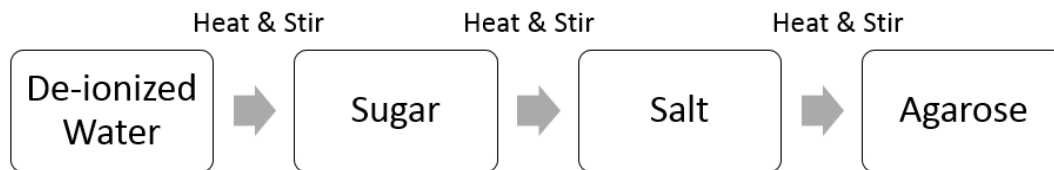
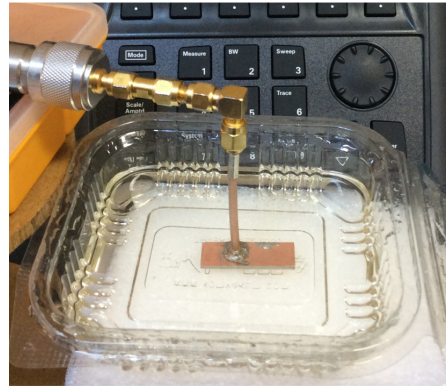


Figure 2.40: Process of preparing skin mimicking gel for MICS band



(a)



(b)

Figure 2.41: (a) Skin mimicking fluid (b) Antenna measurement in skin mimicking fluid

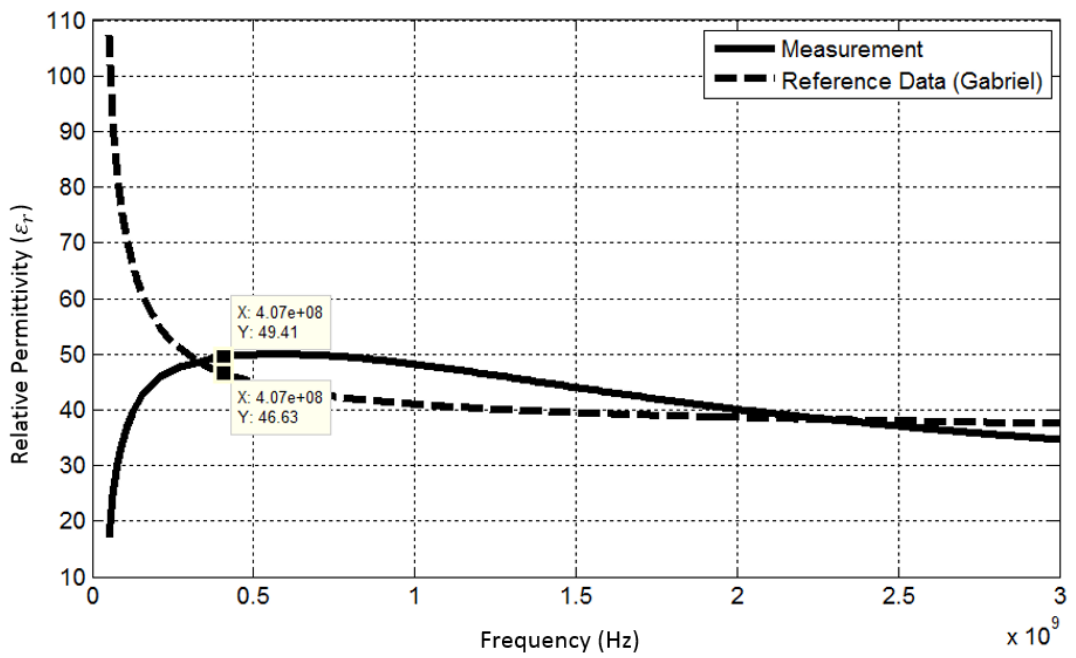


Figure 2.42: Comparison of permittivity of the MICS band skin-mimicking gels with the reference data from [19].

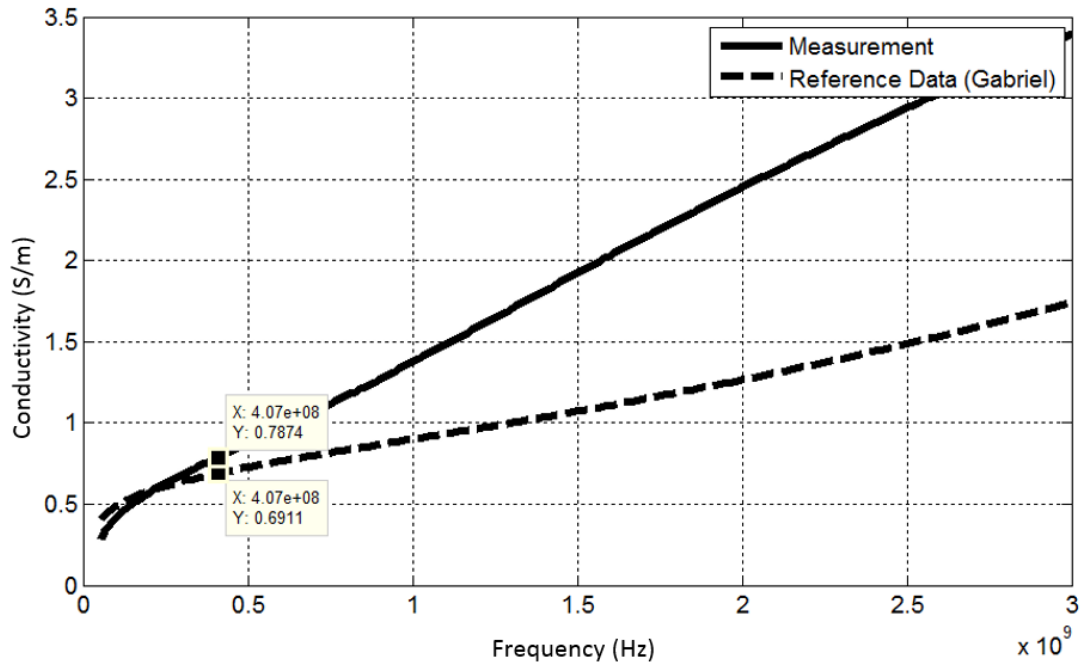


Figure 2.43: Comparison of conductivity of the MICS band skin-mimicking gels with the reference data from [19].

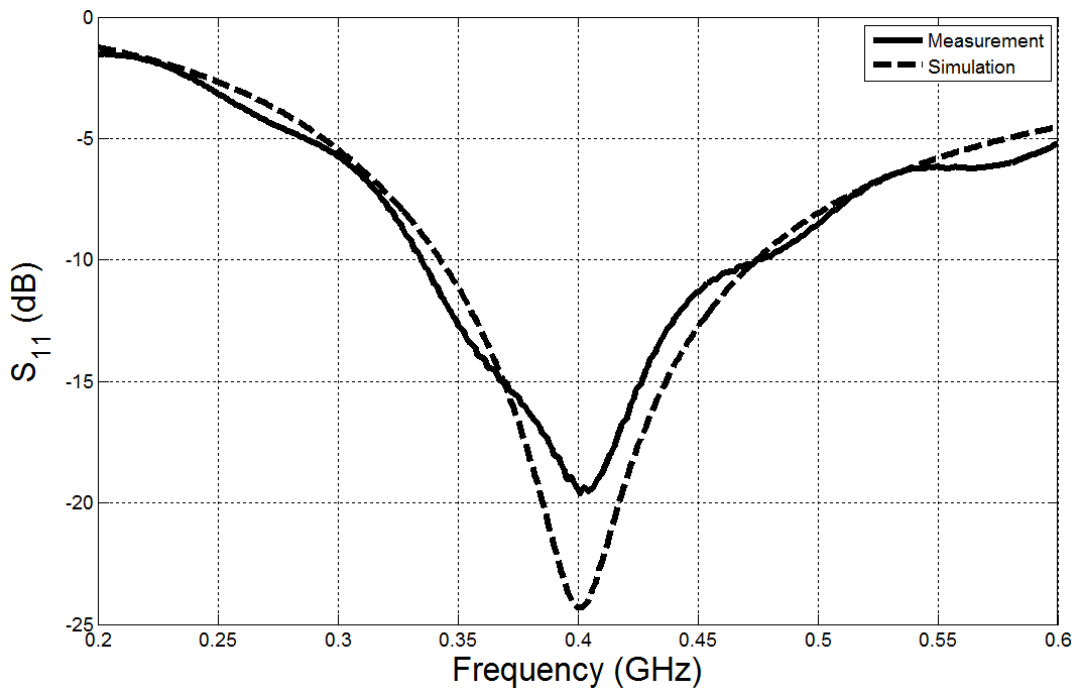


Figure 2.44: Comparison of the measured and simulated S_{11} in skin mimicking gel

CHAPTER 3

DESIGN OF MINIATURIZED IMPLANTABLE PIFA IN DUAL BAND

3.1 Introduction

After the design of the first prototype (See Section 2.3.3) which operates in MICS band, it is decided to design an implantable antenna which has dimensions of $2\text{ cm} \times 1\text{ cm}$ in xy-plane and operates in both MICS and ISM bands. To achieve this aim, miniaturization techniques explained in the previous chapter are utilized. Design procedure is explained step by step.

First of all, without considering the size restriction and dual band operation, patch stacking and use of superstrate are examined. The multilayered microstrip antenna structure consists of a superstrate layer over the substrate. In applications of microstrip antenna in aircraft, spacecraft, missiles and those structures where it needs protection against environment, use of superstrate layer is desirable [61]. When medical applications are assumed, superstrate dielectric layer is used so that the metallic radiator does not directly come in contact with the surrounding biological tissues. Therefore, a superstrate layer facilitates implanted antenna design by providing stable impedance matching performance of implanted antennas and lowers absorbed power inside human body [4]. Moreover, adding a superstrate of high relative permittivity is a standard technique that generally improves the bandwidth and gain efficiency of the antenna. The loading of the superstrate reduces the resonant frequency, decreases the resonant resistance, and enhances the impedance bandwidth of the antenna. The larger

the relative permittivity of the superstrate is, the more the resonant frequency decreases as the superstrate becomes thicker [2].

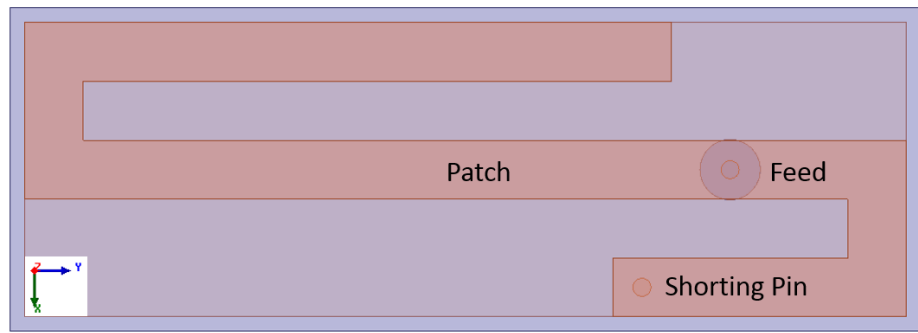
3.2 Antenna Design Steps

Design 1

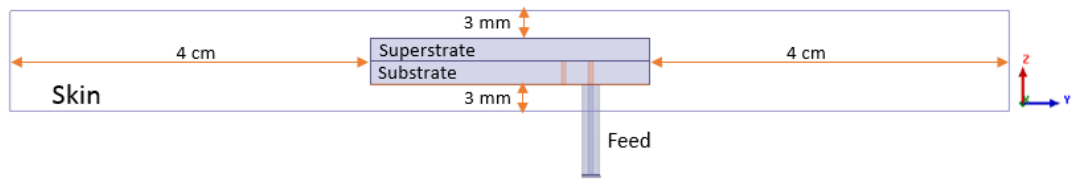
In the first design, the antenna is loaded with a RO3210 superstrate with a thickness of 1.27 *mm*. Since the superstrate layer insulates the antenna from the higher permittivity tissue, the effective permittivity is decreased. This results in an increase in the effective length of the antenna and reduction in the resonant frequency. To compensate it, the length of the radiating metal is increased. Because of the increase in the radiating area, the gain of the antenna is also increased, as expected. The resultant antenna geometry, return loss of the antenna and the simulated three dimensional far field gain are shown in Figure 3.1, Figure 3.2, and Figure 3.3; respectively. The simulated frequencies range from 384 MHz to 420 MHz at the MICS band for S_{11} less than 10 dB and the maximum simulated gain of the antenna is -32.6 dBi.

Design 2

In the second design, the antenna is stacked by carrying the patch's upper arm onto the second substrate. The height of the feed's inner conductor is increased to excite both the upper and the lower arms of the patch. Since the effective length of the antenna increases, length of the radiating metal is also increased to reduce the resonant frequency. With the introduction of the second substrate, the total thickness of the antenna is increased. The resultant antenna geometry, return loss of the antenna and the simulated three dimensional far field gain are shown in Figure 3.4, Figure 3.5, and Figure 3.6; respectively. The simulated frequencies range from 383 MHz to 442 MHz at the MICS band for S_{11} less than -10 dB and the maximum simulated gain of the antenna is -32 dBi.



(a)



(b)

Figure 3.1: Design 1 (a) Top view of the antenna in xy-plane (b) Side view of the antenna in yz-plane

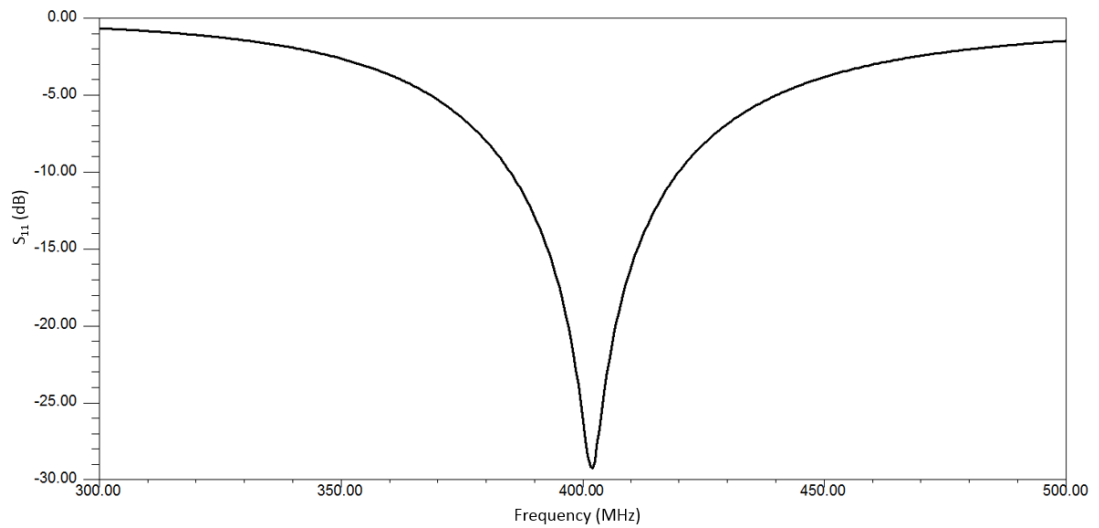


Figure 3.2: Simulated S_{11} of the antenna - Design 1

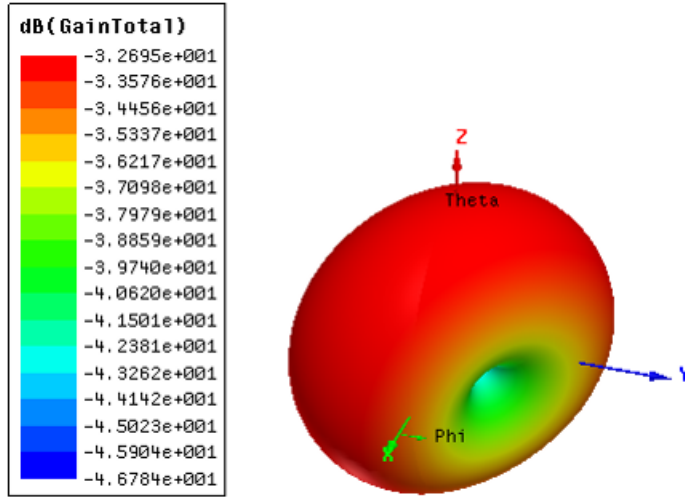
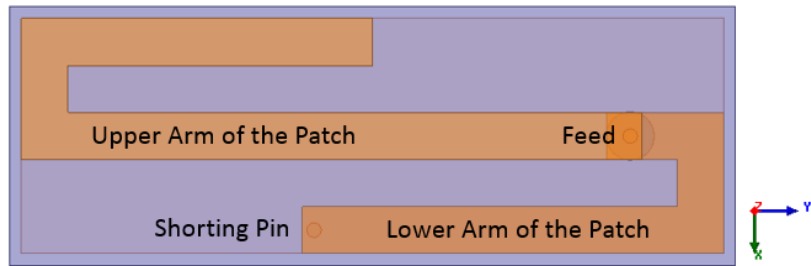


Figure 3.3: Simulated three dimensional gain pattern of the antenna - Design 1

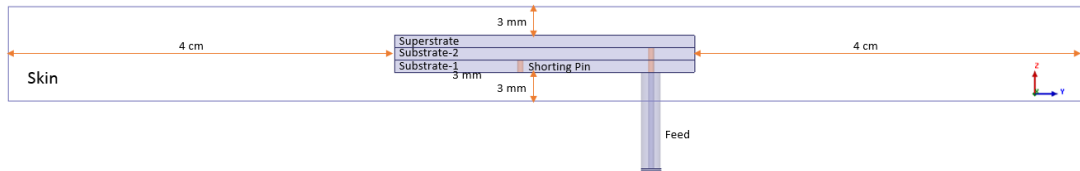
Design 3

In the third design, there are two goals to be achieved: 1) to increase the gain of the antenna and 2) to operate in dual band (MICS and ISM). To operate in dual band, the feed position and the connection point of the arms are parametrically changed and the change in resonant frequency is observed. It is highly recommended to carry out simulations for implantable antennas while considering the actual dimensions and material properties of the commercial coaxial cable to be used in the fabrication [24]. Therefore, the feed is modelled according to the commercially available Huber Suhner Sucoform-141 coaxial cable. The geometry of the antenna with design parameters for each rectangle part is illustrated in Figure 3.7. The effect of the feed point on the resonant frequency is shown in Figure 3.8. It is observed that the location of the feed point impact both the matching of the antenna and the dual band characteristics. The feed location is chosen as $l_f = 2.82 \text{ cm}$ since that gives the best matching for MICS and ISM bands.

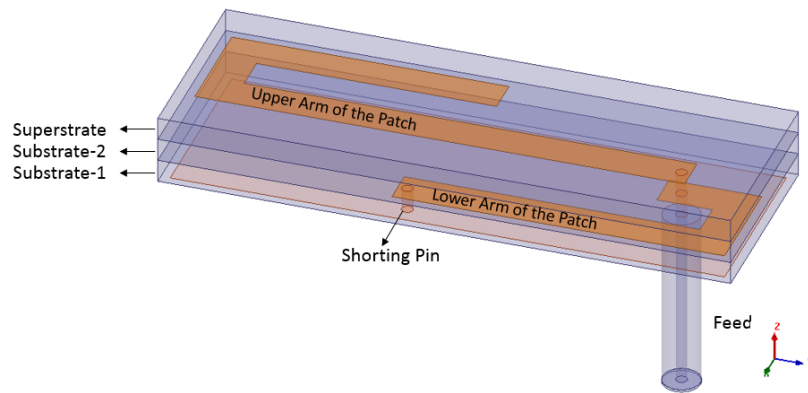
Although there is a frequency shift for the ISM band, the resonant frequency can be tuned. The real and imaginary parts of input impedances for the MICS and ISM bands are presented in Figure 3.9. Imaginary part of the input impedance



(a)



(b)



(c)

Figure 3.4: Design 2 (a) Top view of the antenna in xy-plane (b) Side view of the antenna in yz-plane (c) Trimetric view of the antenna

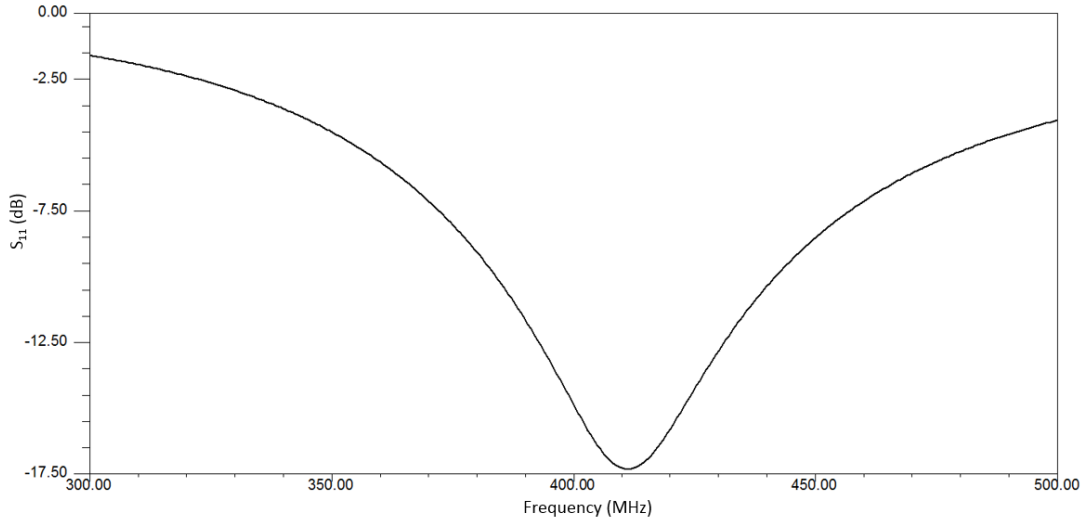


Figure 3.5: Simulated S_{11} of the antenna - Design 2

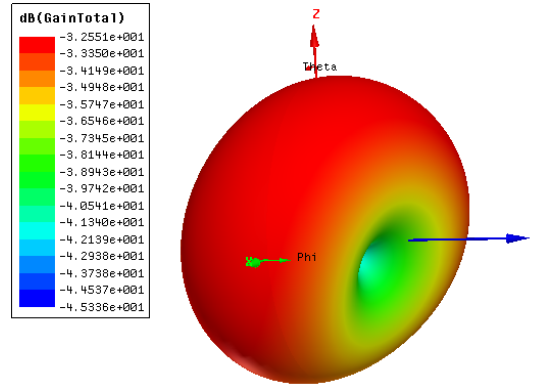


Figure 3.6: Simulated three dimensional gain pattern of the antenna - Design-2

for 2.45 GHz is inductive; to reduce it, firstly, the current density distribution on the patch surface is observed at 403.5 MHz and 2.45 GHz. As shown in Figure, *Rect1*, *Rect2* and *Rect5* does not affect the MICS band. Therefore, changing the dimensions of those rectangles helps to tune antenna for the ISM band operation without disturbing the MICS band operation. First of all, w_2 and w_5 are changed from 0.2 cm to 0.1 cm to reduce the inductive part of the input impedance at the ISM band. The return loss and the input impedance of the antennas are shown in Figure 3.11 and Figure 3.12, respectively. It is observed that the imaginary part of the antenna is reduced from 63Ω to 21Ω for ISM band and -3Ω to -11Ω for the MICS band. As expected, the MICS

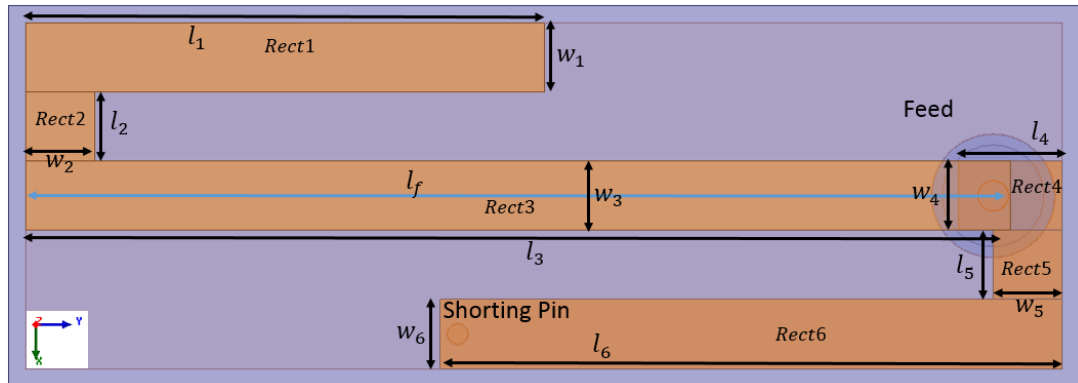


Figure 3.7: Top view of the antenna with design parameters - Design 3

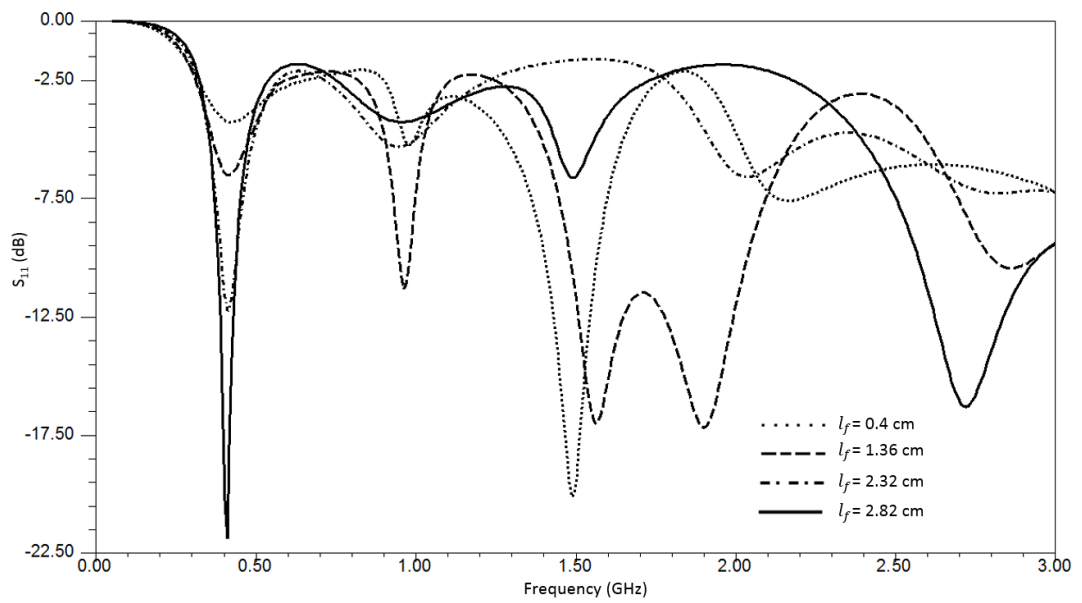


Figure 3.8: Effect of feed point location on the resonant frequency

band is affected slightly. The antenna operates in higher frequency for the ISM band. To reduce the resonance frequency of the antenna the length of the *Rect6* (l_6) is changed slightly from 1.8 cm to 2 cm . Moreover, the shorting pin position is changed to the end tip of (l_6). According to simulation results, S_{11} of the antenna for 2.45 GHz is nearly -15 dB . However, the MICS band is also affected and the resonant frequency is decreased. To tune this affect, the width of the *Rect1* (w_1) is changed from 0.2 cm to 0.1 cm . Figure 3.14 represents the final geometry of the designed antenna. The related parameters and their values are given Table 3.1. The simulated S_{11} of the antenna is represented in Figure 3.15. As aimed, antenna operates in dual band (MICS and ISM). The maximum simulated gain of the antenna for the MICS and ISM bands are found as -30 dBi and -7 dBi , respectively. Gain values are enough to communicate for an external device according to link budget.

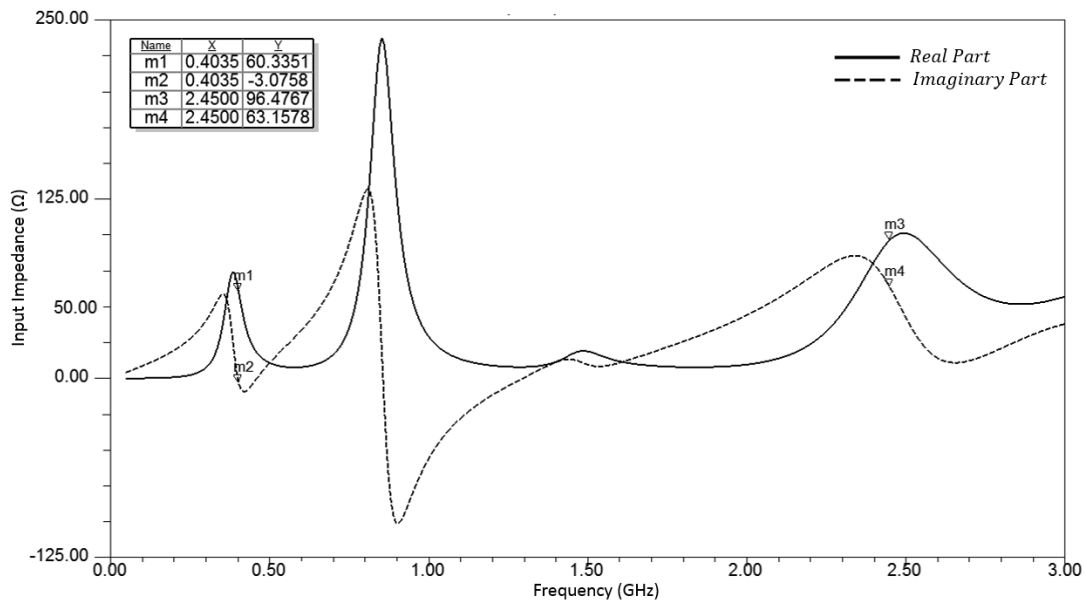
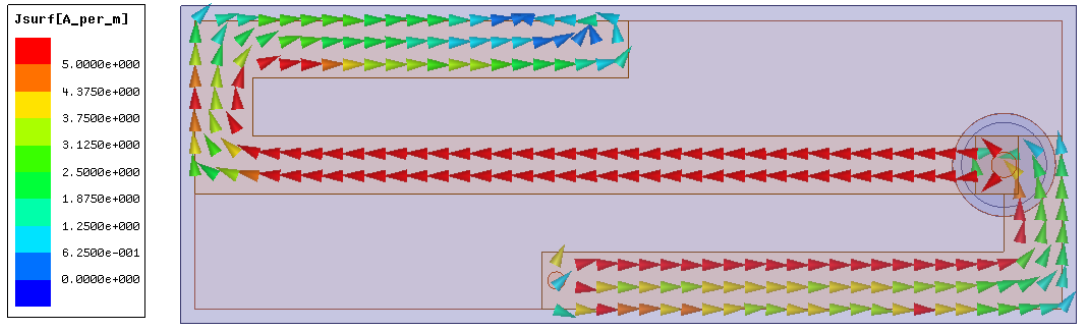
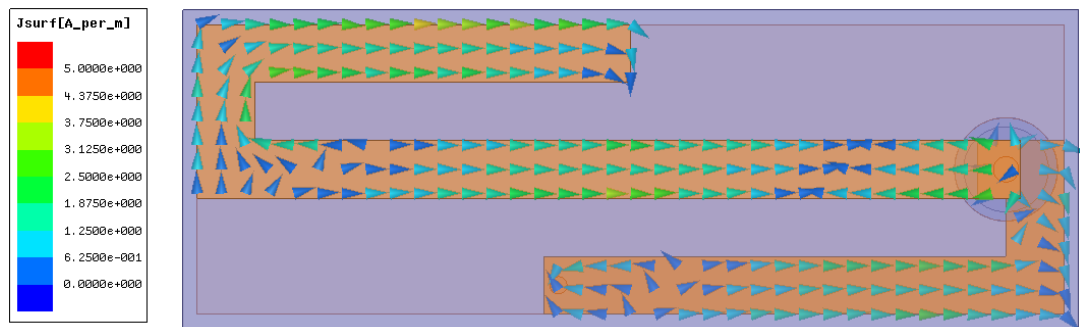


Figure 3.9: Input impedance of the antenna for $l_f = 2.82\text{ cm}$



(a)



(b)

Figure 3.10: Current density vector distribution on the patch surface (a) 403.5 MHz (b) 2.45 GHz

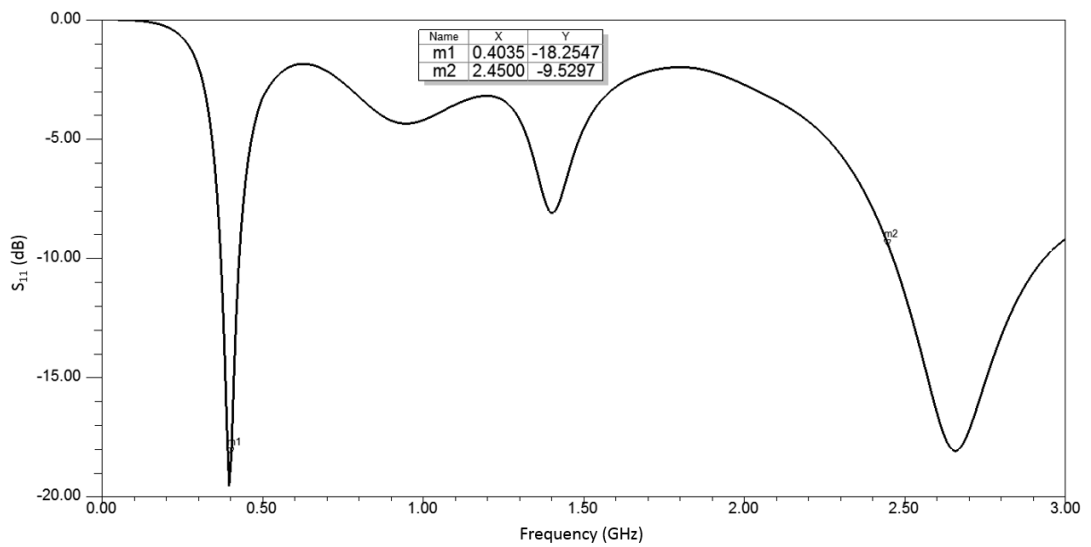


Figure 3.11: Simulated S_{11} of the antenna for $w_2 = w_5 = 0.1 \text{ cm}$

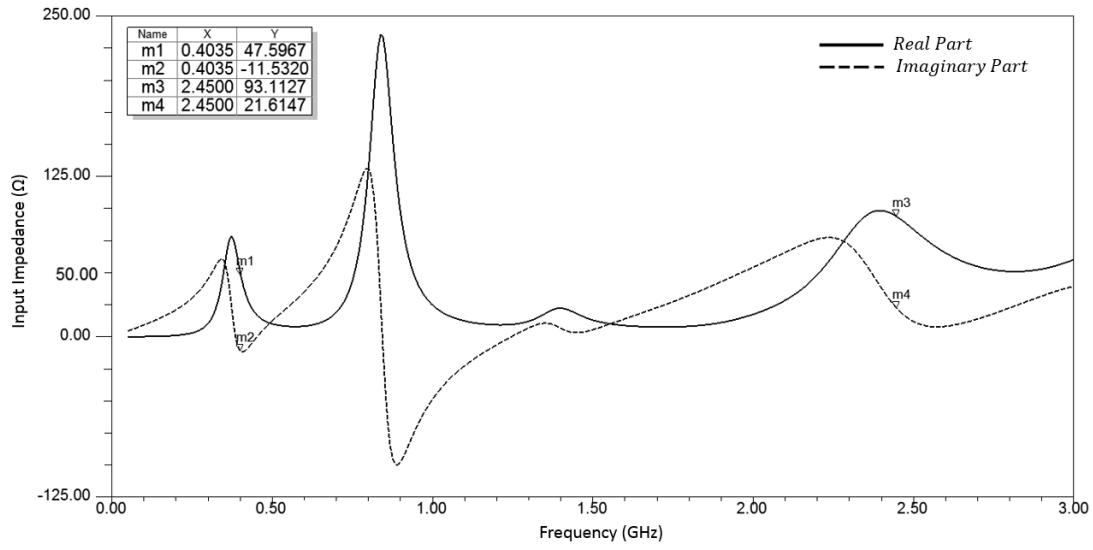
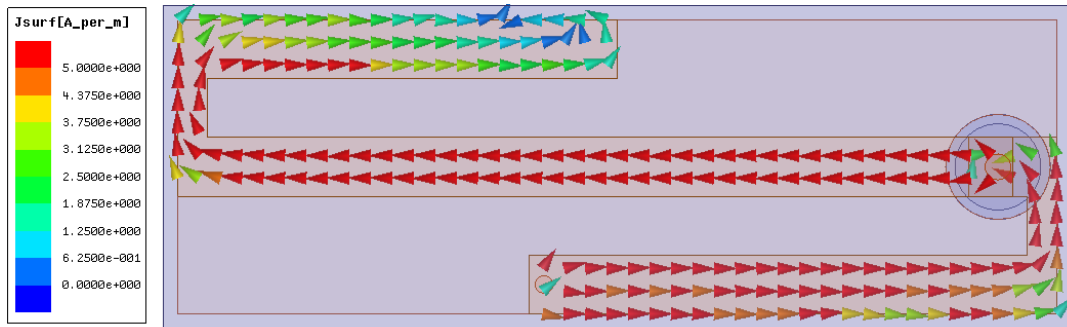
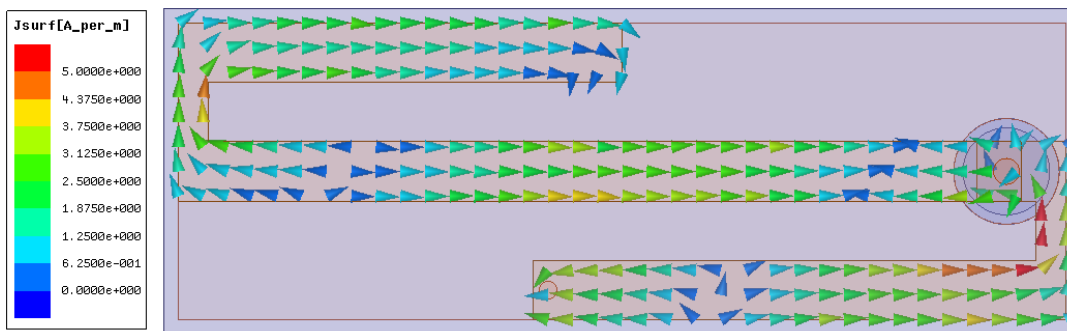


Figure 3.12: Input impedance of the antenna for $w_2 = w_5 = 0.1 \text{ cm}$



(a)



(b)

Figure 3.13: Current vector distribution on the patch surface for $w_2 = w_5 = 1 \text{ cm}$
 (a) 403.5 MHz (b) 2.45 GHz

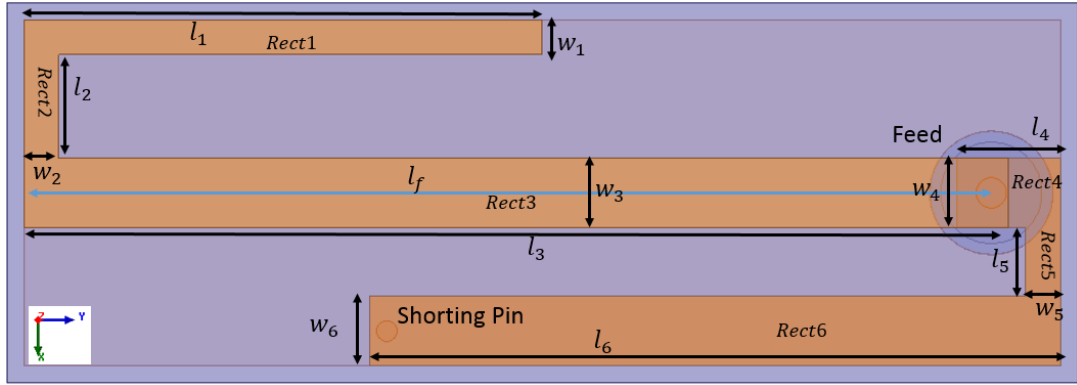


Figure 3.14: Top view of the antenna dual band (MICS and ISM band) tuned antenna - Design 3

Table3.1: Optimized Dimensions of the Design-3 given in Figure 3.14

Parameter	Dimesion (cm)	Parameter	Dimesion (cm)
l_1	1.54	w_1	0.1
l_2	0.3	w_2	0.1
l_3	2.85	w_3	0.2
l_4	0.3	w_4	0.2
l_5	0.2	w_5	0.1
l_6	2	w_6	0.2
l_f	2.82		

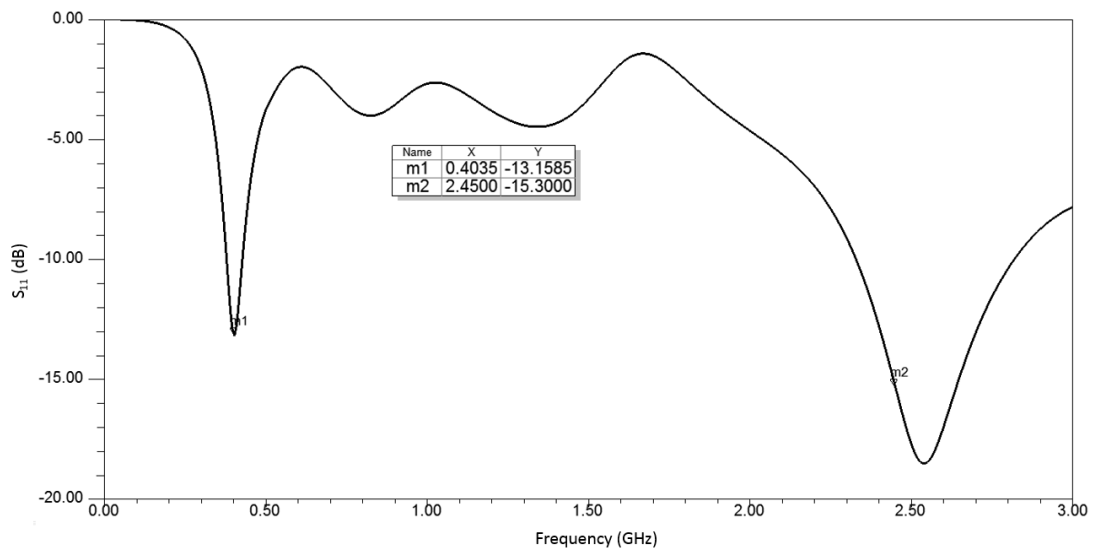


Figure 3.15: Simulated S_{11} of the dual band tuned antenna

Final Design

In the previous design, the antenna is tuned to operate in dual band and has the sufficient gain value for the wireless communication. However, it still has large dimensions ($3\text{ cm} \times 1\text{ cm}$) in the xy-plane. In the final design, the antenna is fitted into the volume of $2\text{ cm} \times 1\text{ cm} \times 3.81\text{ mm}$. The intuition obtained from the previous designs is used to tune the antenna. For each design step, the current vector density distribution on the patch surface and input impedances at the MICS and ISM bands are observed. Firstly, tuning is done manually by changing antenna parameters. After the initial design of the antenna which operates close to the MICS and ISM bands, HFSS optimization tool is utilized. Each step is briefly discussed below:

Step 1

In the first step, antenna designed in *Design-3* is modified to fit in a area of $2\text{ cm} \times 1\text{ cm}$. Resulting antenna geometry is depicted in Figure 3.16. The width parameters are kept constant while the length of the parameters l_3 and l_6 are decreased. The simulated S_{11} and the input impedance of the antenna are presented in Figure 3.17 and Figure 3.18, respectively. It is observed that there exists a frequency shift for both MICS and ISM bands, as expected. Current density vectors on the patch surface are observed and shown in Figure 3.19 to understand the resonant behaviour of the antenna. For MICS band, the resonant frequency is shifted upward. This occurs due to that the patch arms carrying opposing current vectors are closer each other than the one in Design-3. On the other hand, for the ISM band, the resonant frequency is shifted downwards since the patch arms carrying current vectors in the same direction are closer to each other.

Step 2

In the second step, the width parameters w_3 and w_6 are changed to reduce the imaginary part of the input impedance. w_3 is preferred to reduce the inductive

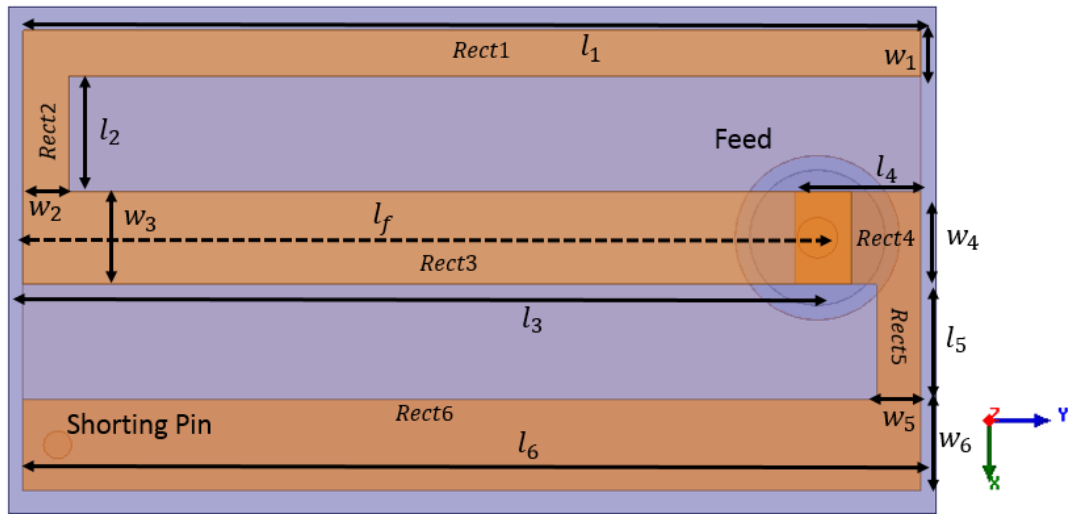


Figure 3.16: Top view of the antenna in Step-1 which fits in an area of $2\text{ cm} \times 1\text{ cm}$

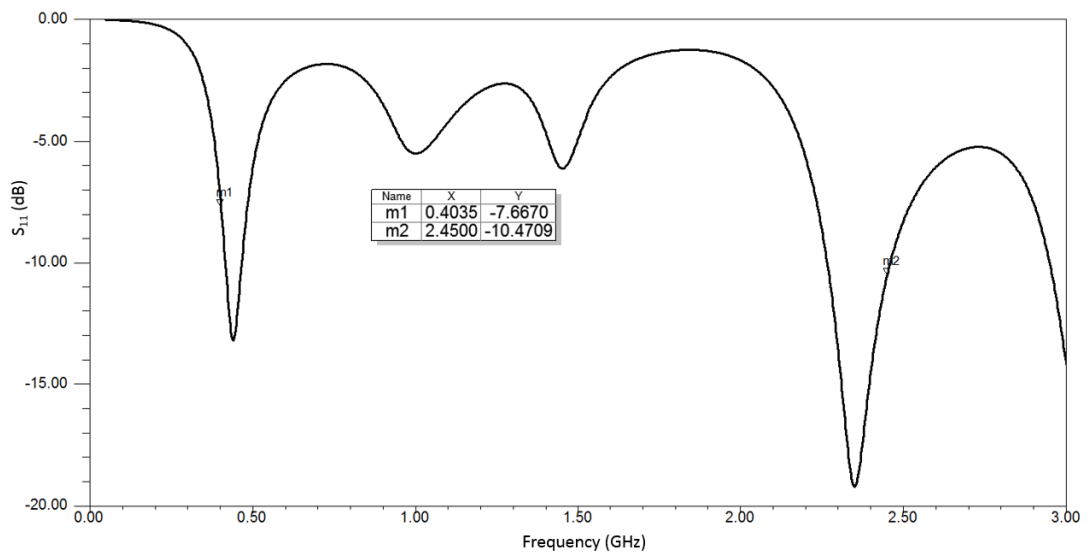


Figure 3.17: Simulated S_{11} of the antenna in Step-1

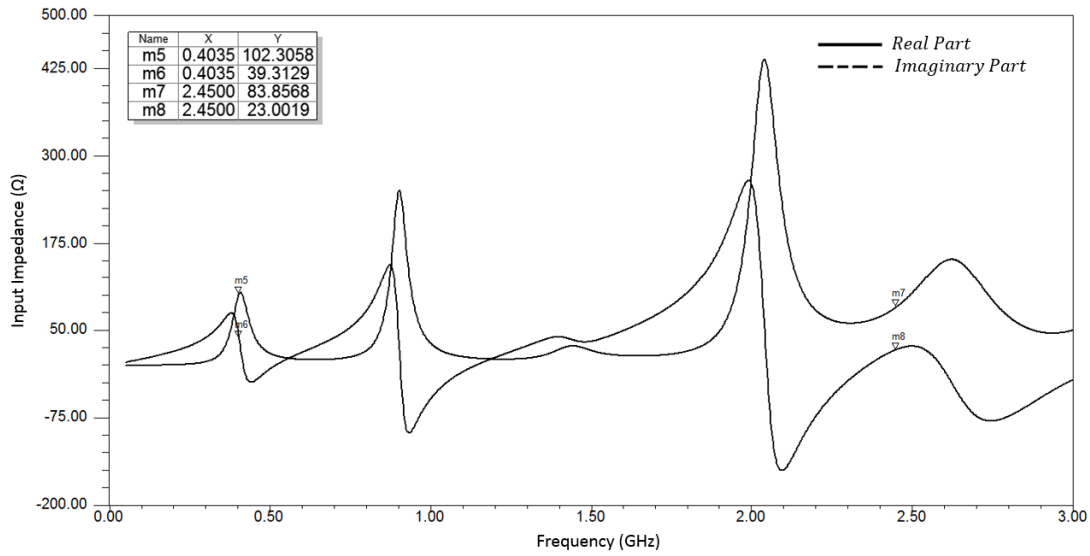
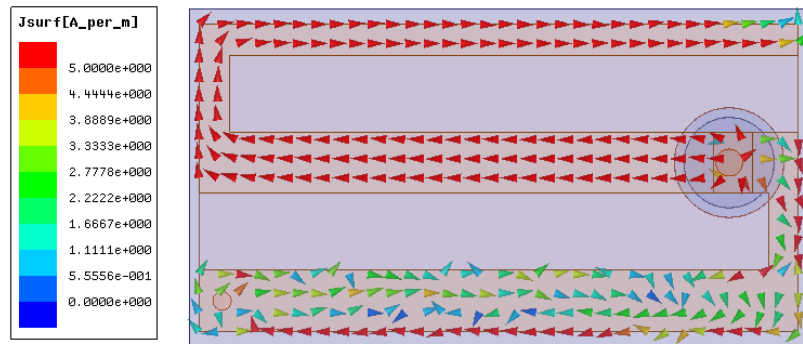
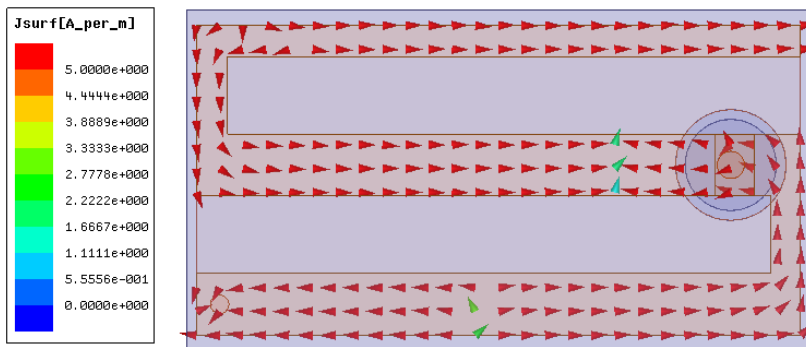


Figure 3.18: Simulated Z_{in} of the antenna in Step-1



(a)



(b)

Figure 3.19: Current density vector distribution on the patch surface of the antenna in Step-1 (a) 403.5 MHz (b) 2.45 GHz

effect for both the MICS and ISM bands, and, w_6 is preferred due to the disturbed current density distribution behaviour at the MICS band as shown in Figure 3.19-(a). The resultant geometry of the antenna is depicted in Figure 3.20. The simulated S_{11} of the antenna is presented in Figure 3.21. According to simulation results, S_{11} of the antenna for 403.5 MHz and 2.45 GHz is nearly -10 dB and -11 dB, respectively.

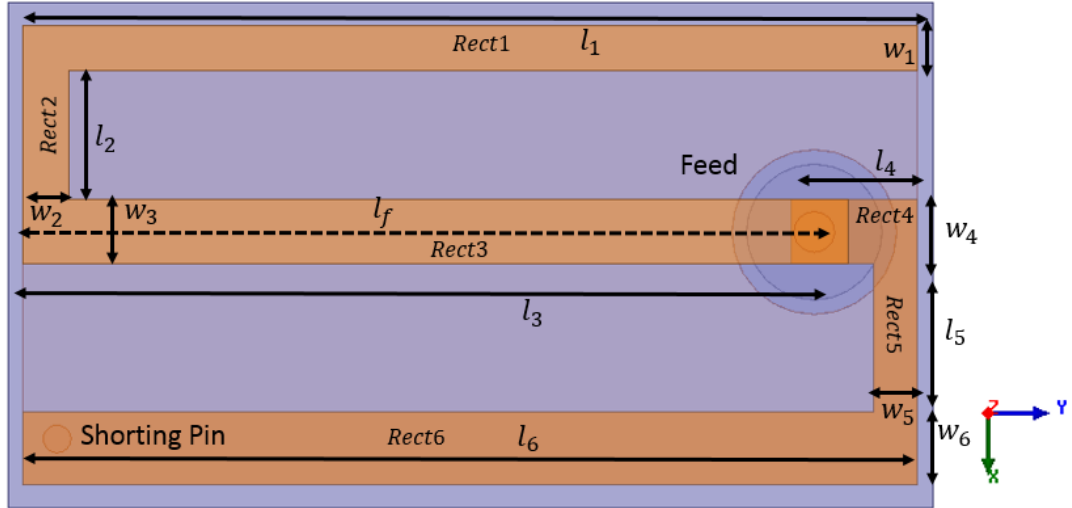


Figure 3.20: Top view of the antenna in Step-2

Step 3

In this step, both parametric and optimetric analyses are done for better matching of the antenna designed in Step-2. Note that the shorting pin is put in the rightmost lower corner of the patch to increase the current path length. The design parameters are chosen as : w_1, w_2, w_3 for the lower arm of the patch and w_4, w_5, w_6 for the upper arm of the patch. These parameters are parametrically changed and their effects are observed. Parametric analysis results are shown in Figure 3.22 and Figure 3.23. According to these results, antenna geometry has been changed. Selected and applied parameters are given in Table 3.2. The resultant geometry and the simulated return loss of the proposed antenna are

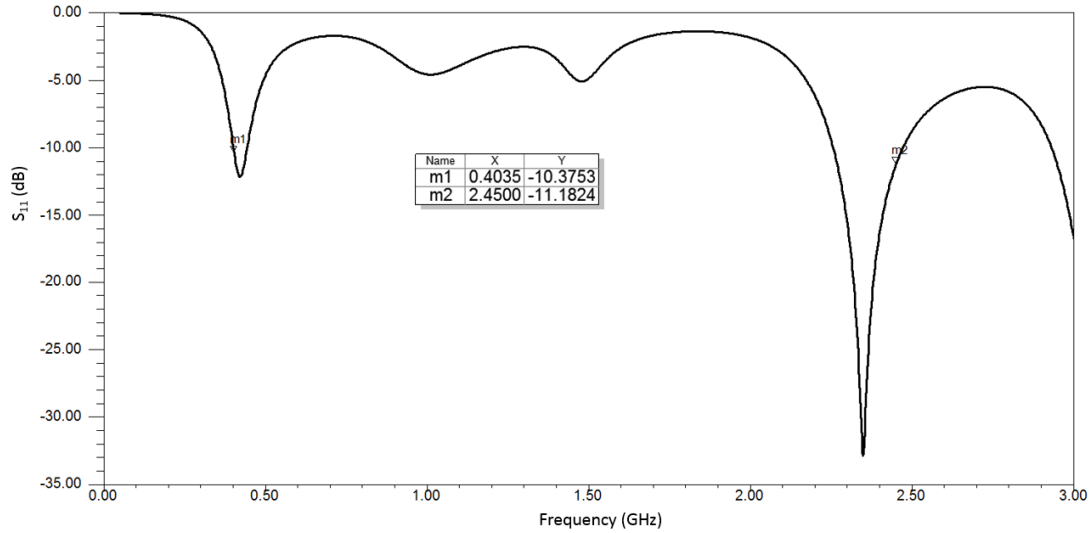


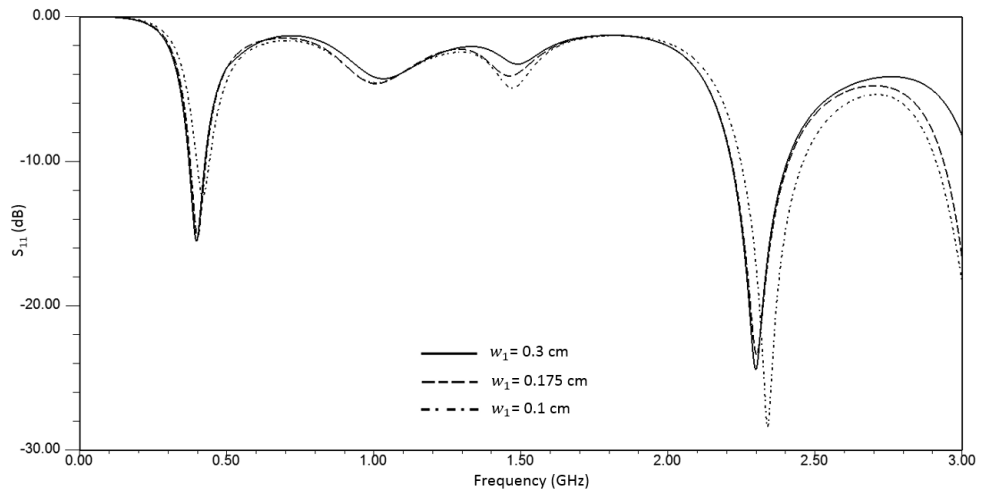
Figure 3.21: Simulated S_{11} of the antenna in Step-2

illustrated in Figure 3.24 and Figure 3.25, respectively. It is observed that the matching of the antenna improves for the selected parameters. Finally, optimization tool of the HFSS is used as shown in Figure 3.26. *Quasi Newton* optimization is preferred due to its speed and accuracy in cases of insignificant numerical noise [24]. The maximum number of iterations is set to 300. Cost function is defined for both the MICS and ISM bands. The goals are selected as: $S_{11} @403.5 \text{ MHz} \leq -15 \text{ dB}$ and $S_{11} @2.45 \text{ GHz} \leq -15 \text{ dB}$. The optimized variables are designated with their minimum and maximum values.

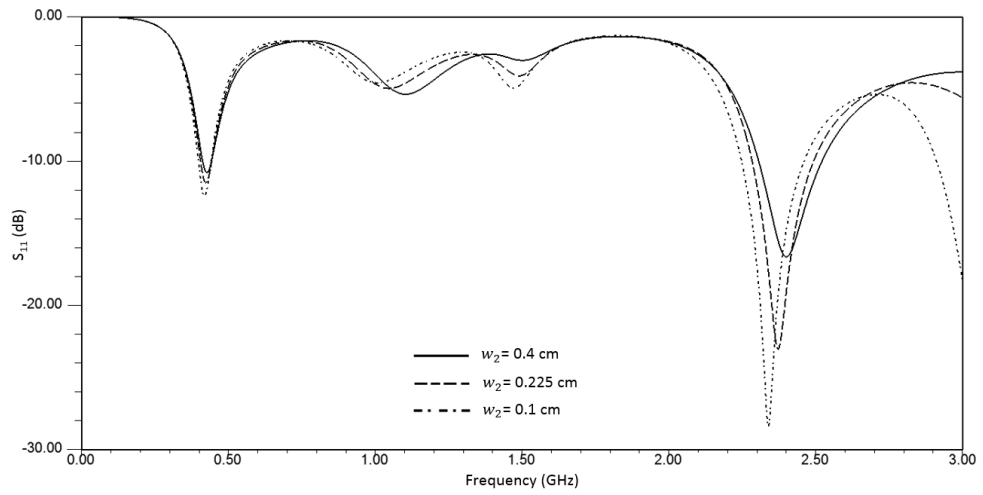
Table3.2: Selected dimensions according to conducted parametric study results (See Figure 3.22 and Figure 3.23)

Parameter	Dimesion (cm)	Parameter	Dimesion (cm)
w_1	0.175	w_4	0.2
w_2	0.225	w_5	0.1625
w_3	0.125	w_6	0.175

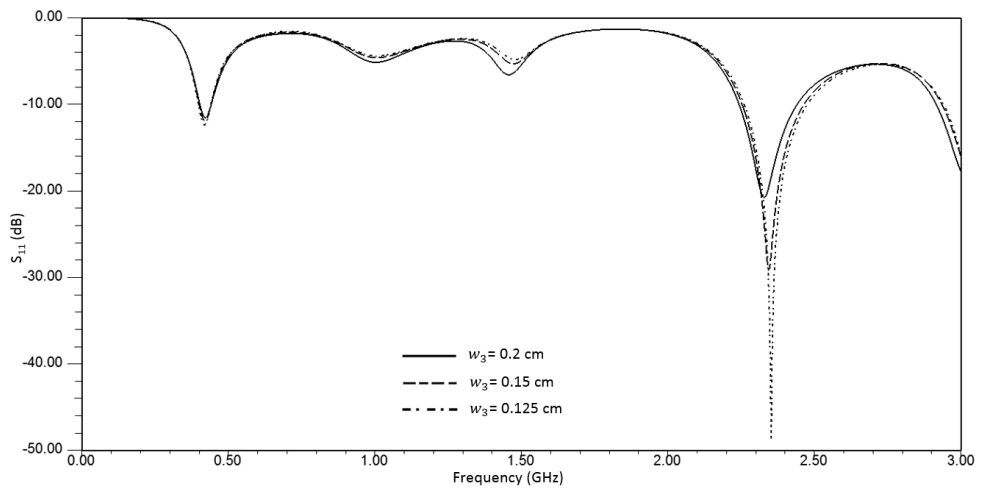
Figure 3.27 shows the geometry of the final design with all related optimized parameters. Detailed dimensions are provided in Table 3.3. Note that the substrate thickness is 1.27 mm. The simulated return loss of the antenna is



(a)

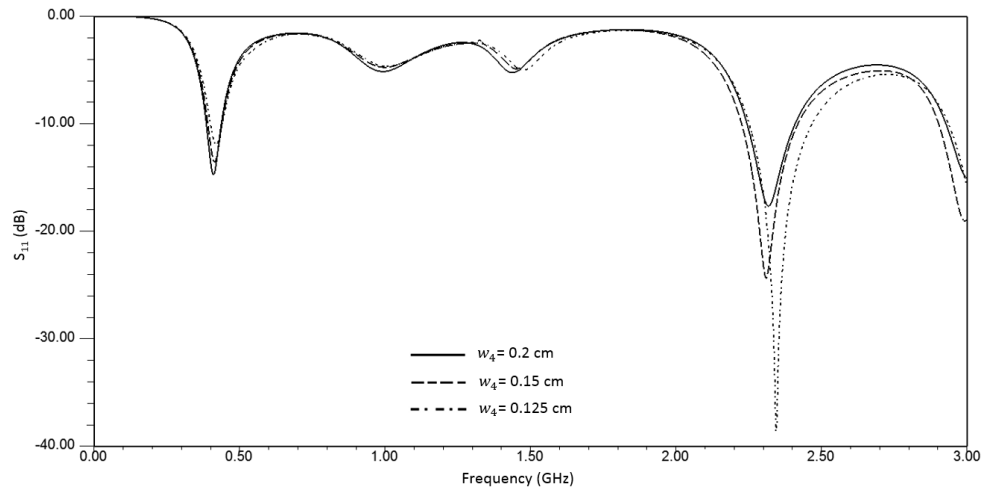


(b)

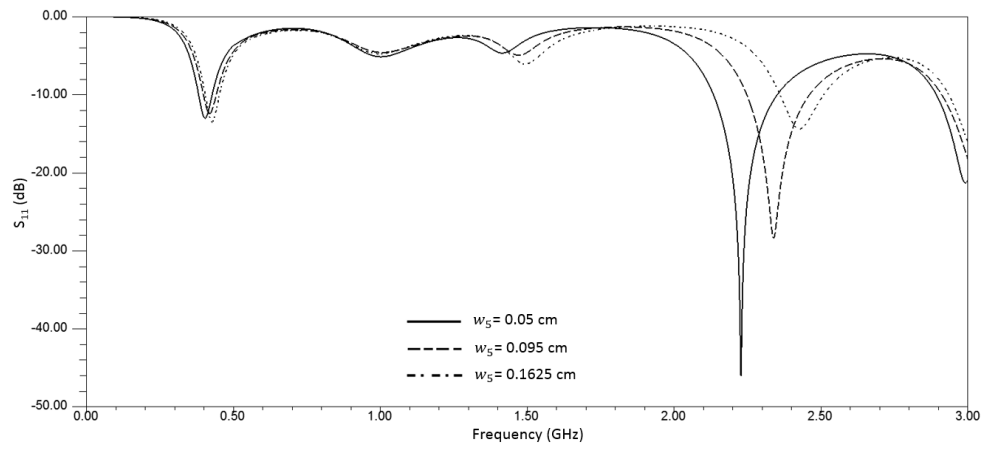


(c)

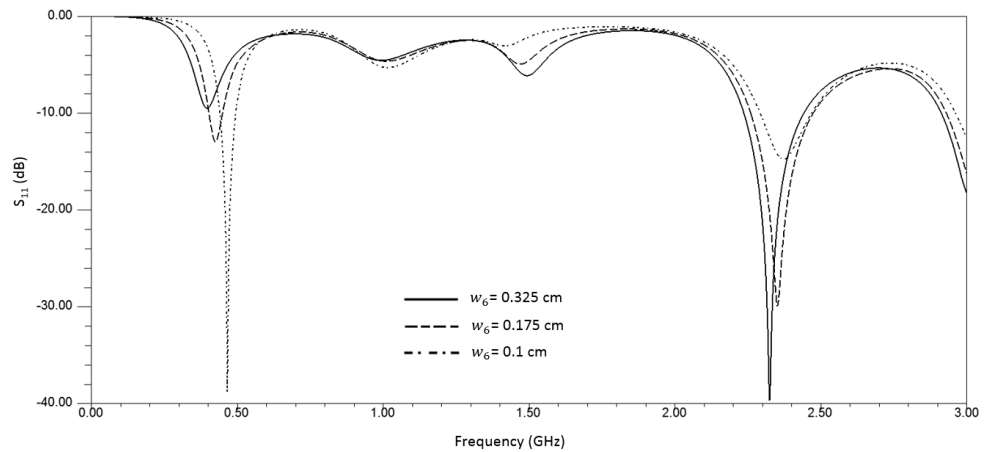
Figure 3.22: Effect of lower patch arm parameters w_1, w_2 and w_3 on the resonant frequency



(a)



(b)



(c)

Figure 3.23: Effect of upper patch arm parameters w_4, w_5 and w_6 on the resonant frequency

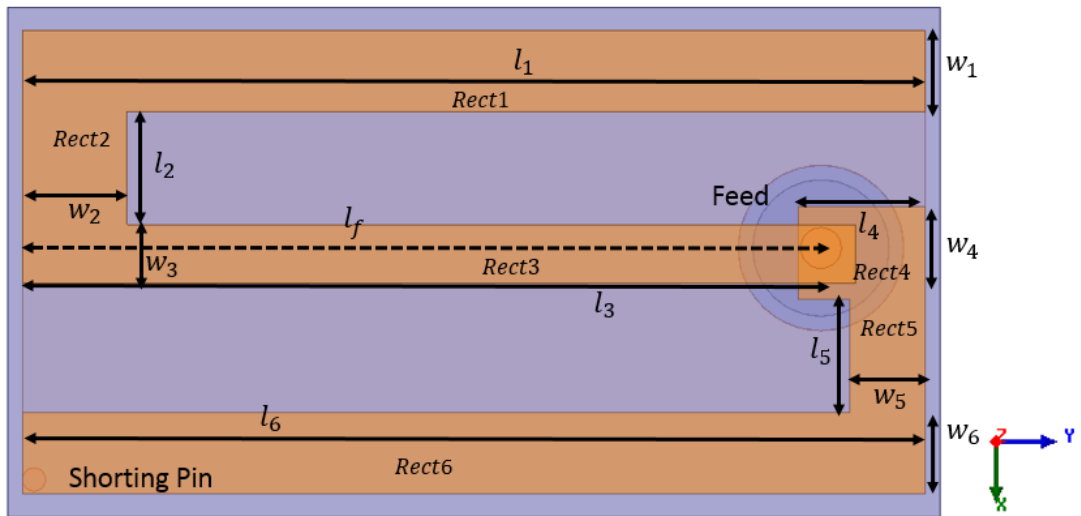


Figure 3.24: Top view of the antenna designed according to parameters given in Table 3.2

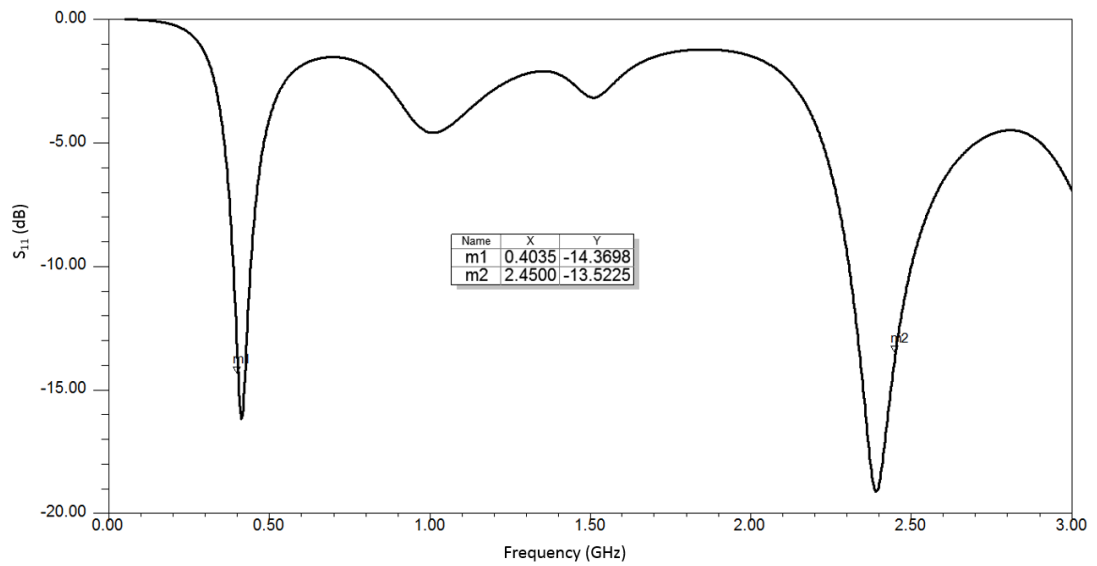
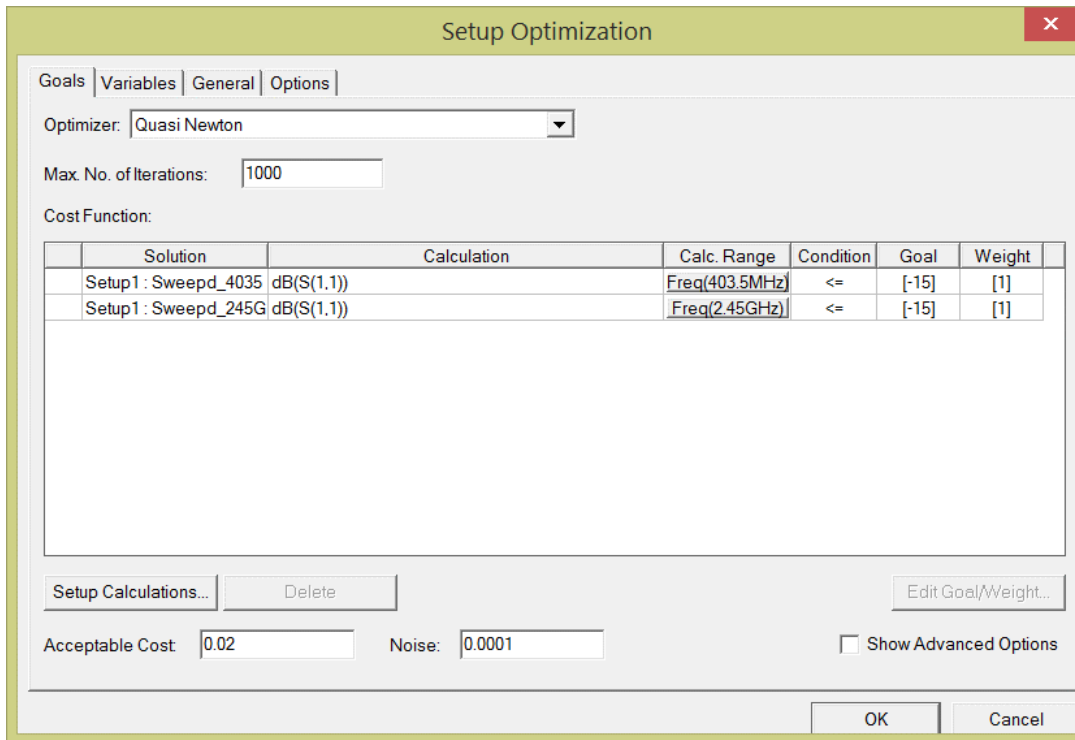
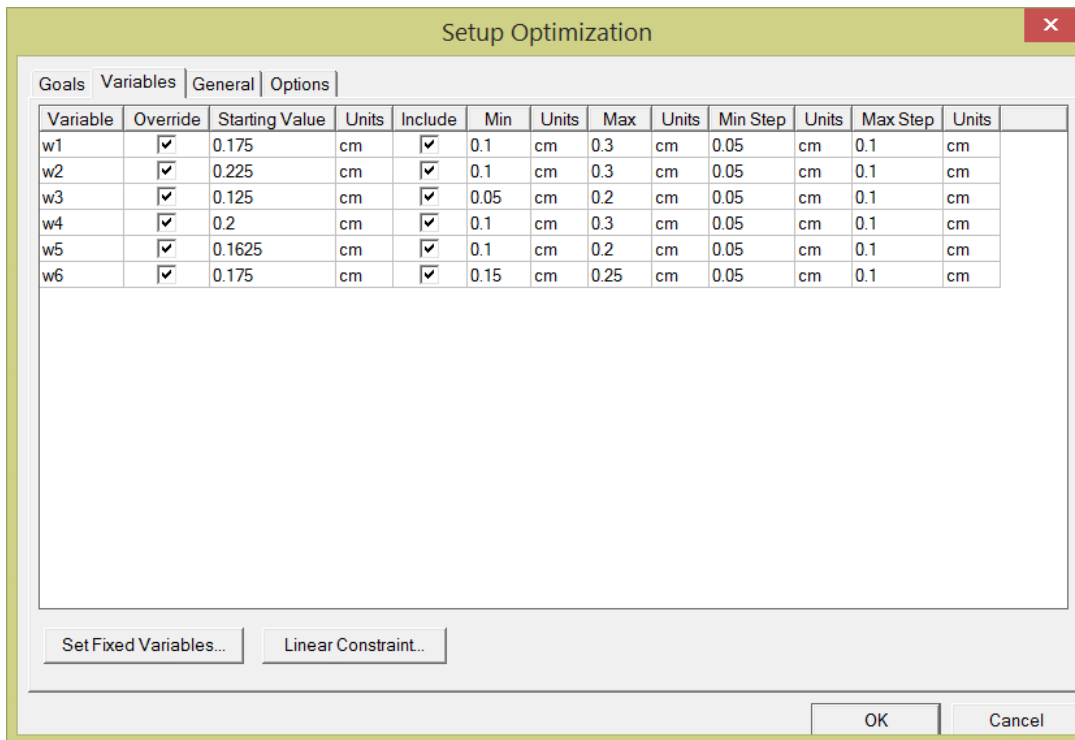


Figure 3.25: Simulated S_{11} of the antenna designed according to parameters given in Table 3.2



(a)



(b)

Figure 3.26: Optimization setup in HFSS (a) Goal definition for both MICS and ISM bands (b) Optimization parameters

depicted in Figure 3.28. The antenna resonates at 403.5 MHz with a reflection coefficient of -18.2 dB, and a wide 10-dB bandwidth of 56 MHz, which covers the MICS band. The antenna, moreover, resonates at 2.45 GHz with a reflection coefficient of -23 dB, and a wide 10-dB bandwidth of 200 MHz, which covers the ISM band. Current distribution of both MICS and ISM bands are shown in Figure 3.29. It is observed that the entire path from the left end to the right end of the patch contributes to the MICS band. The maximum simulated gain of the antenna is found as -32.9 dBi and -12.7 dBi at 403.5 MHz and 2.45 GHz, respectively (See Figure 3.30).

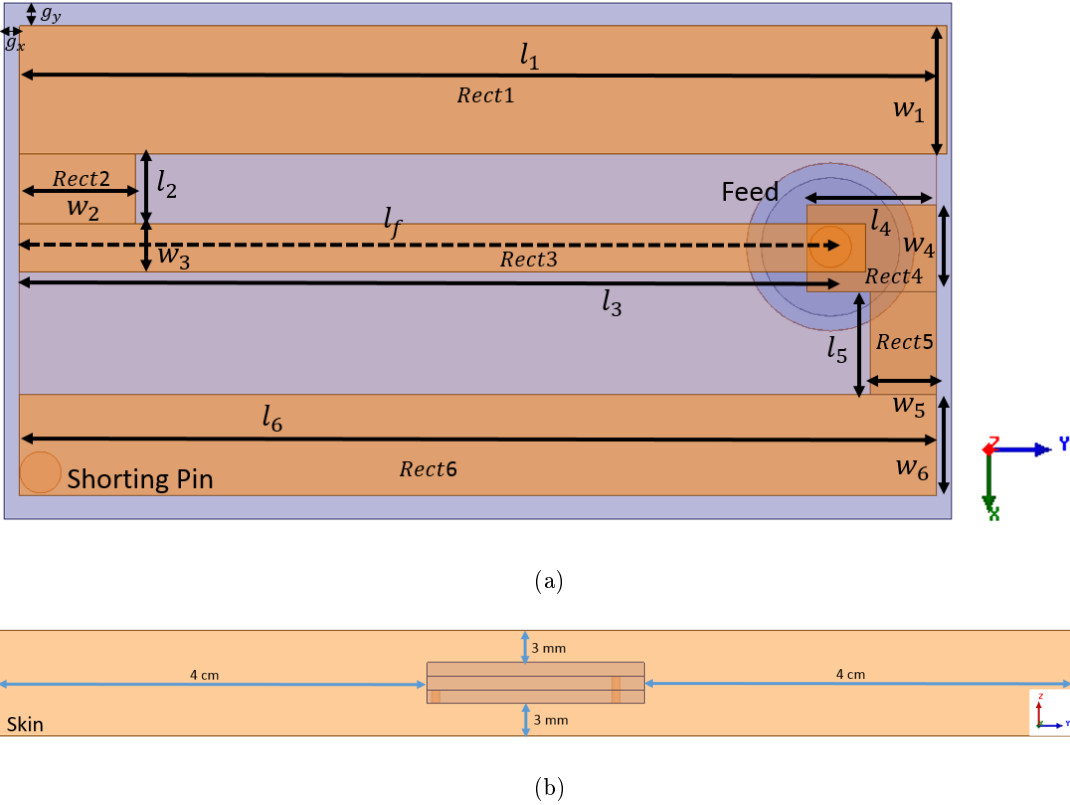


Figure 3.27: Geometry of the proposed antenna with all design parameters (a) Top view of the antenna (b) Side view of the antenna

Table3.3: Antenna design parameters of the final design

Parameter	Dimesion (mm)	Parameter	Dimesion (mm)
l_1	19.5	w_1	2.73
l_2	1.47	w_2	2.47
l_3	18	w_3	1.04
l_4	2.75	w_4	1.86
l_5	2.19	w_5	1.4
l_6	19.5	w_6	2.15
g_x	0.25	g_y	0.35
l_f	17.25		

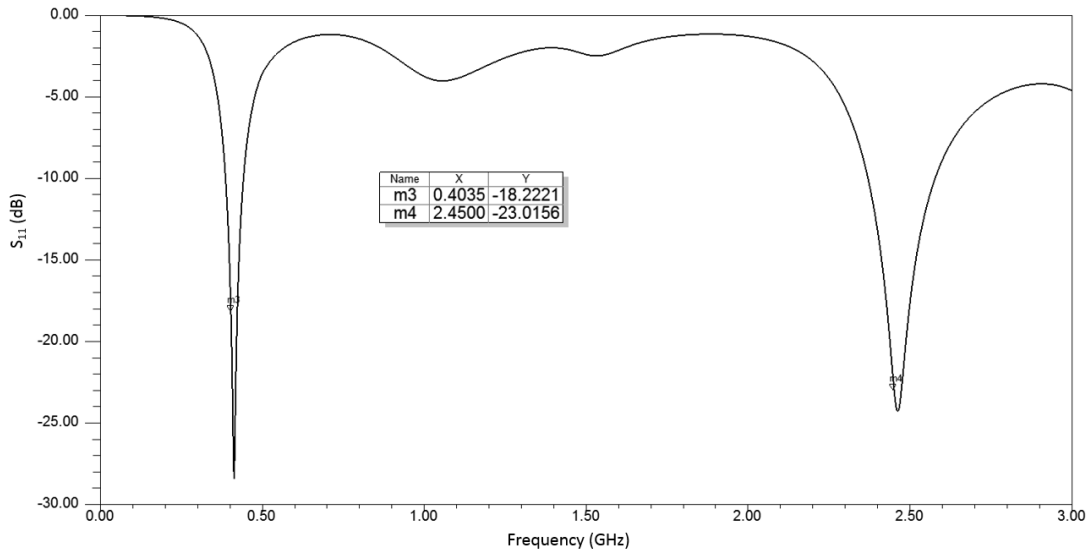
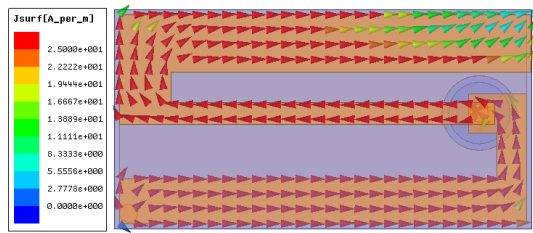
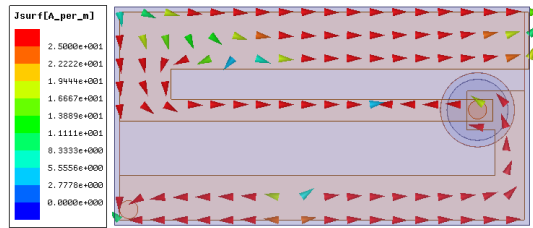


Figure 3.28: Simulated S_{11} of the antenna proposed antenna designed according to parameters given in Table 3.3

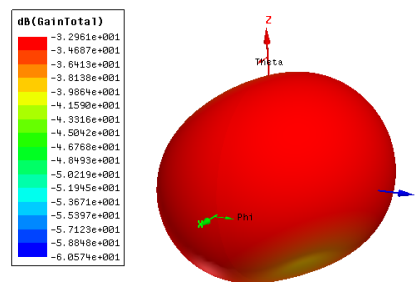


(a)

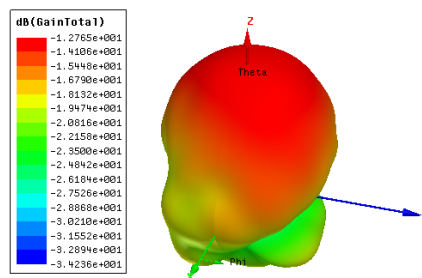


(b)

Figure 3.29: Simulated current density distribution on the patch surface of the proposed antenna (a) 403.5 MHz (b) 2.45 GHz



(a)



(b)

Figure 3.30: Simulated 3D gain pattern of the proposed antenna (a) 403.5 MHz (b) 2.45 GHz

3.3 Realization and Measurement of the Final Design

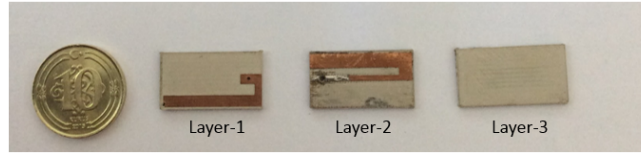
To confirm the validity of the numerical simulations, experimental investigations are carried out for reflection coefficient and communication link measurements.

3.3.1 Realization of the Antenna

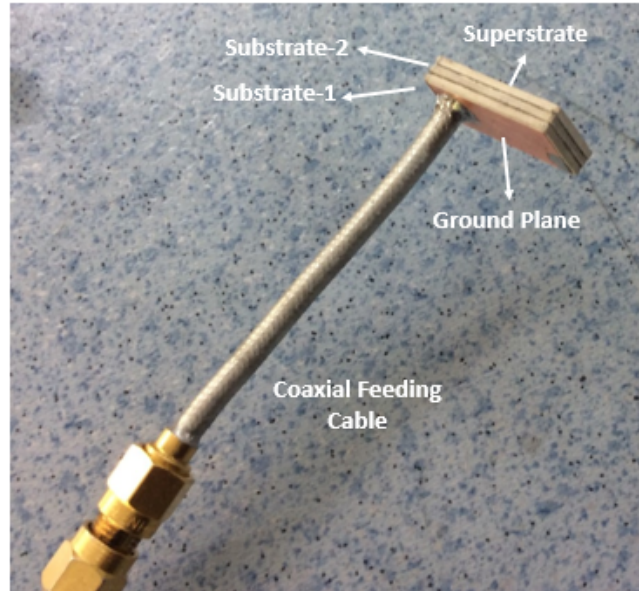
Antenna is fabricated using LPKF-ProMat-H100 circuit board plotter. RO3210 substrate is cut and drilled for feeding cable and shorting pin. Fabricated antenna parts are shown in Figure 3.31. As a coaxial feeding cable, commercially available Huber-Suhner Sucofrom-141 50 Ω coaxial cable is used. Inner conductor of the patch is soldered on the first layer while the outer conductor is connected to the ground plane. The second layer is connected to the first layer using the double-sided tape. Then, the inner conductor of the coaxial cable is soldered to second layer. To prevent the air gap between the layers of the antenna, soldering process has been done carefully. Finally, the third layer, the superstrate layer, is inserted on the top using double-sided tape. The resulted antenna is shown in Figure 3.31. To investigate the effects of double-sided tape on the resonant frequency, simulations are carried out in HFSS. The thickness of the double sided tape is found as 0.025 mm. Since the permittivity of the tape ($\epsilon_{r,tape}$) is unknown, a parametric study is done. The resultant S_{11} of the antenna for tape permittivities 1.5, 2 and 2.5 are given in Figure 3.32. It is observed that, there is a slight change on the resonant frequency and antenna still radiates without disturbing the MICS and ISM band operation.

3.3.2 Return Loss Measurement

Return loss measurements were carried out by N9915A FieldFox Analyzer. Firstly, the proposed antenna is measured in air and the result which compares measured and simulated S_{11} is displayed in Figure 3.33. Since antenna radiates into air, a frequency shift is occurred as expected. To test the antenna in vitro, skin mimicking gels are prepared for both the MICS and ISM bands. MICS band



(a)



(b)

Figure 3.31: Fabricated antenna (a) Fabricated antenna parts (b) Assembled antenna with feeding cable

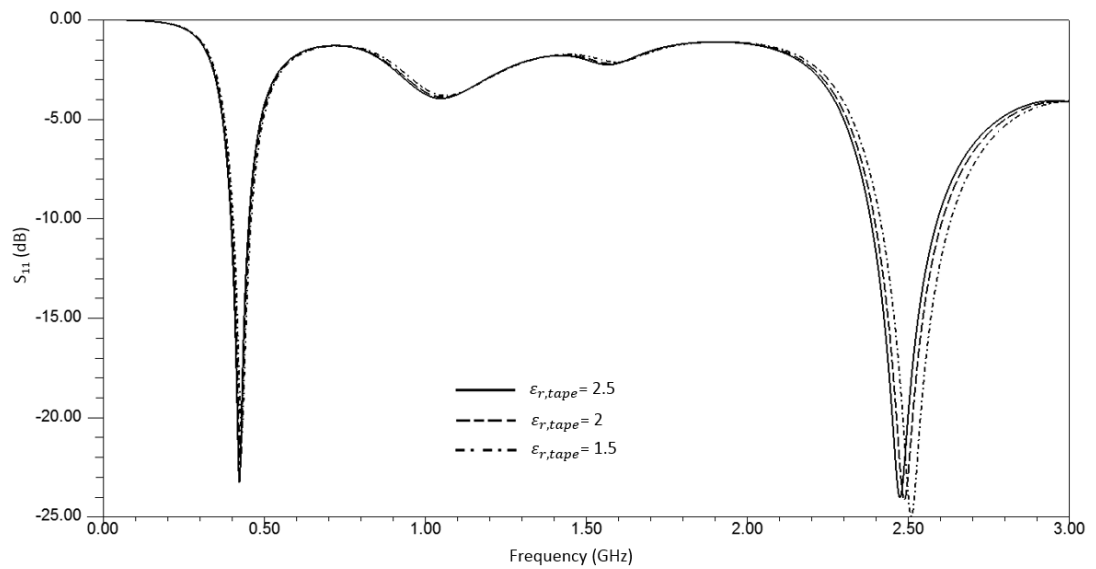


Figure 3.32: Effect of double-sided tape permittivity on the resonant frequency

gel is prepared as explained in the first prototype measurement. Figure 3.34 displays the comparison of the measured and simulated S_{11} of the proposed antenna in the MICS band gel. As seen from the graphs, the results agree well at the MICS band. Two measurements are provided where "Meas-1" represents the measurement result when the antenna is placed in the phantom and "Meas-2" represents the measurement result when the antenna waits in phantom for 1 day. A slight change is observed in the resonant frequency for the second measurement due to two reasons: 1) the phantom starts to become slightly liquid form rather than the gel form in 1 day. 2) the liquid separates the antenna layers and the effective permittivity decreases resulting in an upward shift in the resonant frequency. The measured frequencies range from 376 MHz to 442 MHz (16.5%) at the MICS band for S_{11} less than -10 dB for the first measurement.

For the ISM band measurements, skin mimicking gel is prepared with a recipe taken from [2]. Table 3.4 shows the concentrations of ingredients in ISM gel and Figure 3.35 shows the process to characterize the phantom. The measurement of the phantom's electrical properties (ϵ_r and σ) are conducted via virtual line method [69]. Figures 3.36 and 3.37 show the ϵ_r and σ of the skin-mimicking gel prepared for the ISM band. The measurements are compared with the reference data taken from [19]. Although ϵ_r matches very well with the reference data for the ISM band (Figure 3.36), the conductivity of the material is 2.21 S/m, which is slightly higher than the conductivity of the skin ($\sigma = 1.4407$ S/m) for the ISM band. Prepared phantom, phantom measurement set-up and return loss measurement set-up are shown in Figure 3.38. Figure 3.39 displays the comparison of measured and simulated S_{11} of the proposed antenna in the ISM band gel. As seen from the graphs, the results agree well at the ISM band with a slight difference due to the higher conductivity of the phantom.

Table3.4: Recipe for skin mimicking gel in the ISM band

ISM Band	
Sugar	% 53
De-ionizaed Water	% 47
Agarose	Add 1 g in 100 ml solution

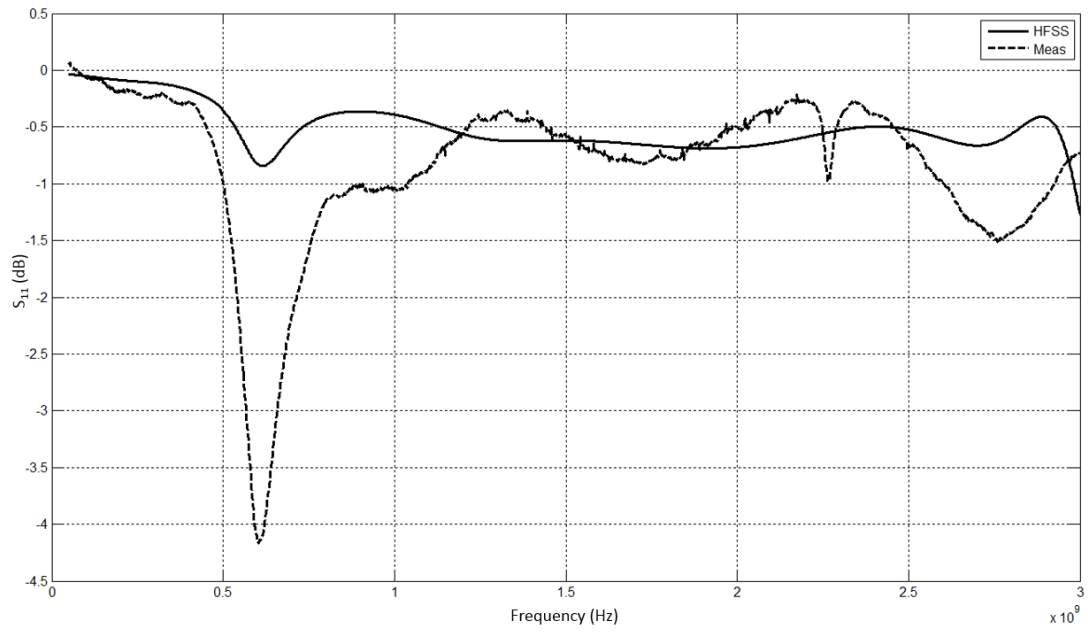


Figure 3.33: Comparison of simulated and measured S_{11} of the proposed antenna in air

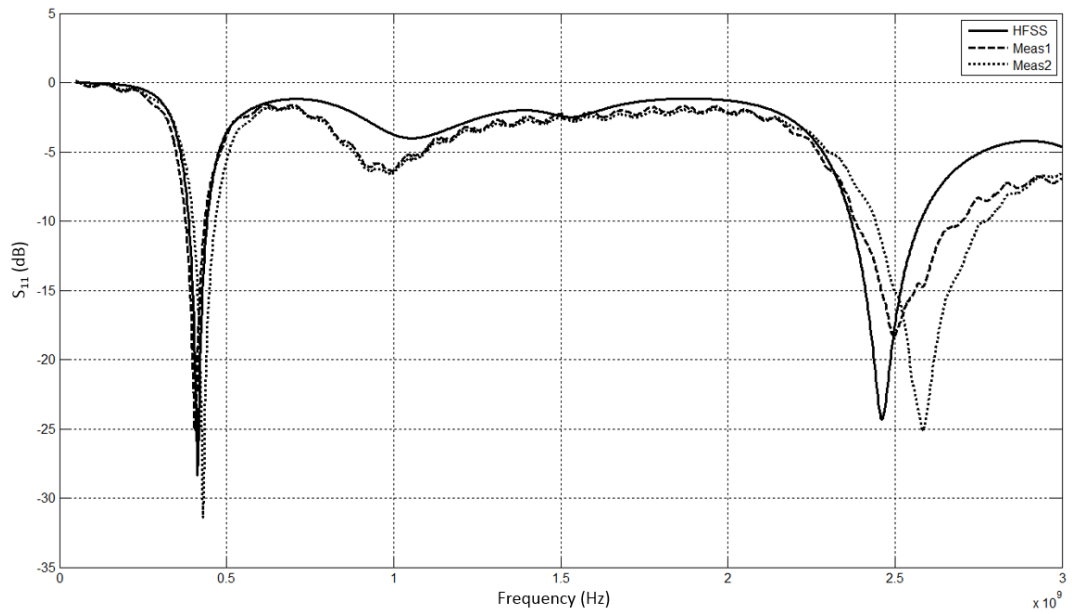


Figure 3.34: Comparison of simulated and measured S_{11} of the proposed antenna in MICS band phantom



Figure 3.35: Process of preparing skin mimicking gel for ISM band

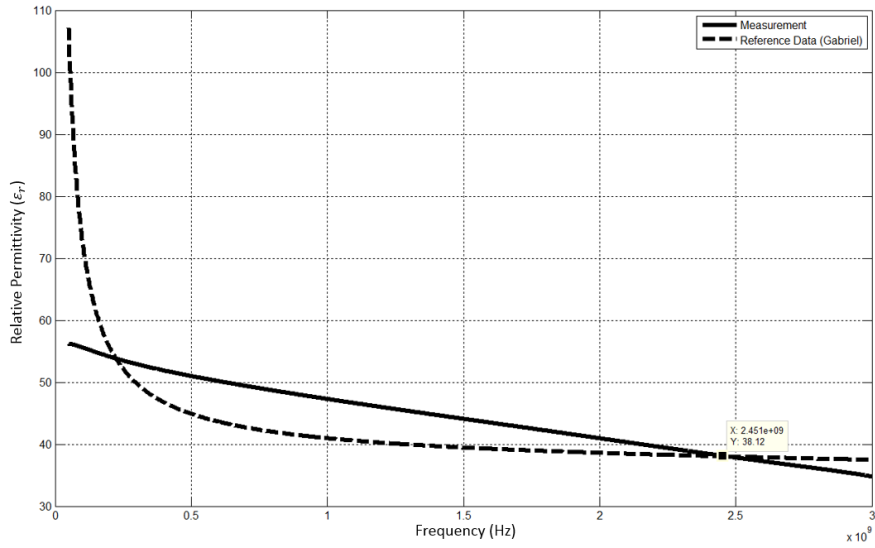


Figure 3.36: Comparison of permittivity of the ISM band skin-mimicking gels with the reference data from [19].

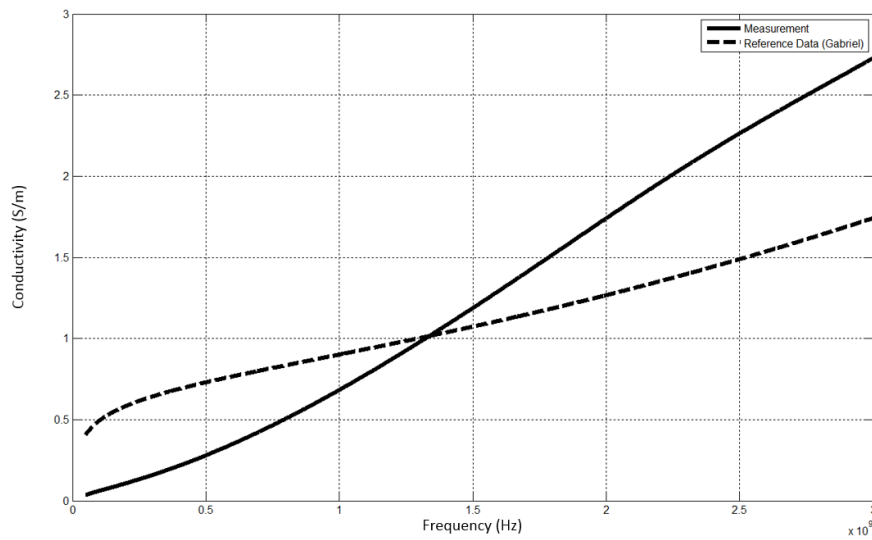


Figure 3.37: Comparison of conductivity of the ISM band skin-mimicking gels with the reference data from [19].

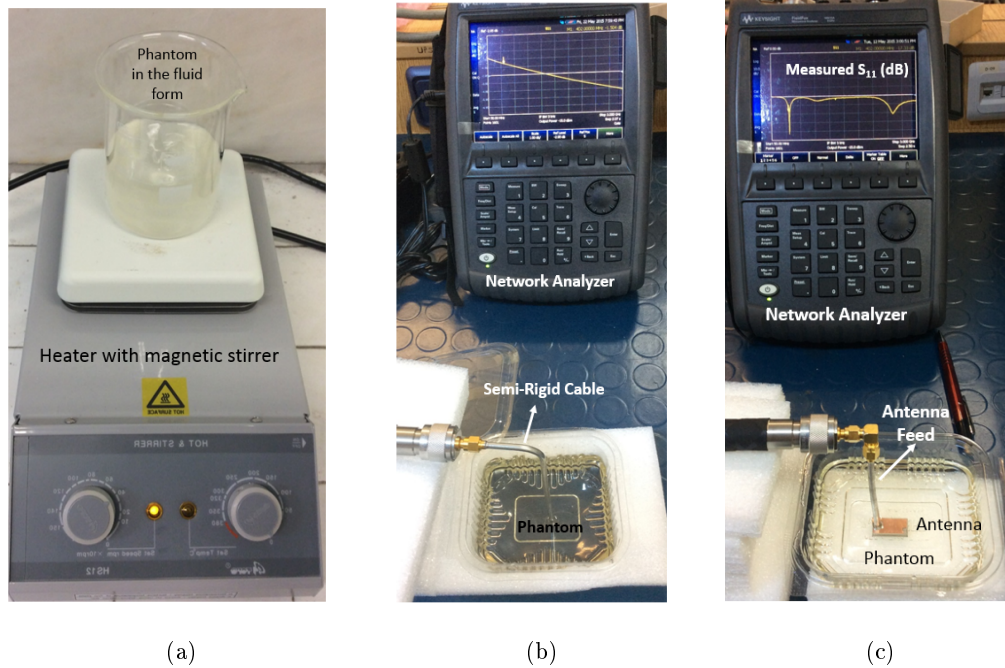


Figure 3.38: (a) Skin mimicking phantom (b) Measurement of the phantom's electrical properties (c) Return loss measurement

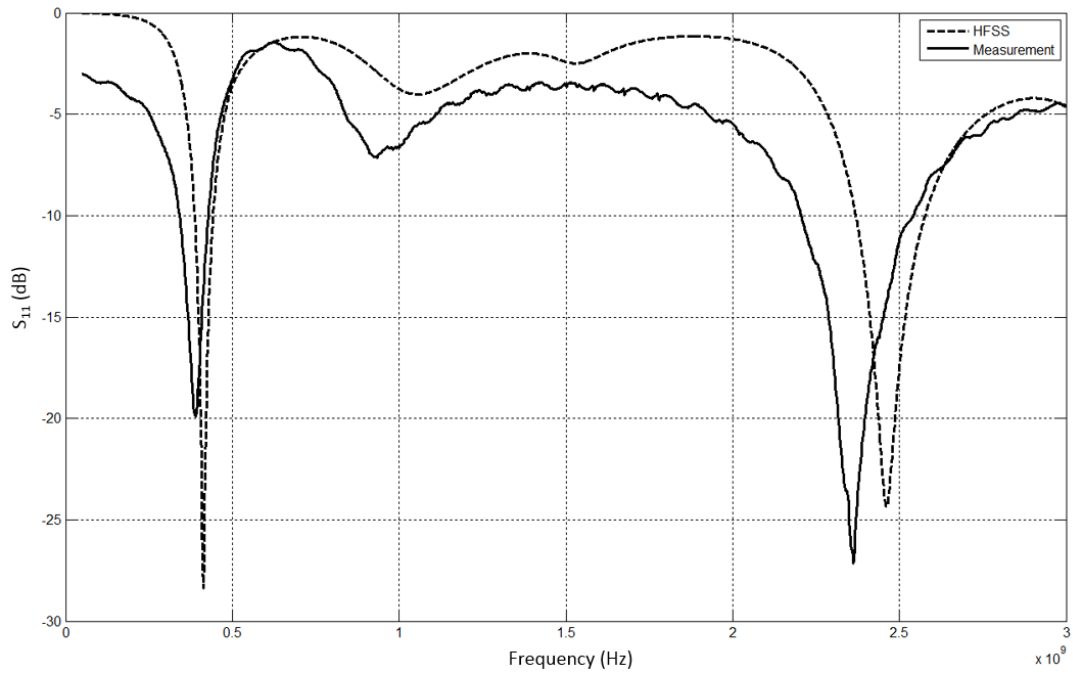


Figure 3.39: Comparison of simulated and measured S_{11} of the proposed antenna in ISM band phantom

3.3.3 Communication Link Measurement

Communication link measurements were performed in order to check the functioning of the proposed antenna. The system behaviour was assessed with the use of Microsemi-Zarlink Application Development Kit for Medical Telemetry (ZLE70102) [70]. The kit is funded by METU-EEE and Kardiosis Ltd. via the Scientific and Technological Research Council of Turkey (TUBITAK) (project number: 113S471) project. Development kit shown in Figure 3.40 consists of "Implant Application Unit (IAU)" and "Base Station Application Unit (BAU)". Implant Application Unit contains optimized MICS band radio transceiver and the antenna which is optimized for air. On the other hand, Base Station Application Unit contains both MICS band radio transceiver and 2.45 GHz wake-up transmitter and dual band antenna (400 MHz and 2.45 GHz) for operation in the air. Units are controlled using the PC based graphical user interface (GUI) provided by Zarlink. Communication is established between the IAU and BAU when the GUI indicates "In Session" for the "Operational State" as shown in Figure 3.41. For link measurement, antenna of the IAU is changed with the designed antenna which is inserted into the gel phantom. Experiments are performed within the anechoic chamber in the EEE Antenna Measurement Laboratory of METU. Photographs are presented from the telemetry set-up as shown in Figure 3.42. The operational state is checked to see the reliable data telemetry. When the GUI indicates "In Session", the data has been sent and received efficaciously from the IAU as shown in Figure 3.43. As a message "Hello Implant" is sent from IAU and received from BAU in 4 meter range.

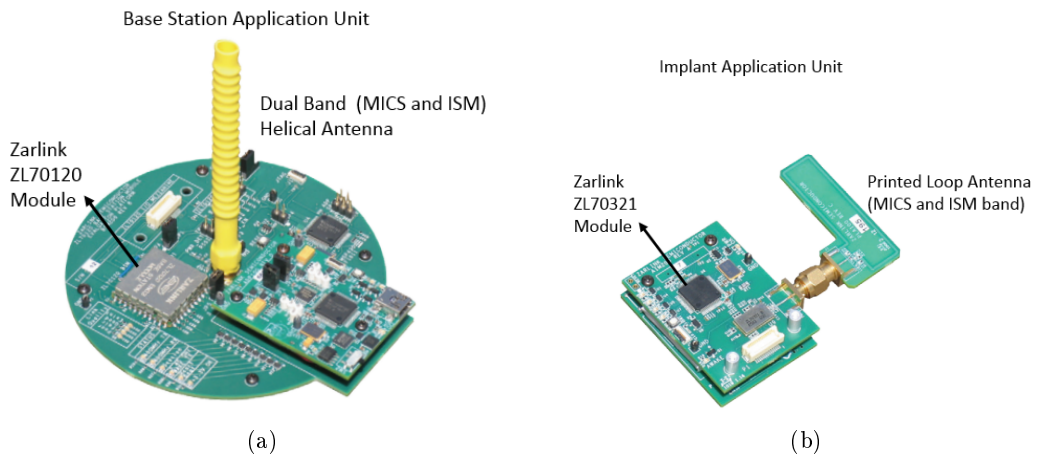


Figure 3.40: Medical telemetry application development kit: ZLE70102 (a) Base Station Application Unit (BAU) (b) Implant Application Unit (IAU)

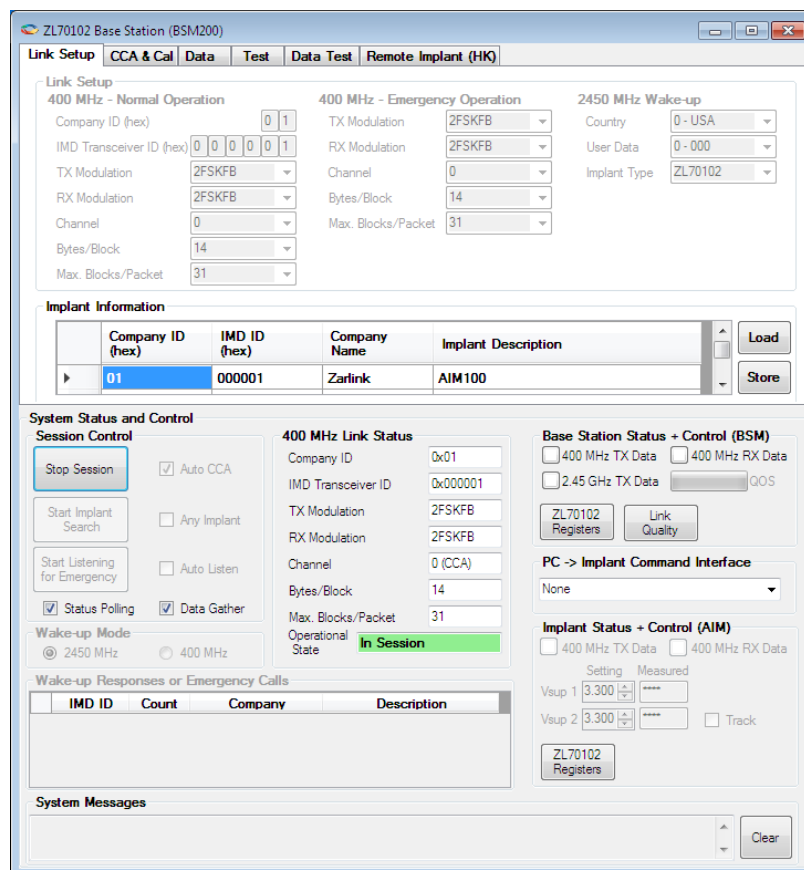


Figure 3.41: GUI for the BAU: Green colored "In Session" indicates that communication is established between BAU and IAU

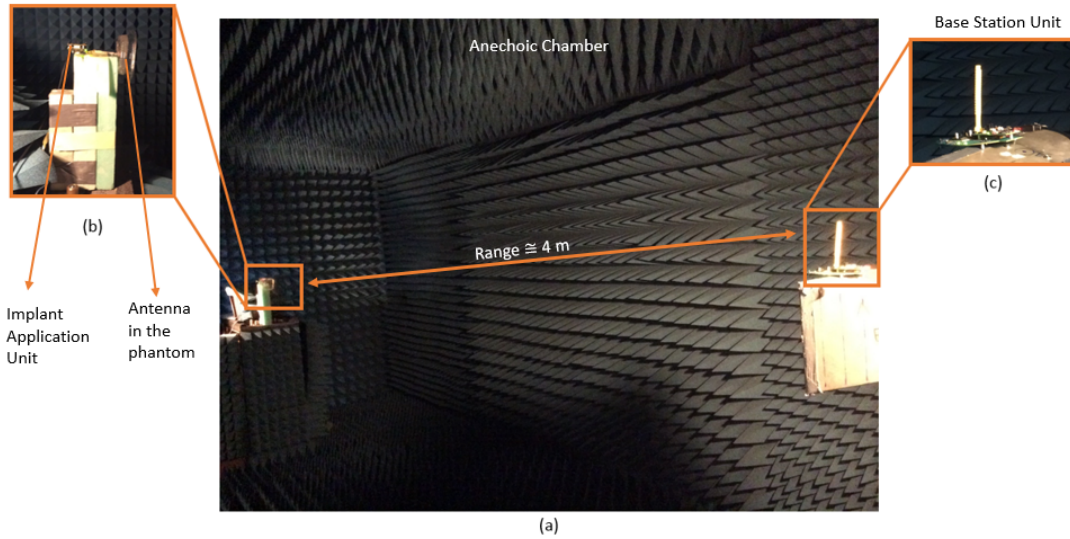


Figure 3.42: Telemetry setup: (a)Antenna test-bed in anechoic chamber (b) IAU with implant antenna inserted in phantom (c) Base Station Application Unit (BAU)

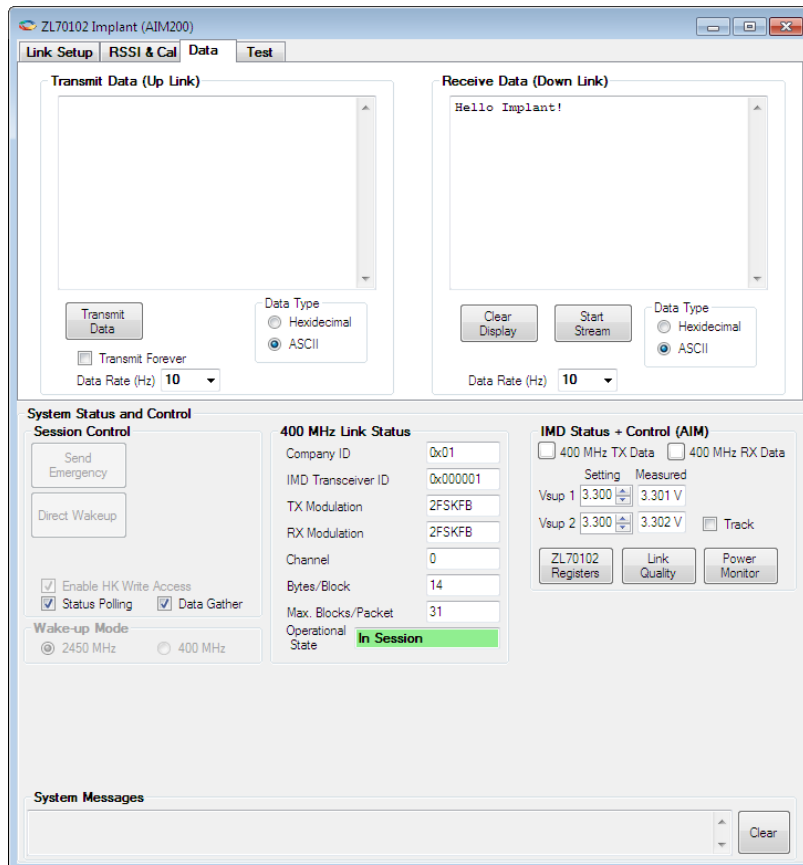


Figure 3.43: GUI for the IAU: "Hello Implant!" message is received.

CHAPTER 4

RESULTS AND DISCUSSION

4.1 Introduction

Design and realization of a dual band implantable antenna operating in skin phantom are presented in previous chapters. In this chapter, patient safety, effects of different phantoms on the resonant frequency, effects of coaxial cable and far field properties of the electrically small antennas are analyzed. For each issue, the feasibility and limitations of the proposed antenna are explored.

4.1.1 Patient Safety

In this thesis study, the proposed antenna is designed using RO3210 as substrate and superstrate material. However, RO3210 is not a biocompatible material. In order not to harm surrounding tissue two typical approaches are applied as mentioned in Section 1.2.4 (See Figure 4.1). For the first approach, antenna is directly designed on biocompatible alumina (Al_2O_3) ceramic ($\epsilon_r = 9.8$). Figure 4.2 represents comparison of simulated S_{11} of the antenna fabricated on RO3210 and Al_2O_3 ceramic substrate. It is observed that there is a slight change in resonant frequency in ISM band, however, it still covers both MICS and ISM bands with $|S_{11}| < 10$ dB. For future applications, biocompatible metals, such as silver palladium, can be used instead of copper. The other approach is encasing the antenna with a thin layer of low-loss biocompatible material. Silastic MDX-4210 biomedical grade elastomer ($\epsilon_r = 3.3$, $\sigma = 0.01$ S/m) is used in numerical simulations for biocompatible encapsulation. To investigate the effects of the

thickness of encased biocompatible material simulations are carried out in the HFSS. The S_{11} of the antenna for different silicone thicknesses ($h_{silicone}$) are given in Figure 4.3. It is observed that the thicker the encased biocompatible material, the more the frequency shifts in the ISM band. Since low permittivity silicone decreases the effective permittivity, the antenna becomes electrically larger and resonant frequency shifts upward. Therefore, a thin layer of silicone ($h_{silicone}=0.03$ mm) can be used to deal with the biocompatibility issues.

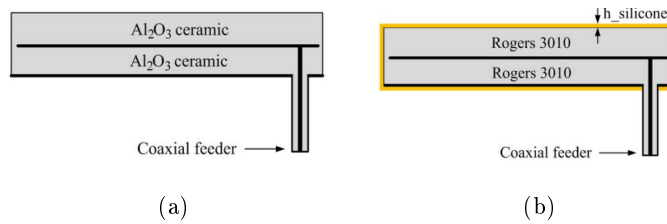


Figure 4.1: Two approaches for biocompatible antenna design (a) Antenna fabricated on biocompatible material (b) Antenna encased with biocompatible material [7]

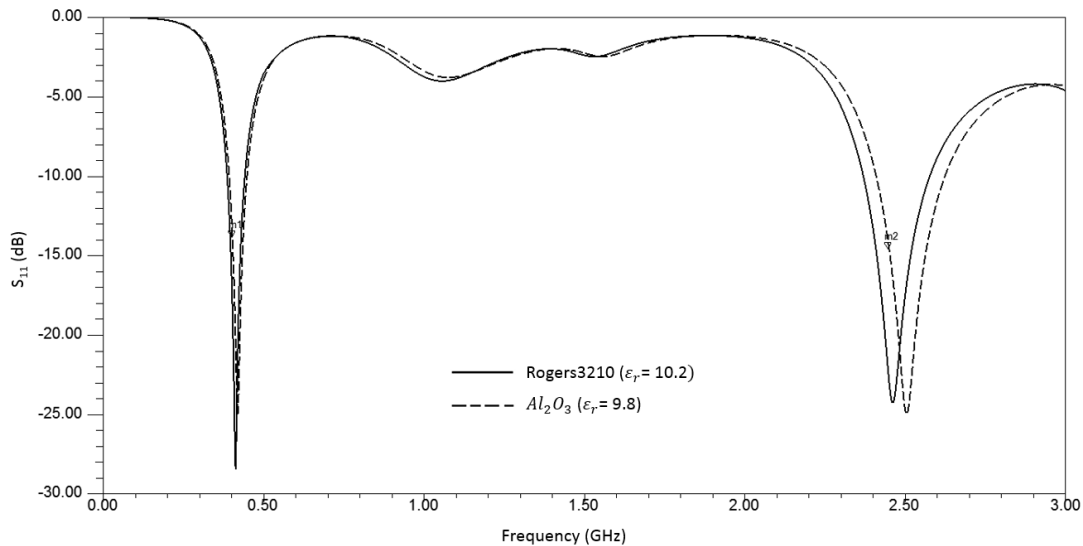


Figure 4.2: Comparison of simulated S_{11} of the antenna fabricated on RO3210 and Al_2O_3 ceramic substrate

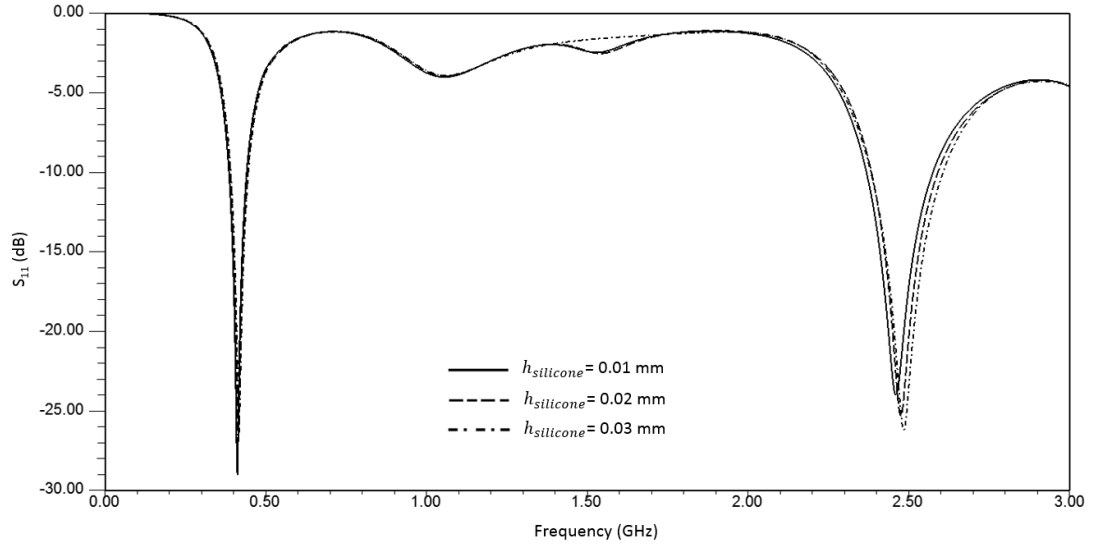


Figure 4.3: Comparison of simulated S_{11} of the antenna for different thickness of encased biocompatible material

Another issue related with the patient safety is the specific absorption rate (SAR). To ensure human safety, 10-g averaged SAR should not be larger than 1.6 W/kg [36]. Simulations are carried out using HFSS to determine the SAR distribution of the antenna. The simulation model presented in Figure 4.5 gives the simulated 10-g average SAR distribution of the antenna at 403.5 MHz and 2.45 GHz at an input power of 1 W. The mass density of the skin is taken as $1.01 \times 10^3 \text{ kg/m}^3$ [71]. The allowed transmitted power to satisfy the SAR regulation is determined as 4.92 mW and 6.37 mW for 403.5 MHz and 2.45 GHz, respectively.

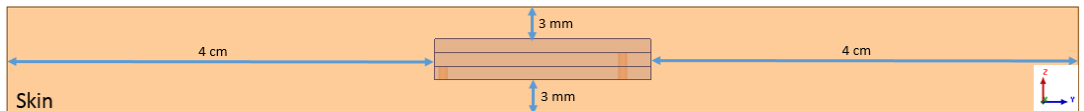
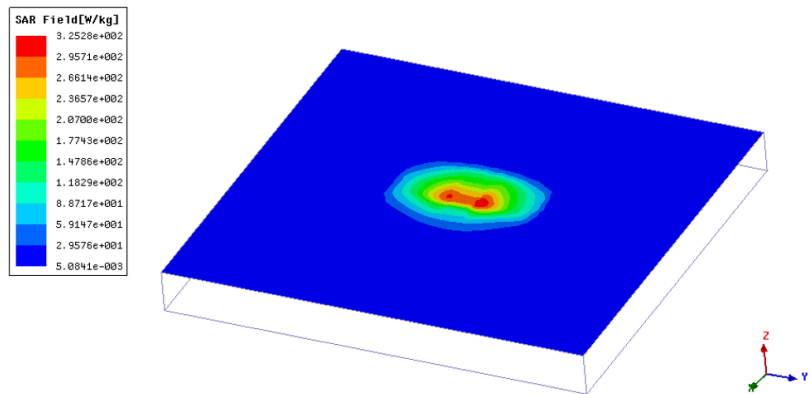
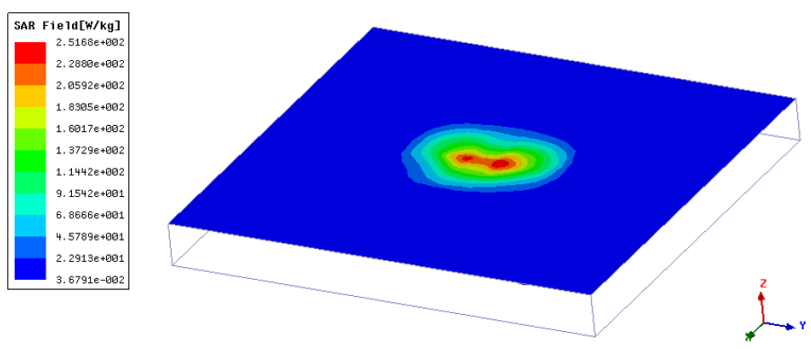


Figure 4.4: Side view of the simulation model used for the calculation of the SAR



(a)



(b)

Figure 4.5: Simulated average SAR of the antenna with 1 W input power (a) 403.5 MHz (b) 2.45 GHz

4.1.2 Effect of Different Phantoms

In this section, sensitivity of the proposed antenna is analyzed for different phantoms. The simulated return loss is studied and compared in four simulation models given in Figure 4.6. Referring to [7], the effect of implant position is evaluated in skin, fat and muscle tissues. The dielectric properties of three tissues are taken from [19]. Simulated return loss results for each case is shown in Figure 4.7. It is observed that the resonant frequency of the proposed antenna has a significant shift to a higher frequency when the antenna is implanted in a fat layer (Case 2 and Case 3), on the other hand, resonant frequency has a slight change when the antenna was implanted in a muscle layer (Case 4). This situation is caused by the fact that the permittivity and conductivity of fat are much lower than those of skin and muscle, while the dielectric properties of skin and muscle are relatively close to each other (See Figure 4.8).

4.1.3 Effect of Coaxial Cable

In this section, the feeding cable's effect is discussed in order to obtain correct proof of the desired performances. Since coaxial feeds are unbalanced, current distributions on the ground plane of the antenna can flow on the external surface of the feeding cable. This situation may provide erroneous results, such as resonant frequency shift [21]. In order to investigate the coaxial cable's effect, three simulation models given in [7] are utilized, namely:

- setup 1: direct contact between the cable and the body phantom (Figure 4.9-a)
- setup 2: presence of biocompatible material (Silastic MDX-4210 biomedical grade elastomer, thickness=0.05mm) shell surrounding the cable and ground plane (Figure 4.9-b)
- Reducing the length of the coaxial cable (Figure 4.9-c)

Simulated reflection coefficients for the three different setups are shown in Figure 4.10. It is observed that there is a slight change in resonant frequency indicating

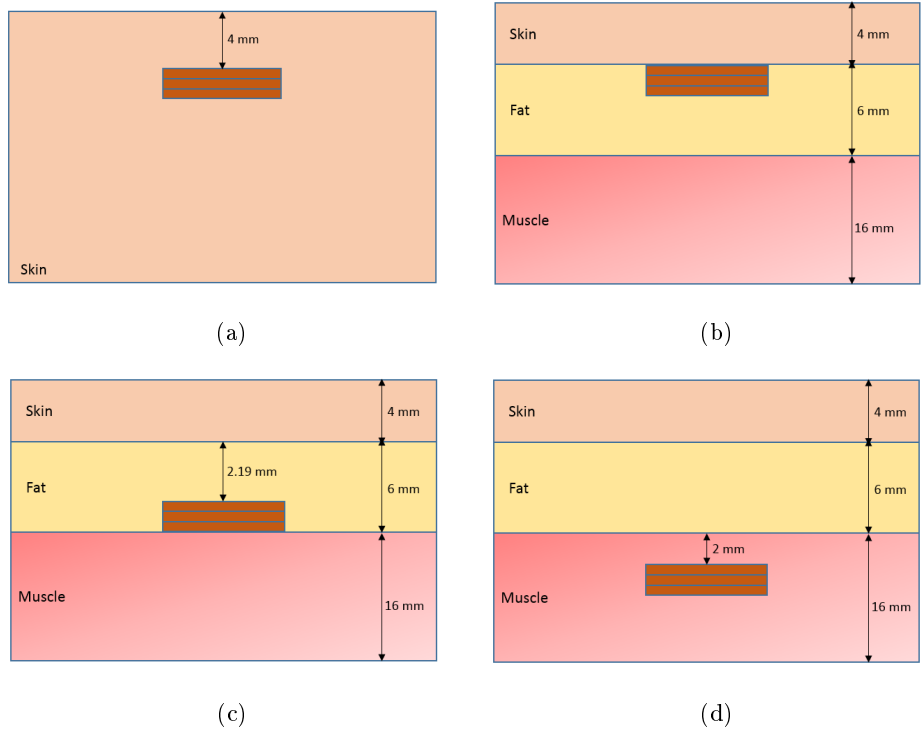


Figure 4.6: Simulation models to investigate the effect of different tissues on the resonant frequency: (a) One-layer skin phantom: case 1 (b) Three-layer tissue phantom where antenna is inserted into skin-fat interface: case 2 (c) Three-layer tissue phantom where antenna is inserted into fat-muscle interface: case 3 (d) Three-layer tissue phantom where antenna is inserted into muscle: case 4

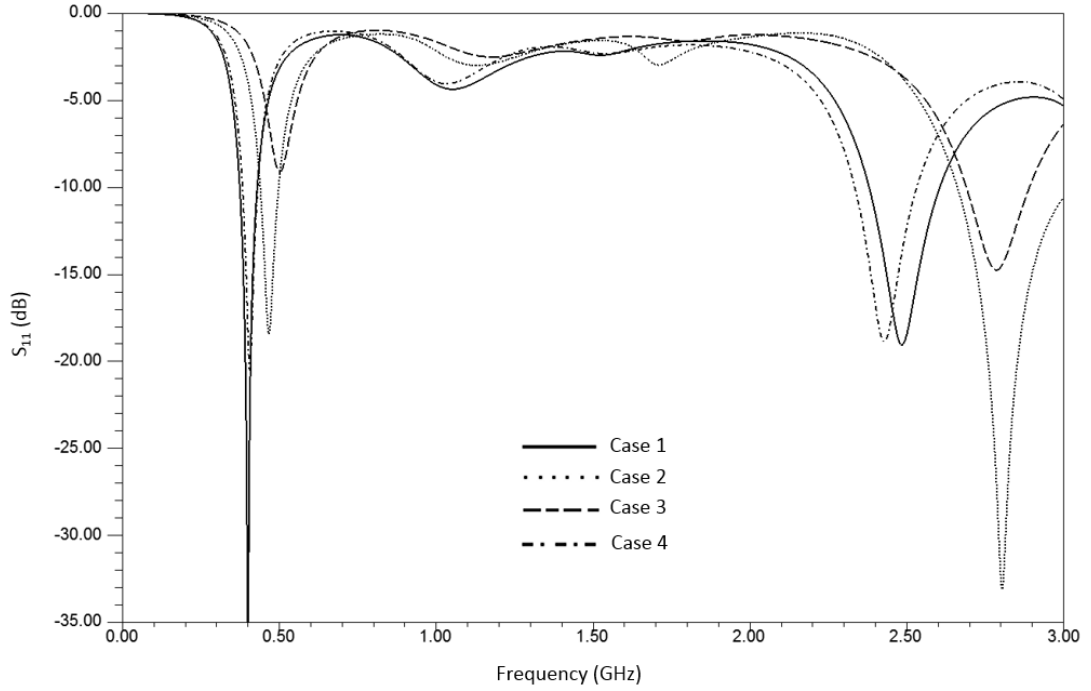


Figure 4.7: Comparison of simulated S_{11} of the antenna for different phantom models given in Figure 4.6

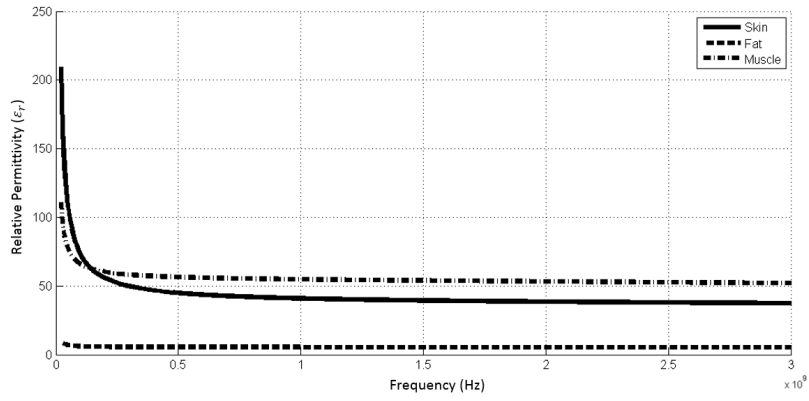
that small coupling exists between the currents flowing on the external metal of the cable and the body phantom [21].

4.1.4 Far Field Properties of the Antenna

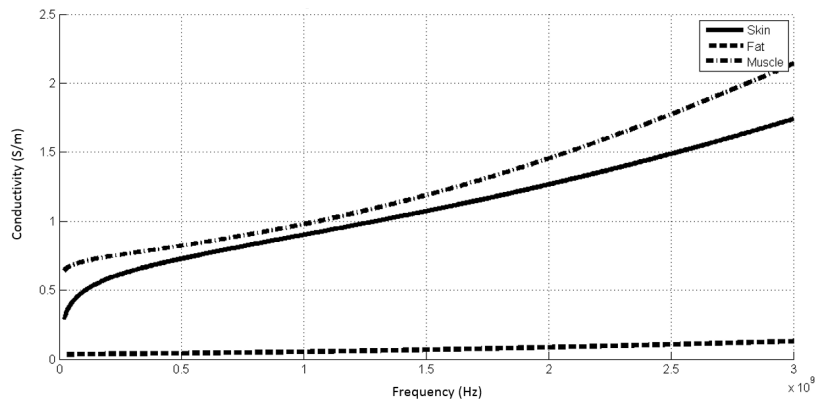
In this section, the far field radiation pattern of an antenna in conducting medium, and the maximum gain measurement of the Electrically Small Antennas (ESAs) are discussed.

4.1.4.1 Effects of Conducting Medium on the Antenna Pattern

When considering the antennas in lossy matter, the standard definition of far field antenna pattern become useless since the radiation from different parts of the antenna are not attenuated in the same way [20]. For an easier understanding, a hypothetical, full wave long, wire antenna carrying a uniform current was inserted first into air and then into a conducting medium by Moore [20]. Figure



(a)



(b)

Figure 4.8: Dielectric properties of skin fat and muscle in 20 MHz-3 GHz frequency band: (a) Relative Permittivity (ϵ_r) (b) Conductivity (S/m)

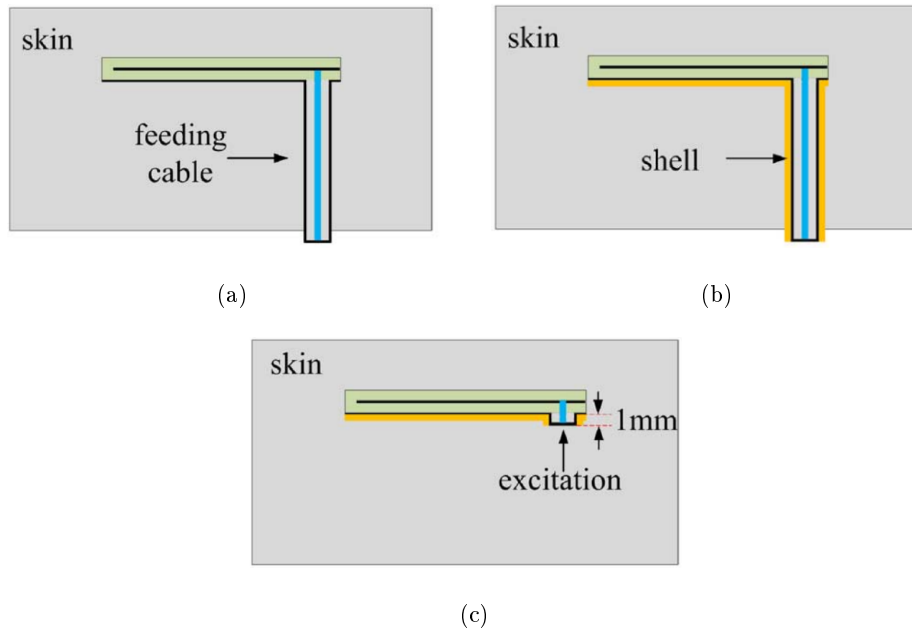


Figure 4.9: Simulation models to investigate the effect of coaxial feed on the resonant frequency: (a) Setup 1 (b) Setup 2 (c) Setup 3 [7]

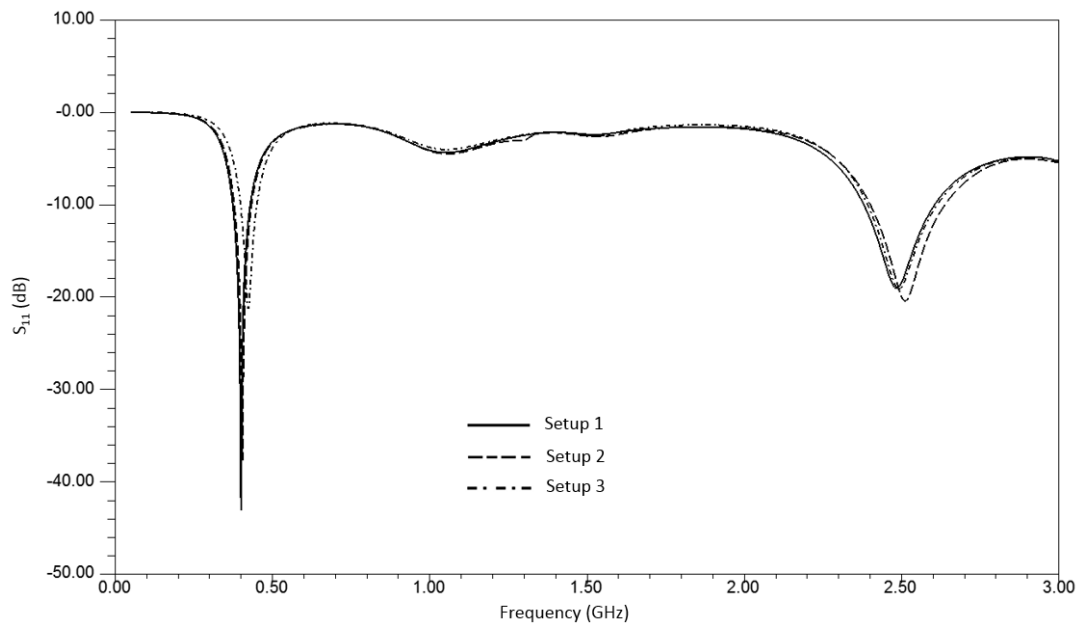


Figure 4.10: Comparison of the simulated S_{11} of the antenna for different feeding models given in Figure 4.9

4.11 represents the results presented in [20]. Note that the change in the antenna pattern does not represent any modification in the field structure. The only difference is the way of looking at the pattern. While measuring the antenna patterns, it is traditional to use a fixed receiver and rotating the transmitting antenna about some axis [51]. When measuring an antenna operating in air, the minor change in the distance between the receiving antenna and the nearest point on the transmitting antenna is not noteworthy, on the other hand, this change causes a significant amount of attenuation when antenna operates in a conducting medium. Therefore, the normal concept of the polar diagram becomes useless for antennas in conducting media [20].

When considering implantable antennas, the problem becomes more pertinent since human body is a complex finite environment. Both the lossy human tissue and the human geometry affects the far field pattern. Merli illustrated this by inserting the same antenna into two phantoms which differ in length (l) and width (w) size, then he observed the related radiation patterns. The results presented by Merli in [21] are reported in Figure 4.12. It is shown that modifying the phantom size affects the radiation pattern significantly. Therefore, antenna pattern must be evaluated using realistic human body models.

4.1.4.2 Measurement of the Maximum Gain of Electrically Small Antennas

The gain measurements of the proposed implantable antenna are conducted in the EEE Antenna Measurement Laboratory of METU. For the ISM band measurements at 2.45 GHz, a standard gain horn antenna (Flann Microwave - Model No:08240-10) is used in the anechoic chamber. The transmitter (Tx) antenna is kept constant. First, the standard gain horn antenna and then the proposed implantable antenna with surrounding phantom tissue are used as receiver (Rx) antenna. For both antennas, the received power level is checked. It is observed that the proposed implantable antenna has nearly the same received power level. Therefore, the gain of the proposed antenna is nearly same as the standard gain horn antenna which is nearly 11 dBi at 2.45 GHz. Similar procedure is applied

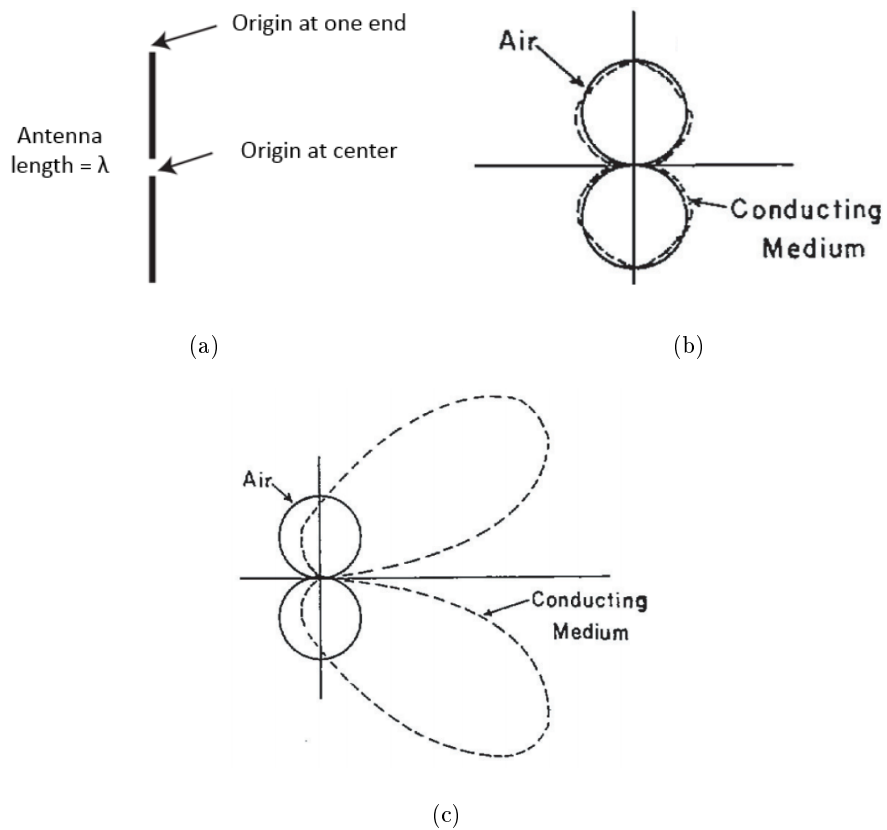


Figure 4.11: Results taken from [20] to show the effect of conducting medium on the radiation pattern of the antenna (a) A hypothetical wire antenna of full wave long carrying a uniform current. The position of the coordinate origins are indicated as: origin at center and origin at one end (b) Patterns in air and conducting medium when origin is at the center (c) Patterns in air and conducting medium when origin is at one end

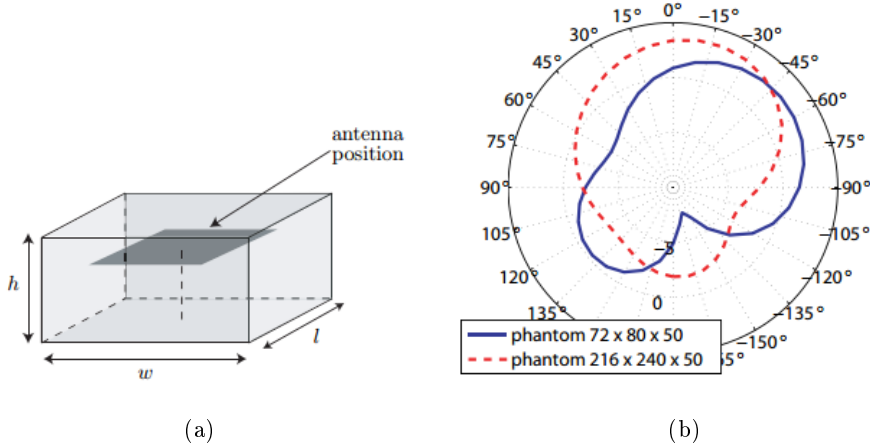
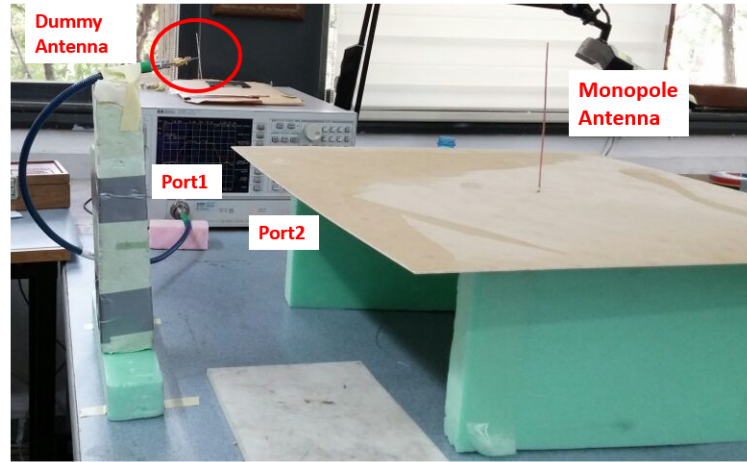


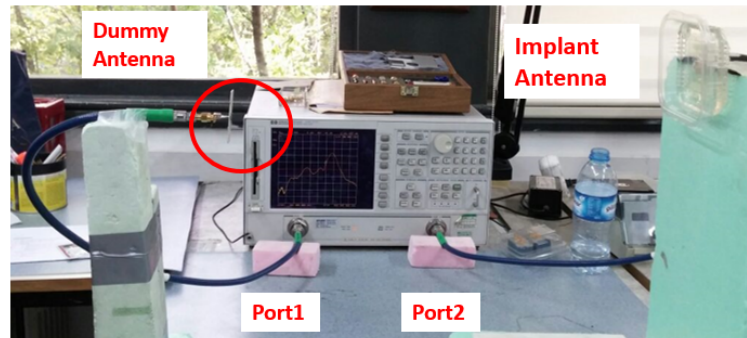
Figure 4.12: Results taken from [21] to show the effect of phantom size on the radiation pattern of the antenna (a) A phantom model with the dimensions of length (l) x width (w) and height (h) (b) Simulated radiation pattern when lateral dimensions of the phantom is modified

for the gain measurement of the proposed antenna at the MICS band. For this aim, a monopole antenna operating at 403.5 MHz is fabricated as the reference antenna. The length of the monopole tip is designed as quarter wavelength (17 cm) and the ground plane size is chosen as 60 cm x 60 cm. The gain of the monopole antenna is taken as 2 dBi according to simulation results. Gain measurement is done using 3 antennas: monopole antenna, proposed implantable antenna and a dummy antenna which operates in the MICS band. The measurement is conducted via network analyzer (Agilent 8720D) and S_{21} values are measured. Dummy antenna is connected to the first port of the network analyzer. Then, the proposed antenna and the monopole antenna are connected to second port of the network analyzer, in sequence. The measurement setup is shown in Figure 4.13. The S_{21} value of the proposed antenna is compared with the monopole antenna and the gain is found as -4.5 dBi at 403.5 MHz. Since the maximum gain values are not consistent with the simulation results, it is decided to conduct a literature survey to find out the gain measurement techniques for ESAs. The method proposed by Zürcher in [22] is found and presented in here.

According to [22], due to the limited size ground plane and difficulty in properly realizing baluns (balanced to unbalanced) in a small volume, electrically small



(a)



(b)

Figure 4.13: Photographs of gain measurement setup for the MICS band (a) First measurement: S_{21} measurement of dummy antenna and monopole antenna (b) Second measurement: S_{21} measurement of dummy antenna and proposed implantable antenna

antennas cannot be considered as purely symmetrical or purely anti-symmetrical. Therefore, when considering the gain measurement of electrically small antennas, traditional gain measurement techniques becomes inadequate because of the spurious radiation from the cable connecting the antenna to the measuring equipment [72]. A solution to this problem was proposed and listed as below [22]:

- Mounting the electrically small antenna under test in its definitive environment in the shielded case which will later contain the electronic equipment used for the particular application.
- Feeding the antenna with a stable voltage controlled oscillator (VCO) of known measured output power, enclosed together with batteries, in the shielded case. This forms the device under test (DUT).
- Rotating in an anechoic chamber the DUT in all possible orientations and polarizations using a specially designed "random" positioner, and capturing the maximum received level using the "peak hold" function of a spectrum analyzer
- Replacing the DUT by a reference antenna having an accurately known gain and fed by a calibrated synthesizer at the same frequency as the DUT. The synthesizer power level is adjusted to obtain the same received level as the maximum produced by the DUT.
- The exact maximum gain of the small antenna under test can then be determined immediately by a simple calculation

The schematic of the proposed measurement system and realized measurement system in the anechoic chamber are shown in Figure 4.14 and Figure 4.15, respectively. Since the EEE Antenna Measurement Laboratory of METU does not have the mentioned setup, the gain measurement of the implantable antenna is not performed. Instead, link measurement is done using ZLE70102 transceiver module, since it comes with its own VCO and receiver unit.

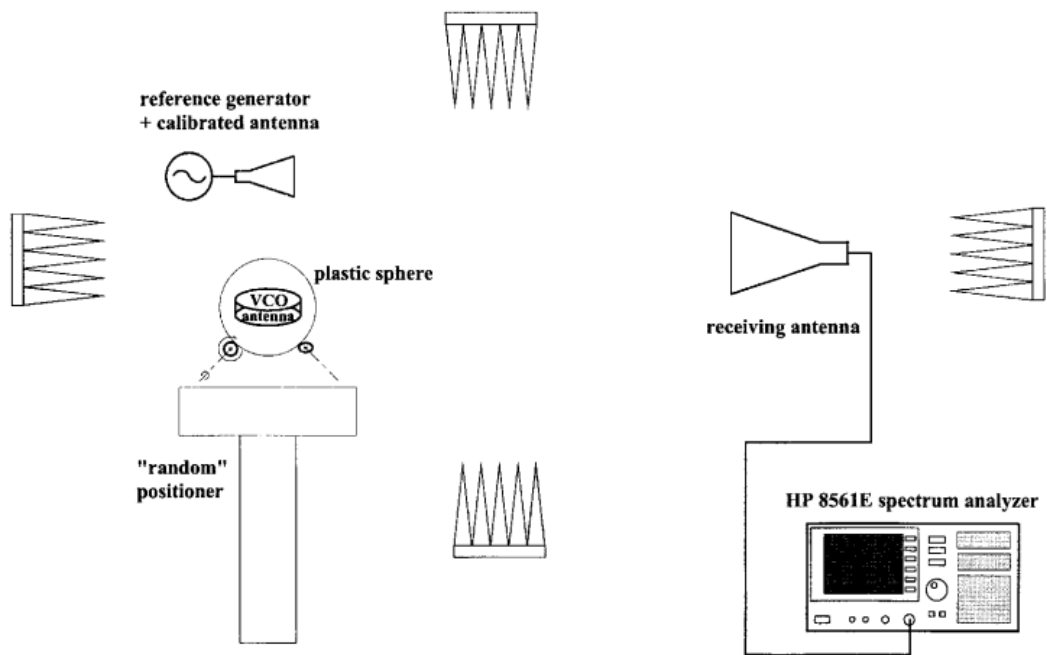
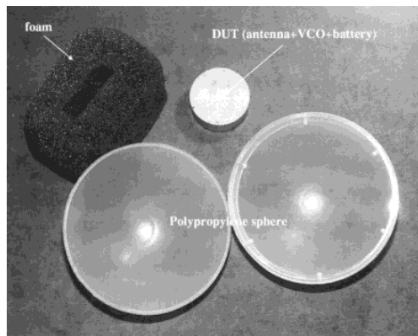
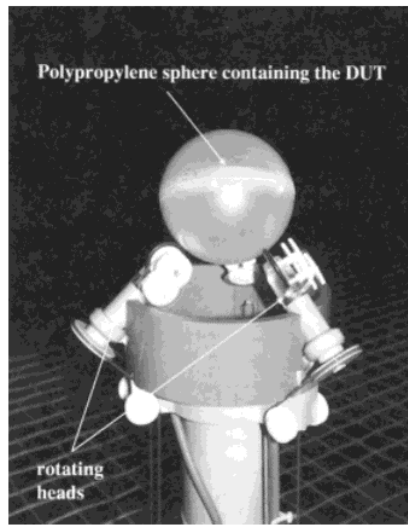


Figure 1 Gain measurement technique for electrically small antennas

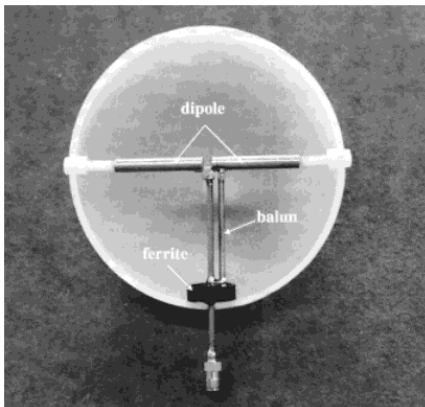
Figure 4.14: Schematic of the gain measurement technique for electrically small antennas proposed in [22]



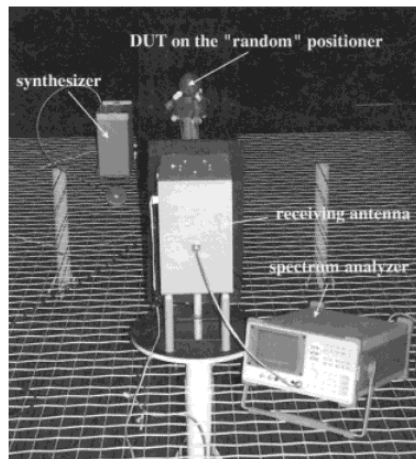
(a)



(b)



(c)



(d)

Figure 4.15: Photographs of electrically small antenna gain measurement setup taken from [22] (a) Dielectric (Polypropylene) sphere that encloses the antenna is used to position the DUT in every possible position and polarization. Device under test is defined as combination of antenna, VCO and battery. DUT is centered within the sphere using the low-density foam (b) Details of the implemented random positioner (c) Reference gain antenna: Dipole mounted within dielectric sphere (d) Complete measurement setup in the anechoic chamber

CHAPTER 5

CONCLUSION

In this thesis study, numerical and experimental analysis of two electrically small implantable antenna designs for biomedical applications were presented. For the first design, antenna was tuned to operate in the Medical Implant Communications Service (MICS, 402 – 405 MHz) band. Then, a miniaturized, compact size, dual band (MICS and ISM) implantable antenna design was proposed. The feasibility and limitations of the proposed antenna were investigated and it was shown that designed antenna can be used in wireless communication link for biomedical implantable systems.

In the first design, it was aimed to study a patch based implantable antenna operating in the MICS band. Therefore, characteristics of the patch antennas were investigated at this band. Numerical studies were conducted via HFSS when the antenna is in the air and inserted into skin tissue. Implantable antenna was explored as an electrically small antenna and miniaturization techniques, namely, loading the substrate, introducing shorting pin and patch meandering were utilized to achieve a compact size. The maximum simulated gain of the antenna was found as -36 dBi. To confirm the validity of the numerical simulations, return loss measurements were carried out. Antenna with a size of $3.1\text{ cm} \times 1.1\text{ cm} \times 1.27\text{ mm}$ was fabricated on a RO3210 substrate. To test the antenna *in vitro*, a skin mimicking gel was prepared and the electrical properties of skin at the MICS band was measured using virtual line method. Antenna was inserted into skin phantom and measurements were done via a network analyser (N9915A FieldFox Analyser). Measurement results showed that the antenna

resonates from 335 MHz to 474 MHz ($BW : 34\%$) at the MICS band for S_{11} less than -10 dB.

In the second design, antenna size was reduced up to $2\text{ cm} \times 1\text{ cm} \times 3.81\text{ mm}$. Stacked type antenna was used to enhance the bandwidth and increase the gain of the antenna. The maximum simulated gain was found as -32.9 dBi and -12.7 dBi for the MICS and ISM bands, respectively. Antenna is tuned to resonate at both the MICS and ISM bands. Parametric simulation studies were conducted for the initial design and then Quasi-Newton optimization tool of the HFSS was utilized to achieve better matching. To confirm the validity of the numerical simulations, experiments were carried out. For return loss measurement of the antenna, skin mimicking gel was prepared in the MICS and ISM bands. Measurement results showed that the antenna resonates at 403.5 MHz with a reflection coefficient of -23 dB , and a wide 10-dB bandwidth of 56 MHz, which covers the MICS band, moreover, it resonates at 2.45 GHz with a reflection coefficient of -22 dB , and a wide 10-dB bandwidth of 200 MHz, which covers the ISM band. For communication link measurement, commercially available Microsemi-Zarlink Application Development Kit for Medical Telemetry (ZLE70102) was used in the anechoic chamber. Designed antenna was inserted into MICS band phantom and antenna that comes with ZLE70102 implant module was replaced with the designed one. It is achieved to wake-up base station module at the ISM band and send data at the MICS band in 4 meter range.

In addition, the feasibility and limitations of the proposed antenna were explored. For patient safety considerations, biocompatibility issues were investigated and SAR was analyzed with respect to IEEE limitations. The change in the resonant frequency with respect to different antenna positions in three layered phantom (skin, fat, muscle) was discussed. It was observed that, when antenna is implanted in the fat layer, the resonant frequency of the antenna shifts significantly. In addition, far field properties of the implanted antennas were discussed. Effects of conducting medium on antenna radiation pattern were analysed and it was concluded that radiation pattern is affected mainly from the finite size human geometry. The gain measurement of the electrically small antennas were studied and a measurement setup was proposed.

In this thesis, compact, small size, dual band operated (MICS and ISM) implantable antenna which can be used in wireless data communication link for biomedical implantable systems are presented. To improve the antenna design for realistic applications, some points should be analysed further in the future. They are as follows:

1. Developing an optimization tool in order to fasten the antenna design for the electromagnetic simulations
2. Conducting numerical simulations on realistic human body models
3. Development of three-layered (skin, fat, and muscle) phantoms and conducting experiments on them
4. Developing gain measurement set-up for electrically small antennas
5. Testing the far field performance of the antenna with a realistic medical device including electronic components

APPENDIX A

MEASUREMENT OF ELECTRICAL PROPERTIES

A.1 Theory

The permittivity ϵ of a linear, homogeneous and isotropic medium is in general a complex quantity and expressed as:

$$\epsilon = \epsilon_0(\epsilon'_r - j\epsilon''_r) \quad (\text{A.1})$$

where ϵ_0 is the permittivity of vacuum. The imaginary term ϵ''_r is related with the conductivity as follows:

$$\sigma = w\epsilon_0\epsilon''_r \quad (\text{A.2})$$

where w is the angular frequency ($w = 2\pi f$)

To validate the electrical properties (permittivity ϵ and conductivity σ) of the prepared phantoms, virtual line method is used [69]. In this method, the coaxial line is placed on the material and it is assumed that the coaxial line extends inside the material (See Figure A.1). Note that the dielectric constant of the material is taken as the dielectric constant of the virtual coaxial line.

The related variables are listed below:

Y_d : Characteristic admittance of the virtual line

ϵ_d : Complex dielectric constant of the material under test

β_d : Propagation constant of the virtual line

Y_t : Characteristic admittance of the coaxial probe

ϵ_t : Complex dielectric constant of the dielectric material used in the probe

β_t : Propagation constant of the probe

Y_L : The admittance at the probe's open end

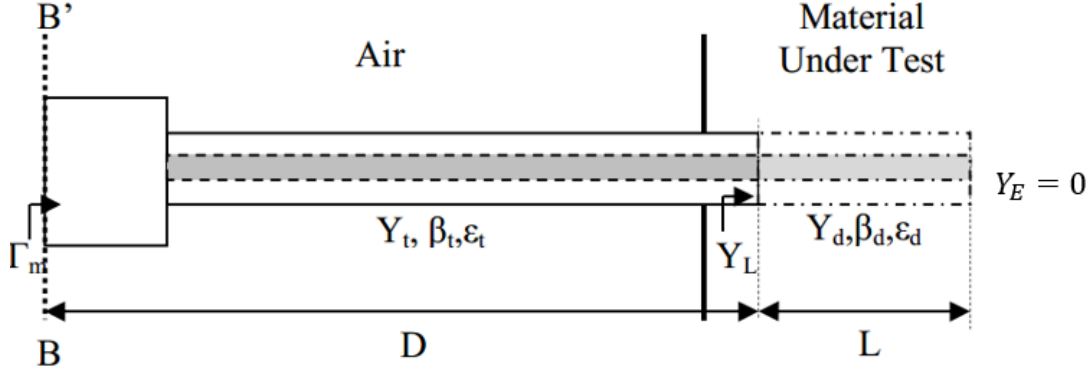


Figure A.1: Open-ended probe model for virtual line method [23]

Γ_m : Measured reflection coefficient at B-B' section

D : Physical length of the probe

L : Length of the virtual line

Assuming a quasi-TEM propagating mode, the complex admittance at plane BB' can be expressed as:

$$Y_L = Y_d \frac{Y_E + jY_d \tan(\beta_d L)}{Y_d + jY_E \tan(\beta_d L)} \quad (\text{A.3})$$

By neglecting the radiation losses, terminating impedance is taken as open circuit and equation in A.3 becomes:

$$Y_L = jY_d \tan(\beta_d L) \quad (\text{A.4})$$

Y_d and Y_t can be written as a function of physical parameters of the virtual line as follows:

$$Y_d = \frac{\sqrt{\epsilon_d}}{60 \ln(b/a)} Y_t = \frac{\sqrt{\epsilon_t}}{60 \ln(b/a)} \quad (\text{A.5})$$

where a and b are the inner and outer diameters of the coaxial probe, respectively.

The admittance of Y_L can be written in terms of characteristic admittance of probe (Y_t) and measured reflection coefficient at plane BB' (Γ_m) as follows:

$$Y_L = \left[\frac{1 - \Gamma_m e^{2j\beta_t D}}{1 + \Gamma_m e^{2j\beta_t D}} \right] Y_t \quad (\text{A.6})$$

Using equations given in A.4, A.5 and A.6, the complex permittivity of the tested material can expressed by:

$$\epsilon_d = \frac{-jc\sqrt{\epsilon_t} \frac{1 - \Gamma_m e^{2j\beta_t D}}{1 + \Gamma_m e^{2j\beta_t D}} \coth\left(\frac{2\pi f L \sqrt{\epsilon_d}}{c}\right)}{2\pi f L} \quad (\text{A.7})$$

where c is the speed of light and f is the frequency.

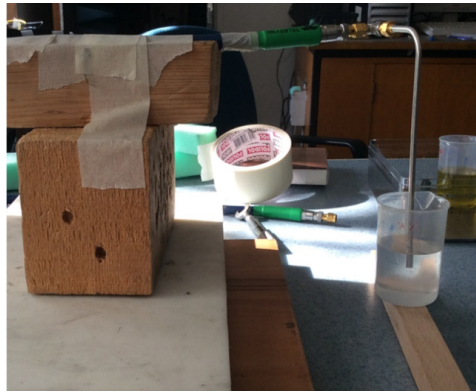
In order to determine the relative dielectric constant and the loss factor of the test medium, probe parameters D and L required to be determined at each measuring frequency. They can be found by calibration with the use of two standard mediums. As calibration materials, air and deionized water is preferred for simplicity. A MATLAB tool developed by Top in [23] is improved for the calculation of the dielectric constant of the materials.

A.2 Experimental Studies and Results

In experimental studies, it is aimed to measure materials for which the dielectric constant is known to validate the proposed method. Sample material is chosen as olive oil. To determine the reflection coefficient (Γ_m), HP8720D Network Analyzer is used. Network analyzer is calibrated using 85052D calibration kit in 50 MHz-6 GHz frequency band. An L-shaped semi-rigid cable having 130 mm length is used as the probe. The measurement of the calibration references is presented in Figure A.2. Note that to remove the reflections caused by the intersection between the cable, *gating* option of the network analyzer is utilized (See Figure A.3). The measured dielectric constant of the olive oil is shown in Figure A.4. Both the real (ϵ'_r) and imaginary parts (ϵ''_r) of the permittivity are presented. The real part of the olive oil's permittivity (ϵ'_r) is found as 3 which is consistent with the reference values given in [73].



(a)



(b)

Figure A.2: Measurement setup of the calibration references (a) Air (b) De-ionized Water

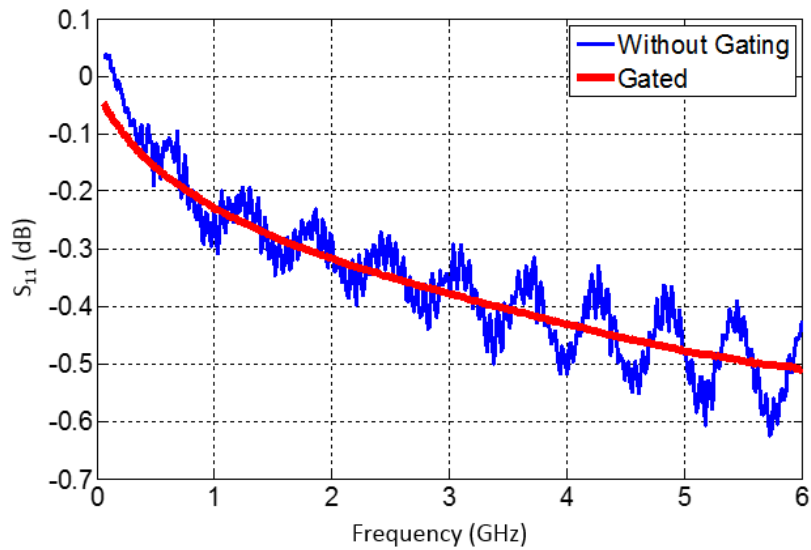


Figure A.3: Comparison of measured S_{11} of the air when *gating* option is on and off

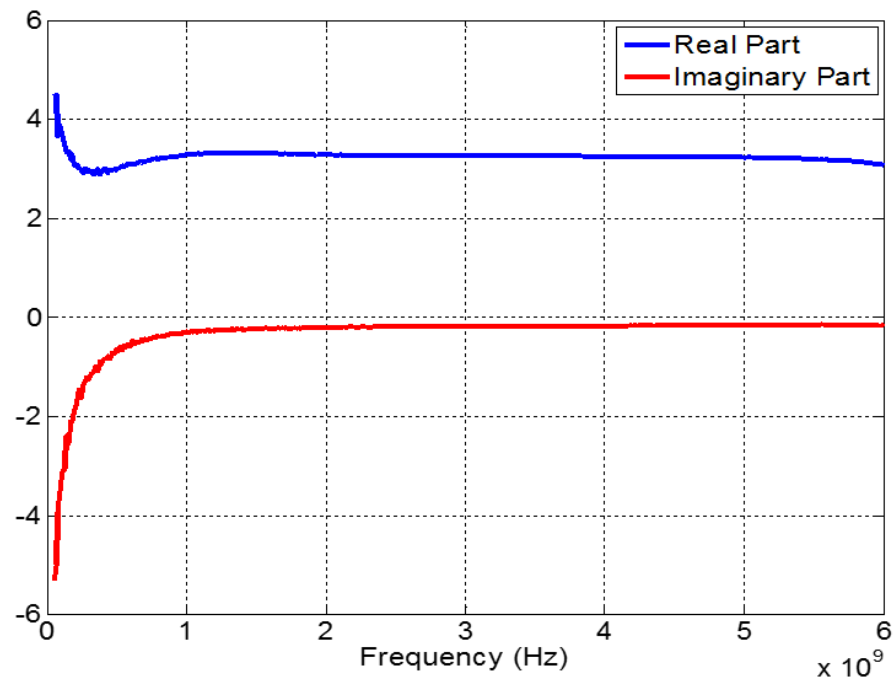


Figure A.4: Measured dielectric constant of olive oil: Real part (ϵ'_r) and the imaginary (ϵ''_r) of the permittivity are presented.

REFERENCES

- [1] T. Karacolak, A. Hood, and E. Topsakal, "Design of a dual-band implantable antenna and development of skin mimicking gels for continuous glucose monitoring," *IEEE Transactions on Microwave Theory and Techniques*, vol. 56, pp. 1001–1008, April 2008.
- [2] T. Karacolak, *Implantable Antennas for Wireless Data Telemetry: Design, Simulation, And Measurement Techniques*. PhD thesis, Mississippi State University.
- [3] T. Karacolak, R. Cooper, J. Butler, S. Fisher, and E. Topsakal, "In vivo verification of implantable antennas using rats as model animals," *Antennas and Wireless Propagation Letters, IEEE*, vol. 9, pp. 334–337, 2010.
- [4] J. Kim and Y. Rahmat-Samii, "Implanted antennas inside a human body: simulations, designs, and characterizations," *IEEE Transactions on Microwave Theory and Techniques*, vol. 52, pp. 1934–1943, Aug 2004.
- [5] W. Xia, K. Saito, M. Takahashi, and K. Ito, "Performances of an implanted cavity slot antenna embedded in the human arm," *IEEE Transactions on Antennas and Propagation*, vol. 57, no. 4, pp. 894–899, 2009.
- [6] A. Kiourti and K. Nikita, "Miniature scalp-implantable antennas for telemetry in the mics and ism bands: Design, safety considerations and link budget analysis," *IEEE Transactions on Antennas and Propagation*, vol. 60, pp. 3568–3575, Aug 2012.
- [7] C. Liu, Y.-X. Guo, and S. Xiao, "Capacitively loaded circularly polarized implantable patch antenna for ism band biomedical applications," *IEEE Transactions on Antennas and Propagation*, vol. 62, no. 5, pp. 2407–2417, 2014.
- [8] T.-F. Chien, C.-M. Cheng, H.-C. Yang, J.-W. Jiang, and C.-H. Luo, "Development of nonsuperstrate implantable low-profile cpw-fed ceramic antennas," *Antennas and Wireless Propagation Letters, IEEE*, vol. 9, pp. 599–602, 2010.
- [9] F. Merli, L. Bolomey, J. Zurcher, G. Corradini, E. Meurville, and A. Skrivervik, "Design, realization and measurements of a miniature antenna for implantable wireless communication systems," *IEEE Transactions on Antennas and Propagation*, vol. 59, pp. 3544–3555, Oct 2011.
- [10] J. R. James and P. S. Hall, *Handbook of Microstrip Antennas, Vols. 1 and 2*. 1989.
- [11] J. Volakis, C.-C. Chen, and K. Fujimoto, *Small antennas: miniaturization techniques & applications*. McGraw Hill Professional, 2010.

- [12] Z. Chen and M. Chia, *Broadband Planar Antennas: Design and Applications*. Wiley, 2006.
- [13] R. B. Waterhouse, *Printed antennas for wireless communications*. Wiley Online Library, 2007.
- [14] S. R. Best and J. D. Morrow, “The effectiveness of space-filling fractal geometry in lowering resonant frequency,” *Antennas and Wireless Propagation Letters, IEEE*, vol. 1, no. 1, pp. 112–115, 2002.
- [15] C. A. Balanis, *Modern Antenna Handbook*. New York, NY, USA: Wiley-Interscience, 2008.
- [16] K.-L. Wong, *Compact and Broadband Microstrip Antennas*. New York, NY, USA: Wiley-Interscience, 2002.
- [17] S. Dey and R. Mittra, “Compact microstrip patch antenna,” *Microwave and Optical Technology Letters*, vol. 13, no. 1, pp. 12–14, 1996.
- [18] F.-J. Huang, C.-M. Lee, C.-L. Chang, L.-K. Chen, T.-C. Yo, and C.-H. Luo, “Rectenna application of miniaturized implantable antenna design for triple-band biotelemetry communication,” *IEEE Transactions on Antennas and Propagation*, vol. 59, pp. 2646–2653, July 2011.
- [19] C. Gabriel, S. Gabriel, and E. Corthout, “The dielectric properties of biological tissues: I. literature survey,” *Physics in medicine and biology*, vol. 41, no. 11, p. 2231, 1996.
- [20] R. Moore, “Effects of a surrounding conducting medium on antenna analysis,” *IEEE Transactions on Antennas and Propagation*, vol. 11, pp. 216–225, May 1963.
- [21] F. Merli, “Implantable antennas for biomedical applications,” Ph.D. thesis, EPFL, 2011.
- [22] J.-F. Zürcher, O. Staub, A. Skrivervik, and M. Hermanjat, “Accurate measurement of the maximum gain of electrically small antennas,” *Microwave and Optical Technology Letters*, vol. 23, no. 6, pp. 328–331, 1999.
- [23] C. B. Top, “Harmonic motion microwave doppler imaging,” Ph.D. thesis, Middle East Technical Univ., 2013.
- [24] A. Kiourti and K. Nikita, “Implantable antennas: A tutorial on design, fabrication, and in vitro/in vivo testing,” *Microwave Magazine, IEEE*, vol. 15, pp. 77–91, June 2014.
- [25] R. Kasevish, “Electromagnetic scale modeling of implantable microwave antennas for cancer hyperthermia,” in *Bioengineering Conference, 1988., Proceedings of the 1988 Fourteenth Annual Northeast*, pp. 261–265, Mar 1988.
- [26] R. D. Beach, F. v. Küster, and F. Moussy, “Subminiature implantable potentiostat and modified commercial telemetry device for remote glucose monitoring,” *IEEE Transactions on Instrumentation and Measurement*, vol. 48, no. 6, pp. 1239–1245, 1999.

- [27] W. G. Scanlon, N. E. Evans, and Z. M. McCreesh, "Rf performance of a 418-mhz radio telemeter packaged for human vaginal placement," *IEEE Transactions on Biomedical Engineering*, vol. 44, no. 5, pp. 427–430, 1997.
- [28] P. Valdastri, A. Menciacchi, A. Arena, C. Caccamo, and P. Dario, "An implantable telemetry platform system for in vivo monitoring of physiological parameters," *IEEE Transactions on Information Technology in Biomedicine*, vol. 8, no. 3, pp. 271–278, 2004.
- [29] "Medical implant communications service (MICS) federal register," *Rules Reg.*, vol. 64, pp. 69926–69934, Dec. 1999.
- [30] *Radio Regulations*, International Telecommunications Union Recommendation (ITU-R), Section 5.138 and 5.150.
- [31] P. Soontornpipit, C. M. Furse, and Y. C. Chung, "Design of implantable microstrip antenna for communication with medical implants," *IEEE Transactions on Microwave Theory and Techniques*, vol. 52, no. 8, pp. 1944–1951, 2004.
- [32] T. Houzen, M. Takahashi, K. Saito, and K. Ito, "Implanted planar inverted f-antenna for cardiac pacemaker system," in *Antenna Technology: Small Antennas and Novel Metamaterials, 2008. iWAT 2008. International Workshop on*, pp. 346–349, IEEE, 2008.
- [33] Microsemi, Medical Implant RF transceiver ZL70102.
- [34] A. K. Skrivervik, "Implantable antennas: The challenge of efficiency," in *Antennas and Propagation (EuCAP), 2013 7th European Conference on*, pp. 3627–3631, Ieee, 2013.
- [35] *Sharing between the Meteorological Aids Service and Medical Implant Communications Systems (MICS) operating in the Mobile Service in the Frequency Band 401-406 MHz.*, International Telecommunications Union Recommendation (ITU-R) Std. ITU-R Recommendation SA 1346, 2001.
- [36] *IEEE Standard for Safety Levels with Respect to Human Exposure to Radio Frequency Electromagnetic Fields, 3 kHz to 300 GHz*, IEEE Standard C95.1-1999, 1999.
- [37] H. Mizuno, M. Takahashi, K. Saito, N. Haga, and K. Ito, "Design of a helical folded dipole antenna for biomedical implants," in *Antennas and Propagation (EUCAP), Proceedings of the 5th European Conference on*, pp. 3484–3487, April 2011.
- [38] P. Izdebski, H. Rajagopalan, and Y. Rahmat-Samii, "Conformal ingestible capsule antenna: A novel chandelier meandered design," *IEEE Transactions on Antennas and Propagation*, vol. 57, pp. 900–909, April 2009.
- [39] K. Gosalia, M. Humayun, and G. Lazzi, "Impedance matching and implementation of planar space-filling dipoles as intraocular implanted antennas in a retinal prosthesis," *IEEE Transactions on Antennas and Propagation*, vol. 53, pp. 2365–2373, Aug 2005.

- [40] H. Usui, M. Takahashi, and K. Ito, "Radiation characteristics of an implanted cavity slot antenna into the human body," in *Antennas and Propagation Society International Symposium 2006, IEEE*, pp. 1095–1098, July 2006.
- [41] C.-M. Lee, T.-C. Yo, F.-J. Huang, and C.-H. Luo, "Dual-resonant π -shape with double l-strips pifa for implantable biotelemetry," *Electronics Letters*, vol. 44, no. 14, pp. 837–839, 2008.
- [42] C. Liu, Y.-X. Guo, and S. Xiao, "Compact dual-band antenna for implantable devices," *Antennas and Wireless Propagation Letters, IEEE*, vol. 11, pp. 1508–1511, 2012.
- [43] L.-J. Xu, Y.-X. Guo, and W. Wu, "Dual-band implantable antenna with open-end slots on ground," *Antennas and Wireless Propagation Letters, IEEE*, vol. 11, pp. 1564–1567, 2012.
- [44] C.-M. Lee, T.-C. Yo, and C.-H. Luo, "Compact broadband stacked implantable antenna for biotelemetry with medical devices," in *Wireless and Microwave Technology Conference, 2006. WAMICON'06. IEEE Annual*, pp. 1–4, IEEE, 2006.
- [45] W.-C. Liu, F.-M. Yeh, and M. Ghavami, "Miniaturized implantable broadband antenna for biotelemetry communication," *Microwave and Optical Technology Letters*, vol. 50, no. 9, pp. 2407–2409, 2008.
- [46] W.-C. Liu, S.-H. Chen, and C.-M. Wu, "Bandwidth enhancement and size reduction of an implantable pifa antenna for biotelemetry devices," *Microwave and Optical Technology Letters*, vol. 51, no. 3, pp. 755–757, 2009.
- [47] A. Kiourti and K. Nikita, "A review of implantable patch antennas for biomedical telemetry: Challenges and solutions [wireless corner]," *Antennas and Propagation Magazine, IEEE*, vol. 54, pp. 210–228, June 2012.
- [48] J. Ung and T. Karacolak, "A wideband implantable antenna for continuous health monitoring in the medradio and ism bands," *Antennas and Wireless Propagation Letters, IEEE*, vol. 11, pp. 1642–1645, 2012.
- [49] Z. Duan, Y.-X. Guo, R.-F. Xue, M. Je, and D.-L. Kwong, "Differentially fed dual-band implantable antenna for biomedical applications," *IEEE Transactions on Antennas and Propagation*, vol. 60, pp. 5587–5595, Dec 2012.
- [50] D. Pozar and B. Kaufman, "Increasing the bandwidth of a microstrip antenna by proximity coupling," *Electronics Letters*, vol. 23, pp. 368–369, April 1987.
- [51] C. A. Balanis, *Antenna Theory: Analysis and Design*. Wiley-Interscience, 2005.
- [52] K. R. Carver and J. Mink, "Microstrip antenna technology," *IEEE Transactions on Antennas and Propagation*, vol. 29, pp. 2–24, Jan 1981.
- [53] Y. Lo, D. Solomon, and W. Richards, "Theory and experiment on microstrip antennas," *IEEE Transactions on Antennas and Propagation*, vol. 27, pp. 137–145, Mar 1979.

- [54] W. Richards, Y. Lo, and D. Harrison, "An improved theory for microstrip antennas and applications," *IEEE Transactions on Antennas and Propagation*, vol. 29, pp. 38–46, Jan 1981.
- [55] M. Bailey and M. Deshpande, "Integral equation formulation of microstrip antennas," *IEEE Transactions on Antennas and Propagation*, vol. 30, pp. 651–656, Jul 1982.
- [56] E. Van Lil and A. Van de Capelle, "Transmission line model for mutual coupling between microstrip antennas," *IEEE Transactions on Antennas and Propagation*, vol. 32, pp. 816–821, Aug 1984.
- [57] C. A. Balanis, *Advanced Engineering Electromagnetics*. Wiley-Interscience, 2012.
- [58] E. Hammerstad, "Equations for microstrip circuit design," in *Microwave Conference, 1975. 5th European*, pp. 268–272, Sept 1975.
- [59] F. Gustrau, *RF and Microwave Engineering: Fundamentals of Wireless Communications*. John Wiley & Sons, 2012.
- [60] D. Pozar, "Rigorous closed-form expressions for the surface wave loss of printed antennas," *Electronics Letters*, vol. 26, pp. 954–956, June 1990.
- [61] I. Bahl, P. Bhartia, and S. Stuchly, "Design of microstrip antennas covered with a dielectric layer," *IEEE Transactions on Antennas and Propagation*, vol. 30, pp. 314–318, Mar 1982.
- [62] H. Wheeler *et al.*, "Fundamental limitations of small antennas," *Proceedings of the IRE*, vol. 35, no. 12, pp. 1479–1484, 1947.
- [63] Z. Qi, F. Kan, and L. Tie-zhu, "Analysis of planar inverted-f antenna using equivalent models," in *Antennas and Propagation Society International Symposium, 2005 IEEE*, vol. 3A, pp. 142–145 vol. 3A, July 2005.
- [64] M.-C. Huynh and W. Stutzman, "Ground plane effects on planar inverted-f antenna (pifa) performance," *Microwaves, Antennas and Propagation, IEE Proceedings*, vol. 150, pp. 209–213, Aug 2003.
- [65] P. Bhartia, I. Bahl, R. Garg, and A. Ittipiboon, "Microstrip antenna design handbook," *Norwood, MA, Artech House*, 2000.
- [66] "Antenna modeling software, in www.eznec.com."
- [67] T. Endo, Y. Sunahara, S. Satoh, and T. Katagi, "Resonant frequency and radiation efficiency of meander line antennas," *Electronics and Communications in Japan (Part II: Electronics)*, vol. 83, no. 1, pp. 52–58, 2000.
- [68] T. Yilmaz, *Characterization of tissue mimicking materials for testing of implantable and on body antennas*. Mississippi State University, 2009.
- [69] F. Ghannouchi and R. Bosisio, "Measurement of microwave permittivity using a six-port reflectometer with an open-ended coaxial line," *IEEE Transactions on Instrumentation and Measurement*, vol. 38, pp. 505–508, Apr 1989.

- [70] Microsemi, Medical Implant RF transceiver ZLE70102, 2010.
- [71] O. Gandhi, G. Lazzi, and C. Furse, “Electromagnetic absorption in the human head and neck for mobile telephones at 835 and 1900 mhz,” *IEEE Transactions on Microwave Theory and Techniques*, vol. 44, pp. 1884–1897, Oct 1996.
- [72] O. Staub, J.-F. Zürcher, and A. Skrivervik, “Some considerations on the correct measurement of the gain and bandwidth of electrically small antennas,” *Microwave and Optical Technology Letters*, vol. 17, no. 3, pp. 156–160, 1998.
- [73] T. Chen, “Capacitive sensors for measuring complex permittivity of planar and cylindrical structures,” Ph.D. thesis, Iowa State Univ., 2012.